JUSTUS-LIEBIG-
UNIVERSITÄT
GIESSEN

Faculty 07 - Mathematics and Computer Science, Physics, Geography
II. Physics Institute - Hadronphysics

Revision of the $\overline{\text{P}}$ANDA Calorimeter Front-End operating parameters by means of high energetic photons

Verbesserung der PANDA-Kalorimeter Front-End-Betriebsparameter mittels hochenergetischer Photonen

MASTER THESIS

for obtaining the academic degree

Master of Science

submitted by

Aniko Tim Falk

Matriculation number: 1004383

Gießen 2020

Initial corrector:	Prof. Dr. Brinkmann
Secondary corrector / supervisor:	Dr. Markus Moritz
technical supervisors:	Dr. Hans-Georg Zaunick, René Schubert

Contents

List of abbreviations **VI**

Abstract **1**

1. Introduction & Motivation **3**
1.1. FAIR . . . 3
1.2. $\overline{\text{P}}$ANDA . . . 4
1.3. Motivation . . . 6

2. Theory **7**
2.1. Interaction of radiation with matter . . . 7
2.1.1. Photoelectric effect . . . 7
2.1.2. Compton effect . . . 8
2.1.3. Pair-production . . . 9
2.2. Lead tungstate scintillator . . . 9
2.3. Avalanche photodiodes . . . 9
2.4. APFEL . . . 10
2.5. $\overline{\text{P}}$ANDA SADC . . . 13

3. Experimental Setup **17**
3.1. Detector matrix . . . 17
3.2. Readout electronics . . . 21
3.3. Cooling and Temperature Control . . . 22
3.4. Light pulser . . . 25
3.5. MAMI . . . 26
3.6. APD-gain setups . . . 29

4. Procedure **31**
4.1. Accelerator runs . . . 31
4.2. Lightpulser runs . . . 33
4.3. Cosmic Radiation run . . . 34

5. Analysis **35**
5.1. Raw beam and cosmics data . . . 35

5.2. Calibration 40
5.3. Calibration with light pulser 49
5.4. Timecuts 52
5.5. Beam position 58
5.6. Lineshapes 59
5.7. Energy resolution 63

6. Discussion **67**

7. Outlook **78**

References **80**

A. Appendix **81**

List of figures **86**

List of tables **87**

Acknowledgements **88**

Eidesstattliche Erklärung

Hiermit versichere ich, die vorgelegte Thesis selbstständig und ohne unerlaubte fremde Hilfe und nur mit den Hilfen angefertigt zu haben, die ich in der Thesis angegeben habe.
Alle Textstellen, die wörtlich oder sinngemäß aus veröffentlichten Schriften entnommen sind und alle Angaben die auf mündlichen Auskünften beruhen, sind als solche kenntlich gemacht.
Bei den von mir durchgeführten und in der Thesis erwähnten Untersuchungen habe ich die Grundsätze guter, wissenschaftlicher Praxis, wie sie in der "Satzung der Justus-Liebig-Universität zur Sicherung guter wissenschaftlicher Praxis" niedergelegt sind, eingehalten. Gemäß §25 Abs. 6 der Allgemeinen Bestimmungen für modularisierte Studiengänge dulde ich eine Überprüfung der Thesis mittels Anti-Plagiatssoftware.

Gießen, den 22.10.2020

.....
Aniko Tim Falk

List of abbreviations

APD	Avalanche photodiode
APFEL	ASIC for $\overline{\mathrm{P}}$ANDA front-end electronic
ASIC	Application specific integrated circuit
EMC	Electromagnetic Calorimeter
FAIR	Facility for Antiproton and Ion Research
FPGA	Field programmable gate array
GSI	Helmholtz Centre for Heavy Ion Research
HESR	High Energy Storage Ring
LAAPD	Large area avalanche photodiode
MAMI	Mainzer Mikrotron
OpAmp	Operational Amplifier
$\overline{\mathrm{P}}$ANDA	Anti-Proton annihilation at Darmstadt
PCB	Printed circuit-board
SADC	Sampling analog-to-digital converter

Abstract

The barrel part of the electromagnetic calorimeter (EMC) in the future $\overline{\text{P}}$ANDA-experiment provides the possibility to identify and measure photons with high resolution produced during the annihilation of antiprotons and protons. To characterise these with the required efficiency and precision, the barrel and especially the read-out electronics have to be operated at a peak performance. Therefore, the use of optimal gains, thresholds and filters are key elements to achieve the set goals.

Kim Giebenhain proposed the use of a higher gain for the Large-area avalanche photodiodes to be used in $\overline{\text{P}}$ANDA, based on the results of her thesis [3]. She showed, that a significant improvement from 43 % down to 12 % in the energy resolution could be achieved with a higher gain. As these results were produced with a light pulser in the laboratory, the aim of this thesis is the proof of these assumptions in an accelerator experiment at MAMI in Mainz with a detector matrix and close-to-final $\overline{\text{P}}$ANDA front-end electronics.

In the subsequent analysis, several filters and event selections were used and their effect on the data was investigated. The deposited energy per detector was determined by adding up the energies of the two corresponding APDs and the total deposited energy of the matrix was calculated to obtain the lineshapes of various photon energies. Eventually, the energy resolution of the lineshapes was listed in the response function and this in turn was compared for a photodiode gain of 150 and 500, the former being the previously foreseen gain and the latter being the proposition of Kim Giebenhain.

The comparison of low and high photodiode gains displays an improvement in energy resolution from 21.5 % down to 12.4 % (9.1 % absolute improvement) for the lowest energies. Compared to previous tests with the PROTO120, an absolute improvement of the energy resolution by 3.2 % was found.

As the highest photon energies will occur near the forward-endcap of the EMC, this higher gain can be used from 40 ° down to the end of the barrel without losing signals, whilst improving the energy resolution significantly.

Further investigations beyond this thesis could unveil even larger improvements concerning the energy resolution and effective ways to cope with upcoming noise could be discovered.

Zusammenfassung

Das Barrel des Electromagnetic Calorimeter (EMC) im zukünftigen $\overline{\text{P}}$ANDA-Experiment bietet eine Möglichkeit, die Photonen, die während der Annihilation von Protonen und Antiprotonen entstehen, mit hoher Präzision zu identifizieren und zu vermessen. Dafür muss das Barrel-EMC und besonders die Auslese-Elektronik auf Höchstleistung ausgerichtet sein. Daher ist die Verwendung optimaler Verstärkungen, Grenzwerte und Filter unabdingbar, um die gesetzten Ziele zu erreichen.
Kim Giebenhain hat, basierend auf den Ergebnissen ihrer Thesis, eine höhere Verstärkung für die im $\overline{\text{P}}$ANDA-Experiment verwendeten Photodioden vorgeschlagen [3]. Sie zeigte, dass die Verwendung einer höheren Verstärkung die Energieauflösung von 43 % auf 12 % absenken konnte. Da diese Ergebnisse mit einem Lichtpulser unter Laborbedingungen erzeugt wurden, war das Ziel dieser Thesis die Verifizierung dieser Annahmen in einem Experiment an der Beschleuniger-Anlage MAMI in Mainz, mit einer Detektor-Matrix und Front-end Elektronik ähnlich zu der, die für das spätere $\overline{\text{P}}$ANDA-Experiment vorgesehen ist.
In der anschließenden Analyse wurden verschiedene Sortier-Algorithmen und Filter, sowie deren Effekt auf die Messdaten untersucht. Die pro Detektor deponierte Energie wurde durch Summation der beiden zugehörigen Photodioden bestimmt und die in der Matrix deponierte Gesamtenergie wurde für die verschiedenen Photonenenergien errechnet. Letztlich, wurden die Energieauflösungen zur Antwortfunktion des Experiments zusammengetragen und für eine Photodioden-Verstärkung von 150 und 500 verglichen. Dabei ist Erstere die geplante Verstärkung im $\overline{\text{P}}$ANDA-Experiment und Letztere die von Kim Giebenhain Vorgeschlagene.
Der Vergleich zwischen hoher und niedriger Verstärkung im Experiment zeigte eine Verbesserung der Energieauflösung von 21.5 % auf 12.4 % (9.1 % absolute Steigerung) für die niedrigsten gemessenen Energien. Verglichen mit dem PROTO120, war eine absolute Steigerung um 3.2 % festzustellen. Da die höchsten Photonenenergien nur nahe der Forward-Endcap des EMC auftauchen, kann die höhere Verstärkung ab einem Winkel von 40 ° im Barrel verwendet werden ohne Informationen zu verlieren, während die Energieauflösung deutlich verbessert wird.
Weitere Untersuchung der Verstärkungsfaktoren außerhalb dieser Thesis könnten weitere Steigerung der Energieauflösung und effektivere Wege zur Bewältigung von auftretendem Rauschen zu Tage fördern.

1. Introduction & Motivation

Using highly efficient readout-systems at their optimal settings is crucial to get the most detailed information out of high-energy physics experiments. Therefore, the working conditions of electronics and detectors for those experiments, must be constantly improved and verified.

1.1. FAIR

The facility for antiproton and ion research (FAIR) is a large accelerator complex currently being constructed at the "Gesellschaft für Schwerionenforschung" (GSI) in Darmstadt, which will be capable of creating diverse particle beams including ions and antiprotons. Several accelerator and storage units will form the 20 hectares large experimental site.

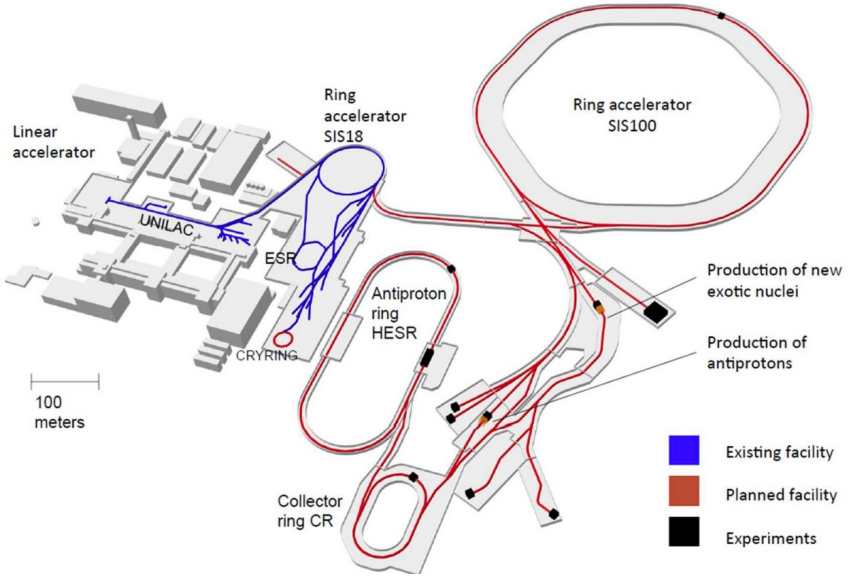

Figure 1: Schematic of FAIR, shown in blue is the existing complex and in red the facilites, that are currently under construction. The $\overline{\text{P}}$ANDA-experiment in the HESR is located on the western side of the new FAIR areal [1].

The facility is constantly extending with new experiments and storage devices like the high-Energy Storage Ring (HESR). FAIR advertises the complex with the highest precision, intensity and diversity of accelerated ions, very high particle

energies of up to the equivalent of 99 % the speed of light and the possibility to operate up to four experiments in parallel at the same time.

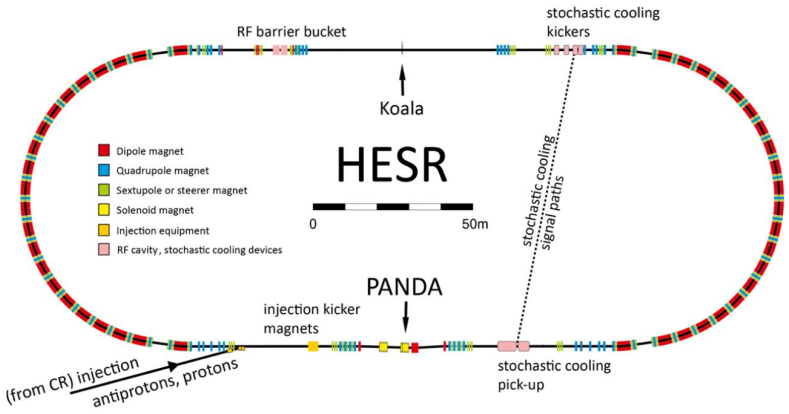

Figure 2: Schematic of the HESR at FAIR. The antiproton beam for the panda experiment is fed in from the lower right, coming from the collector ring (CR). $\overline{\text{P}}$ANDA itself is located at the bottom of the picture [2].

A great variety of experiments are and were built to run on the experimental site of the future FAIR facility, including e.g. HADES (high acceptance di-electron spectrometer), PHELIX (petawatt high-energy laser for ion experiments) and $\overline{\text{P}}$ANDA (anti-proton annihilation at Darmstadt).

1.2. $\overline{\text{P}}$ANDA

The $\overline{\text{P}}$ANDA-Experiment is a high-energy physics experiment, planned to get insight into the still not well understood topic of strong interactions between quarks. The general idea is to let a high-energetic anti-proton beam with a momentum between 1.5 GeV/c and 15 GeV/c collide with hydrogen or nuclear targets. The resulting annihilation produces a multiplicity of different hadrons which can be further analysed and characterised. The HESR, which feeds the antiproton beam into the experiment, features two operational modes: one being a high-resolution mode with intensities up to 10^{10}/s and a high-luminosity mode producing an intensity of up to 10^{11}/s. The experiment is divided into two main parts. One of which is the target spectrometer being built around the interaction point. It consists of the typical setup for high

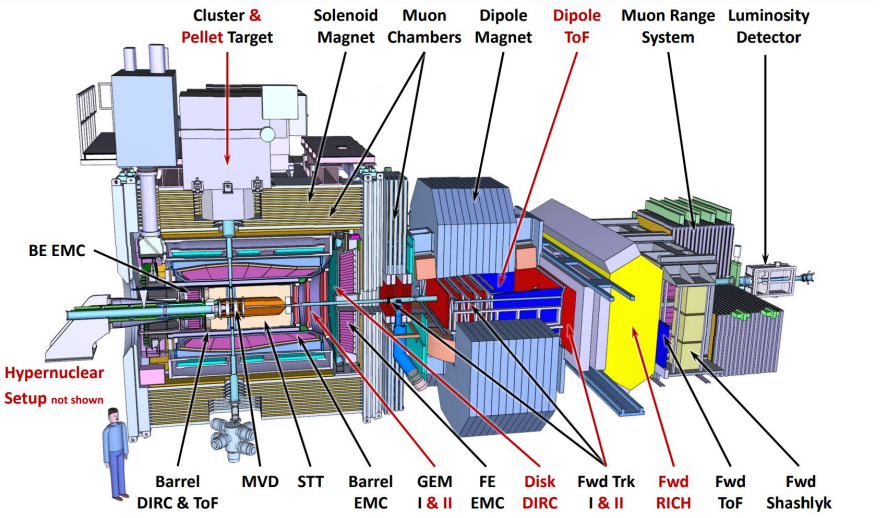

Figure 3: Schematic of the whole $\overline{\text{P}}$ANDA-detector. The purple parts in the vicinity of the interaction point form the electromagnetic spectrometer [10].

energy physics experiments, meaning a micro-vertex detector, a straw-tube tracker, the electromagnetic calorimeter (EMC) formed by the barrel, forward endcap and backward endcap, a solenoid magnet, a detector for internally reflected cherenkov light (DIRC) and time-of-flight-system (ToF) inside the barrel and gas electron multiplier (GEM) detectors. The other being the forward spectrometer consisting of a dipole magnet, Disk DIRC, forward trackers, dipole ToF-detector, a ring imaging cherenkov detector (RICH), forward ToF and Shashlyk calorimeter as well as a luminosity detector.

Especially relevant for this thesis is the EMC. It consists mainly of scintillator 11360 crystals of 11 different geometries in the barrel part and 3856 tapered crystals plus 640 rectangular crystals for the forward and backward endcap, respectively, adding up to 15856 crystals. The scintillator crystals are read-out by avalanche photodiodes, as the strong magnetic field of 2 T makes the usage of photomultiplier tubes (PMTs) impossible.

To generate optimal results, certain requirements for the barrel have to be met. These requirements are hardly met and so it is of high interest to improve these conditions constantly and to build up a performance buffer, in case radiation damage or lacking thermal or magnetic uniformity do inhibit the measurements.

Table 1: Certain requirements for the Barrel-EMC, that should and have been met before operation of the experiment.

Parameter	**Requirement**
Radiation hardness	$> 125\,\mathrm{Gy/a}$
Dynamic range	$10\,\mathrm{MeV}$ to $15\,\mathrm{GeV}$
Temperature	$-25°\mathrm{C}\ \pm 0.1°\mathrm{C}$
Energy resolution	$1\,\% \oplus 2\,\%/\sqrt{E/\mathrm{GeV}}$
Time resolution	$2\,\mathrm{ns}$

Certain goals are set as requirements for the Barrel EMC, ensuring the $\overline{\mathrm{P}}$ANDA-experiment is able to operate with a peak performance if the goals are met. These requirements include e.g. a radiation hardness of over $125\,\mathrm{Gy/a}$, as this is the expected annual dose, or a dynamic range of $10\,\mathrm{MeV}$ up to $15\,\mathrm{GeV}$.
A few more of these requirements are shown in table 1.

1.3. Motivation

The most important specifications of the $\overline{\mathrm{P}}$ANDA calorimeter are energy resolution, time resolution and quantum efficiency. Kim Giebenhain showed in her bachelor's thesis, that a modification of one of the currently planned operational parameters could improve the energy resolution of the measurements drastically, when in low-energy regimes [3]. The parameter tested here was the gain of the photodiode and the results were quite impressive: in lower energy regimes, the energy resolution of the measured signals could be improved from roughly $43\,\%$ to $12\,\%$, compared to the foreseen gain, while the energy resolution in the higher energy regimes remained similar.
Following the results of her thesis, the new optimal gain for the avalanche photodiodes (APD) should be 500 instead of the prior optimal gain of 150, at least for crystals with an angular position of above 40°.
The measurements made by Giebenhain, were made by using a light pulser, which pulses cause signals similar to those from scintillation light. As the light pulses themselves differ from actual scintillation light, these results had to be verified in an actual accelerator experiment an a comparison of different operational parameters had to be carried out for an eventual further improvement.

2. Theory

2.1. Interaction of radiation with matter

The interaction of photons with nuclei and electrons can be assigned to three different processes: photoelectric effect, compton effect and pair-production. They account for a change in energy and direction of the photons or create electrons, respectively, depending on the incident photon. The intensity-mitigation of incoming photon can be described via an exponential function:

$$I(x) = I_0 \cdot \exp^{-\mu x}, \tag{1}$$

with I_0 as incoming intensity, x the effective crossed distance in the material and μ as attenuation coefficient. This in turn can be described through Avogadro's number N_A, the density of the material ρ, the molar mass M and a cross-section coefficient σ, accounting for the three different interaction processes mentioned beforehand:

$$\mu = \frac{N_A \cdot \rho}{M} \cdot \sigma, \tag{2}$$

where σ is defined by:

$$\sigma = \sigma_{\text{Photo}} + Z \cdot \sigma_{\text{Compton}} + \sigma_{\text{Pair}} \tag{3}$$

These three processes will now be discussed briefly.

2.1.1. Photoelectric effect

The photoelectric effect describes an interaction, where the incoming photon is completely absorbed by a bound electron. The electron can be emitted by the atom which it was bound to, if the absorbed energy is greater than its work function. The kinetic energy of an electron emitted in this way can therefore be written as:

$$E_{\text{kin}} = E_\gamma - W \tag{4}$$

with the energy of the incident photon E_γ and the work function of the material W. This dependency allows to derive the energy of incident photons by measuring the kinetic energy of photoelectrons. The cross-section belonging to the photoelectric effect is proportional to:

$$\sigma_{\text{Photo}} \propto \frac{Z^5}{E_\gamma^{7/2}}, \tag{5}$$

with the atomic number Z.

2.1.2. Compton effect

The compton effect characterises inelastic scattering of a photon by a charged particle. The incident photon transfers energy to the electron and the electron is emitted from its atom. This means, that the energy of the incident photon must be large against the work function of the material $E_\gamma \gg W$. The scattered photon changes its direction of flight and travels with reduced energy after the scattering process. The remaining photon energy can be calculated by the following formula:

$$E_{\gamma'} = \frac{E_\gamma}{1 + \frac{E_\gamma}{mc^2} \cos\theta}, \tag{6}$$

where θ is the scattering angle.
The cross-section proportion of the compton scattering in turn can be qualified by:

$$\sigma_{\text{Photo}} \propto \frac{Z}{E_\gamma} \tag{7}$$

2.1.3. Pair-production

If the incident photon has a larger energy than two times the rest mass multiplied by the squared light velocity ($E_\gamma > m_e c^2$), the generation of an electron-positron-pair is possible.

2.2. Lead tungstate scintillator

Scintillators in general are materials that emit photons when excited by charged particles or higher energetic photons. The electrons of the material are excited through absorption of the photon and relax at doped activation centres in the material by emitting characteristic radiation in the visible or ultraviolet spectrum. The amount of photons emitted this way is proportional to the energy of the incident particle.

The scintillator crystals used for $\overline{\text{P}}$ANDA are made of a material called PWO-II, being an improved type of $PbWO_4$-crystal, optimised especially for $\overline{\text{P}}$ANDA. The emission wavelength of this scintillator is 420 nm.
The crystals are doped with a small amount of Y- and La-ions to hold against an increasing amount of cation vacancies due to a lead leakage in the production of the crystals [4]. In $\overline{\text{P}}$ANDA, they are wrapped completely in reflective foil. They are additionally equipped with two APDs each, connected by optical grease to the crystal surface and held in place by a plastic cube and a shrinking tube all around. An image of this design can be seen in figure 4.

2.3. Avalanche photodiodes

The abbreviation "LAAPD" accounts for large-area avalanche photodiode, providing a tool to measure small, incoming light intensities with a very high efficiency. The combination of multiple doped semiconductor-layers enables the generation of charge carriers in an intrinsic absorption layer and the multiplication of these carriers by means of the avalanche effect occuring in p-n-diodes.
The general operating principle of a Si-APD will be explained in the following section using the schematic shown in figure 5.



Figure 4: Image of a single detector. Shown are a PWO-crystal lying on top of reflective foil with the readout at the rear, build by two APDs attached to an APFEL. The picture shows a detector like it is planned for the backward endcap of the EMC [5].

Incoming photons pass through the top layer of the APD, which consists of an anti-reflective material (in this case silicon-nitride), to reduce losses at the interface. After passing the p^{++}-layer unaffected, photons will be absorbed in the p^{+}-layer and generate an electron-hole pair. Due to an applied voltage between the electrodes at the p^{++}-layer and the lower n^{++}-layer, these charge carriers are accelerated towards the electrodes. In the multiplication area (denoted by n^{++}(Hamamatsu)), the accelerated electrons can in turn generate secondary electrons through an impact ionization, which leads to the so-called "avalanche effect", multiplying a small incoming signal significantly and enabling even the detection of single photons, if the bias voltage between the electrodes is high enough.

2.4. APFEL

The ASIC for $\overline{\text{P}}$ANDA front-end electronics (APFEL) is an ASIC (application-specific integrated circuit), specifically designed for the needs of the $\overline{\text{P}}$ANDA-EMC readout. It acts as a low-noise, low-power-consuming preamplifier, which is directly attached to the APDs and is responsible for amplifying and shaping the signals, that are delivered by the APDs. Due to the operation temperature of $-25\,^{\circ}\text{C}$, the power consumption of the preamplifier unit has to be minimised to achieve a small

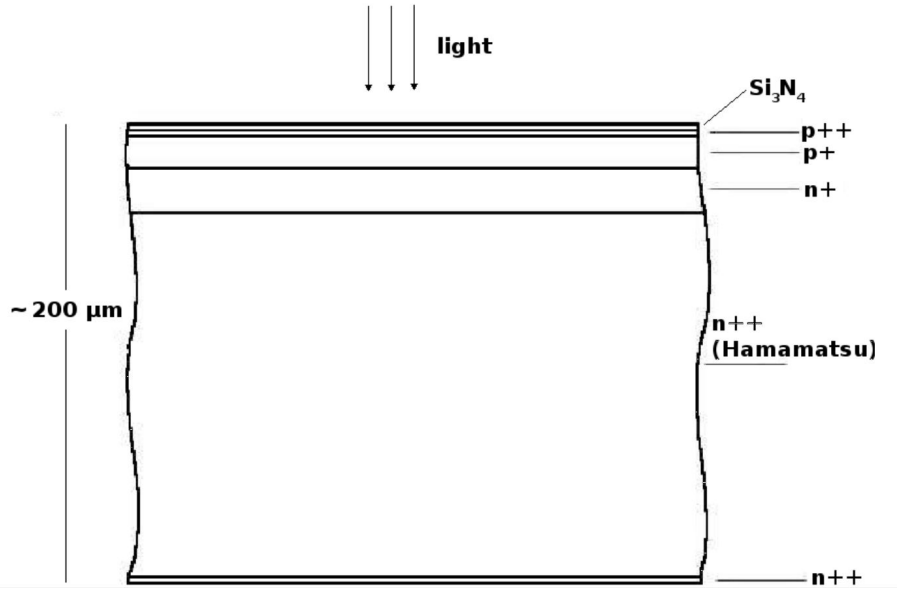

Figure 5: Schematic of a Si-APD with reverse structure. From top to bottom, six layers can be seen: a Si_3N_4 anti-reflective layer, a p^{++}-layer as electrode, p^{+}-layer as absorption-zone, n^{+}-layer as first multiplication area, n^{++}-layer(Hamamatsu) as second multiplication area and the lower n^{++}-layer as electrode [4].

temperature gradient within the scintillators. Additionally, the required maximum single crystal threshold of the experiment is at 3 MeV, which means that the noise level of the preamplifier must be particularly low. A schematic of the layout of the designed APFEL-ASIC is shown in figure 6, it should be noted here, that every APFEL has two inputs, one for each of the APDs. These inputs are split into a high and a low gain branch to achieve a large dynamic range.

The reference voltages for the shaping stages (shown in green in the schematic) can be controlled externally through modification of the four DAC-values, to adapt the dynamic range to the varying ambient temperature. The APFEL has two output stages per APD, where the second output respectively, is emitted with an additional amplification selectable between a factor of approximately 12 and a factor of approximately 24. This second output is called the High-APD-gain branch of the APFEL, while the not amplified output is designated as Low-APD-gain.

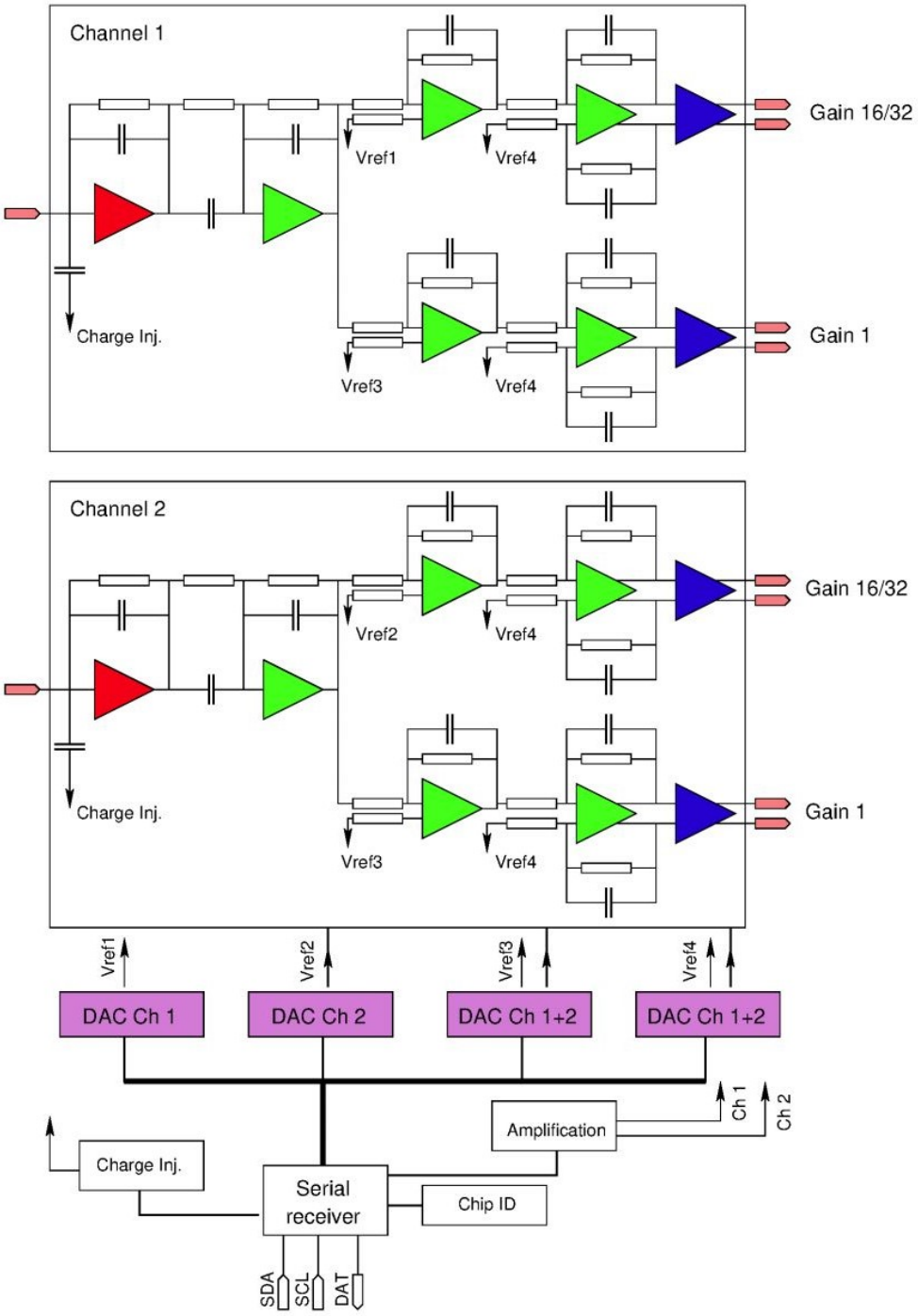

Figure 6: Schematic of the APFEL-layout. The red OpAmps act as preamplifier, the green ones build the shaping stage and and can be controlled by modifying the four DACs, while the blue OpAmps form differential output drivers [3].

2.5. $\overline{\text{P}}$ANDA SADC

The readout of the output signals emitted by the APFELs is executed by a sampling analog-to-digital converter (SADC). The SADC is also developed specially for the needs of the $\overline{\text{P}}$ANDA-experiment and is formed in principal by eight ADC units with eight channels each, controlled and evaluated by two field-programmable gate-array (FPGA) chips plus some infrastructure. The $\overline{\text{P}}$ANDA-SADC was designed by Pawel Marciniewski from the University of Uppsala and uses currently two Kintex-7 FPGAs from Xilinx [6]. An image of the layout is shown in figure 7.

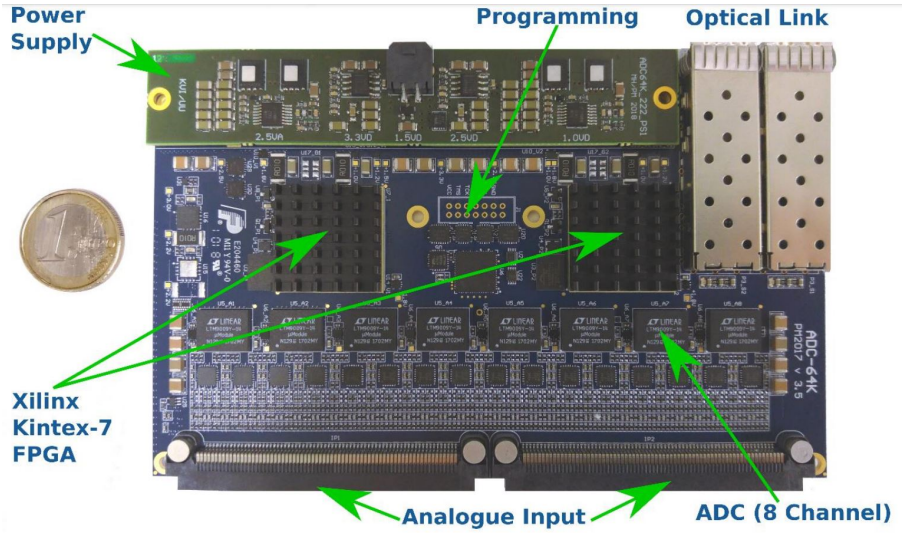

Figure 7: Picture of the $\overline{\text{P}}$ANDA-SADC. The FPGAs and ADCs are highlighted, as well as input, output, power supply and FPGA-programming port [6].

The $\overline{\text{P}}$ANDA-SADC has two times 32 differential inputs with an input range of $\pm 2.2\,\text{V}$, runs with a sampling rate of 80 MHz and uses a 14-bit word length.
The SADC can be configured in various ways to adapt to the needs of certain measurements. It can be triggered on any or all of its input channels, with trigger thresholds, that can be set for every channel separately. The WaveformShift-option gives the possibility to shift the signal relative to the trigger. This shift is set to 250 for the majority of measurements in this thesis, so that the measured signals are in the middle of the 512 samples long trace. Additionally, a WaveformStretch-option can be set, which extends the temporal trace length, by averaging $x + 1$ samples, where x is the Stretch-parameter. When set to 1, the SADC will average two values

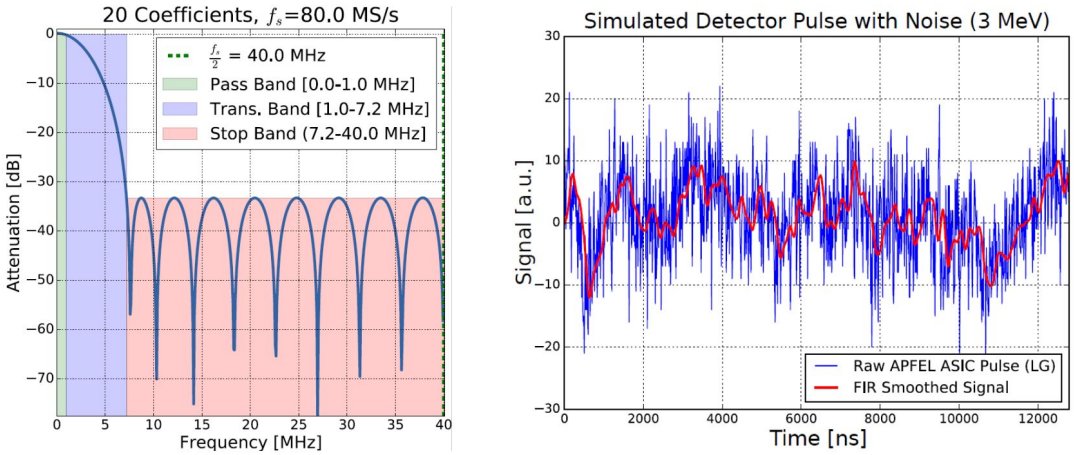

Figure 8: Pictorial representation of the FIR. The left picture shows the attenuation behaviour of the filter and the right picture a trace after processing by the FIR. Picture taken from [6].

and store them as one sample, which results in a trace, that is still 512 samples long, but accounts for double the amount of time (12.5 µs). The Stretch-option is shut off for the majority of the measurements in this thesis.
FPGAs in general are integrated circuits housing several different logic blocks (formed e.g. by look-up tables and flip-flops), input/output ports and routing. The speciality of FPGAs is that the configuration of logic blocks and the routing between them can be configured by users, utilising a hardware description language (HDL) to adapt the FPGA to their individual needs.
The FPGAs build in the $\overline{\text{P}}$ANDA-SADC gather data from the ADC-units (four eight-channel ADC-units that add up to 32 different channels) by means of a de-serializer and applies a feature-extraction (FEx) on the data, if needed.
This feature-extraction algorithm was developed by Oliver Noll from the Johannes Gutenberg-Universität Mainz and will be explained briefly in the following. A first noise-filtering is applied via a finite-impulse response filter (FIR), where high-frequency noise above 7.2 MHz is removed and signals between 1 and 7.2 Mhz are diminished. In figure 8, a pictorial representation of this filter is shown.

The acquisition of the signal amplitude is then realised by means of the signals derivative. The multiplication of the first derivative with a Heaviside function applied to the first derivative results in the function denoted by D^*_{inv}. It is the negative first derivative of the falling edge of the original signal. When added to the

first derivative, the resulting function D_s describes just the first derivative of the rising edge of the trace as far as the peak. The integration of this function yields a signal form, that matches the original trace up to the peak of the signal. The whole process is pictured in image 9.

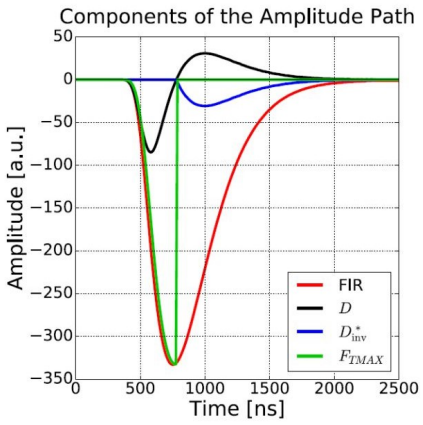

$$D[i] = T[i] - T[i-r]$$
$$D^*_{\text{inv}}[i] = -\Theta(-D[i]) \cdot D[i]$$
$$\Theta(x) \mapsto \begin{cases} 0: & x < 0 \\ 1: & x \geq 0 \end{cases}$$
$$D_s[i] = D[i] + D^*_{\text{inv}}[i]$$
$$D_s[i] \mapsto \begin{cases} F_{TMAX}[i] = F_{TMAX}[i-1] + \frac{D_s[i]}{r} & : D_s[i] < 0 \\ F_{TMAX}[i] = 0 & : D_s[i] = 0 \end{cases}$$

Figure 9: Description of the amplitude extraction algorithm of the feature extraction by Oliver Noll. Picture taken from [6].

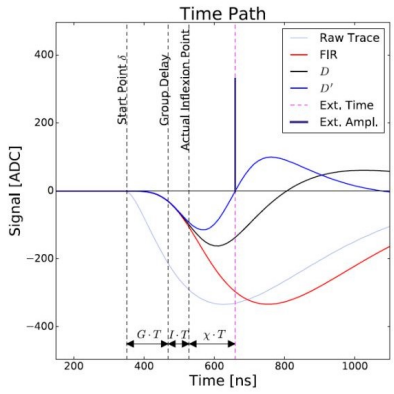

$$f(x) = -A \cdot e^{\frac{-N(x-\delta)}{\tau}} \cdot \left(\frac{x-\delta}{\tau}\right)^N$$
$$f''(x) = 0$$
$$I = \frac{\tau(\sqrt{N}-1)}{\sqrt{N}}$$ Theory inflexion point
$$T_0 = \delta + I$$
$$T_0 = i_0 + \frac{D'[i_0]}{D'[i_0] - D'[i_1]}$$ Between sample interpolation

D is already the first derivative.
Thus, D' is the second one

Figure 10: Description of the time extraction algorithm of the feature extraction by Oliver Noll. Picture taken from [6].

The time-extraction is also realised via derivatives. By calculating the inflexion point via the second derivative and interpolating between samples, the time of the signal can be determined very accurately. A representation of the time extraction algorithm is shown in figure 10. When using this feature-extraction algorithm, the

user can modify several parameters to configure the analysis. One of these is the hit-detection threshold. The feature-extraction has an included event-selection by means of a hit-detection weight function, that considers the rise time, signal height and width of a signal and is sensitive to APFEL ASIC pulse-like signal structures.

3. Experimental Setup

A 3 × 3 $PbWO_4$ Matrix (PWO-II type) with close-to-final readout electronics including the APFEL and the 80 MHz $\overline{\text{P}}$ANDA-SADC, were used. The used crystals are rectangular crystals matching the crystals for the backward endcap with a length of 200 mm and a sqaure front face with 24.4 mm side length. The crystals are wrapped in reflective foil of the type "Specular Film DF2000MA", coupled with APDs with optical grease and are fixated with shrinking tubes. As the $\overline{\text{P}}$ANDA Target calorimeter will be operated at a temperature of −25 °C, the setup was additionally housed in a thermally insulated aluminium box, cooled to the same temperature by a cooling machine. In this thesis, the detectors are numbered from top to bottom and from left to right, when facing the beam as shown in figure 11.

3.1. Detector matrix

The measurements were carried out using a matrix of 3 by 3 crystals. All crystals used for the $\overline{\text{P}}$ANDA-experiment are enumerated by the manufacturer and the identification numbers of the utilised crystals in the matrix are shown in table 2. The optical coupled APDs have an active area of (7 × 14) mm^2 and were developed especially for $\overline{\text{P}}$ANDA(Hamamatsu S8664-1010SPL). The APDs went through the full $\overline{\text{P}}$ANDA screening process where their gain-to-bias-voltage characteristics are determined. Hence, the IDs of the APDs with the respective detectors are also listed in table 2. It is noteworthy, that the terms "left" and "right" refer to the position of the APD at the rear of the detector, when facing the rear and the pin connectors of the APD are orientated to the top of the crystal. For better understanding, this is also shown again in figure 11.

To interpolate the voltage to gain data from the screening process, the Miller-function was used:

$$M(V) = \frac{1}{1 - \left(\frac{V}{p_0}\right)^{p_1}} + p_2, \tag{8}$$

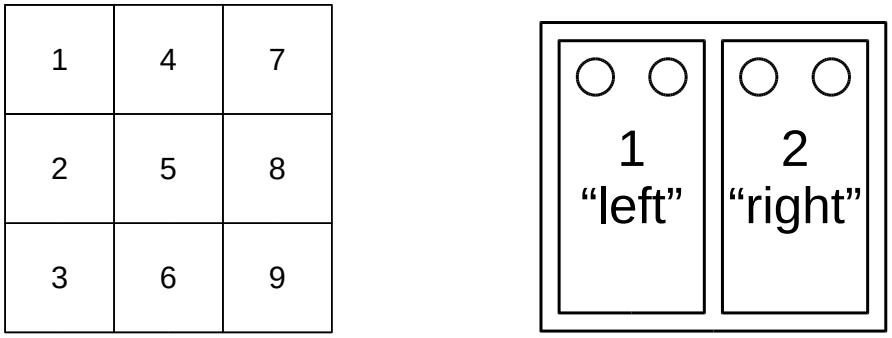

Figure 11: Schematics of detector- and APD-positioning. **Left:** Numbering scheme of the detectors in the matrix. The perspective is facing the beam. **Right:** Schematic drawing of the position of the APDs on a PWO-crystal. The drawing is made from top view on the APDs and the circles in the upper area of the APDs represent the pin connectors of the APDs. The APD with the number 1 is denoted with ”left” and the one with number 2 as ”right”. The drawing is not true to scale.

Table 2: Manufacturer IDs of the utilised APDs and crystals with their respective detector. Two APDs were used per detector.

Detector #	Crystal ID	APD ID left	APD ID right
1	1931	1315014672	1315014673
2	1932	1402015184	1402015185
3	1933	1408015633	1408015634
4	1934	1410015804	1410015805
5	1935	1410015853	1410015854
6	1936	1410015855	1410015856
7	1937	1412015992	1412015993
8	1938	1503016674	1503016675
9	1939	1601016790	16010167091

whereas $M(V)$ is the resulting gain, V is the bias voltage, p_0 a fit parameter representing the breakdown voltage and p_1 as well as p_2 being additional fit-parameters [7]. A plot of a Miller-Fit on screening data is shown in figure 12.

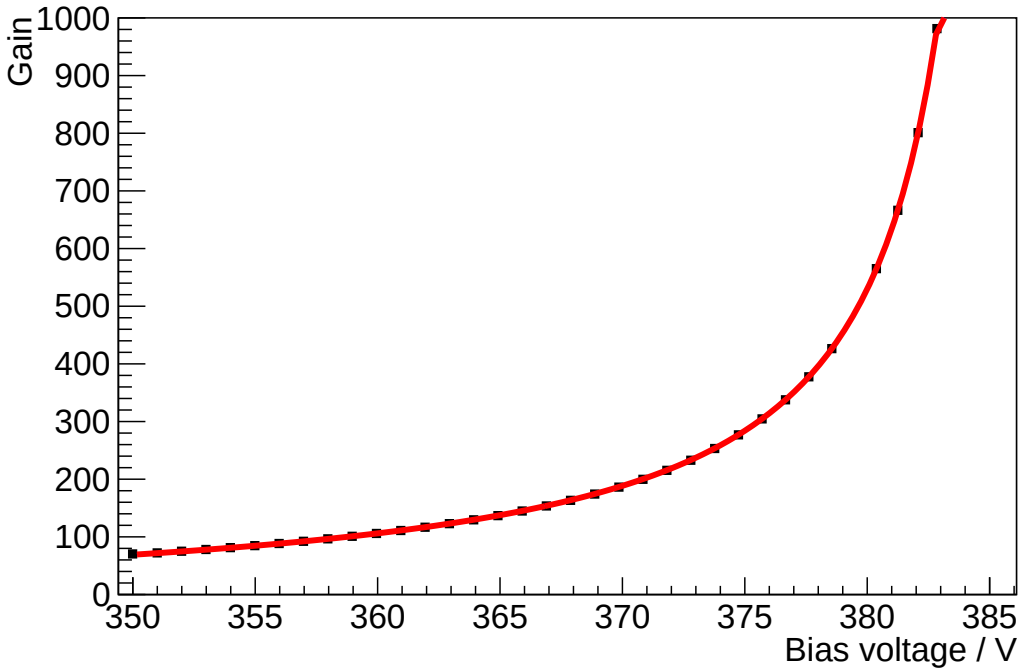

Figure 12: Miller fit on an APD-gain vs. bias voltage data set of APD 1601016742.

The obtained bias-voltages for the intended gains of 150, 300, 400 and 500 are listed in table 4.
In the later analysis, it became apparent, that two of the listed APDs are actually not in the matrix. These are the APDs with IDs 1412015992 and 1412015993, expected to be on detector 7. Instead of those, the APDs with the manufacturer's ID 1415016226 and 1601016742 are assumed to be coupled to this detector. As the orientation of those two APDs is in turn not known, table 3 shows the gain, at which they would operate, if provided with the bias voltages that were set according to table 4.

Table 3: Gain of the actual APDs on detector 7, when supplied with the bias voltage of the previously assumed APDs.

Assumed APD		**APD# -226 Gain**	**APD# -742 Gain**
APD #	Gain	Gain	Gain
-992	150	156	155
-992	300	310	315
-992	400	417	427
-992	500	523	543
-993	150	176	177
-993	300	386	398
-993	400	552	579
-993	500	740	798

Table 4: Required bias voltages for the desired APD-gains. The table shows which bias voltage has to be applied to a specific APD, so that a gain of 150, 300, 400 or 500, respectively, is achieved with this APD. All voltages are given in Volts.

APD ID	$\mathbf{U}_{150}$	$\mathbf{U}_{300}$	$\mathbf{U}_{400}$	$\mathbf{U}_{500}$
1315014672	389.612	398.979	401.597	403.217
1315014673	389.685	399.012	401.614	403.233
1402015184	366.762	375.741	378.203	379.727
1402015185	369.193	378.363	380.918	382.509
1408015633	367.906	376.965	379.515	381.108
1408015634	366.229	375.244	377.747	379.302
1410015804	368.833	377.945	380.401	381.192
1410015805	368.801	377.931	380.481	382.069
1410015853	368.367	377.263	379.789	381.365
1410015854	372.260	381.399	383.947	385.532
1410015855	369.760	378.913	381.457	383.040
1410015856	368.966	378.101	380.632	382.204
1412015992	367.040	376.026	378.563	380.150
1412015993	369.096	378.031	380.516	382.061
1503016674	367.683	376.880	379.438	381.030
1503016675	366.223	375.380	377.912	379.484
1601016790	366.103	375.128	377.613	379.153
1601016791	366.059	375.047	377.538	379.086

3.2. Readout electronics

The front-end readout electronics consists of various devices, ensuring an efficient, low-noise and loss-free data-handling. The response of the APDs is fed into the attached APFEL-ASIC, which transfers the signal towards a SADC. Some additional front-end electronics are placed between the APFEL and the SADC, almost similar to the later $\overline{\text{P}}$ANDA-experiment. They consist of backplanes, supplying the APDs with high-voltage, bufferboards, which are fed by two backplanes respectively and distribute the data to eight RJ-45 ports, one for each APFEL. These two devices are shown in figures 13 and 14.

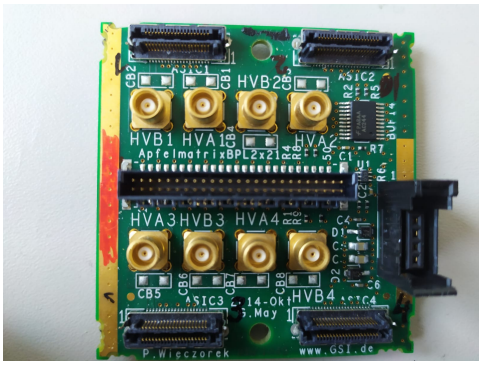

Figure 13: Backplane of the readout electronics, also known as "Apfelmatrix". Located in the four corners are connectors to the APFEL-ASICs, the golden connectors are inputs for the high-voltage supply of the APDs, the central connector forms data output, control input and link to the bufferboard and the low voltag power supply for the APFELs is located at the lower right side of the PCB.

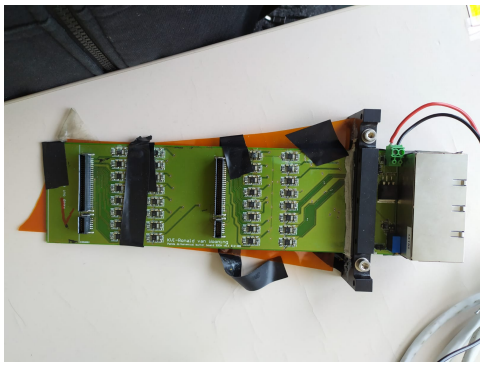

Figure 14: Bufferboard of the readout electronics. On the right side, a block with eight RJ-45 ports can be seen, which acts as output and is connected to the SADC. Two backplanes can be connected by the large connectors in the middle and on the left side of the board. The small connectors beneath them act as busses for communication and allow the configuration of the APFEL-ASICs (e.g. changing the DAC-values, and switching between times 16 and times 32 amplification)

In figure 15, a picture of the complete readout-chain is displayed.
Despite one backplane having four ports, four of these backplanes were needed, due to certain space-constraints of the setup. The detectors 2,3,5 and 6 were plugged together in one backplane. 8 and 9 were plugged in a second one, 1 and 4 in the third and detector 7 was solemnly plugged in the last backplane. One bufferboard in turn managed the first two backplanes, while a second bufferboard managed the last two, in the previously given order.

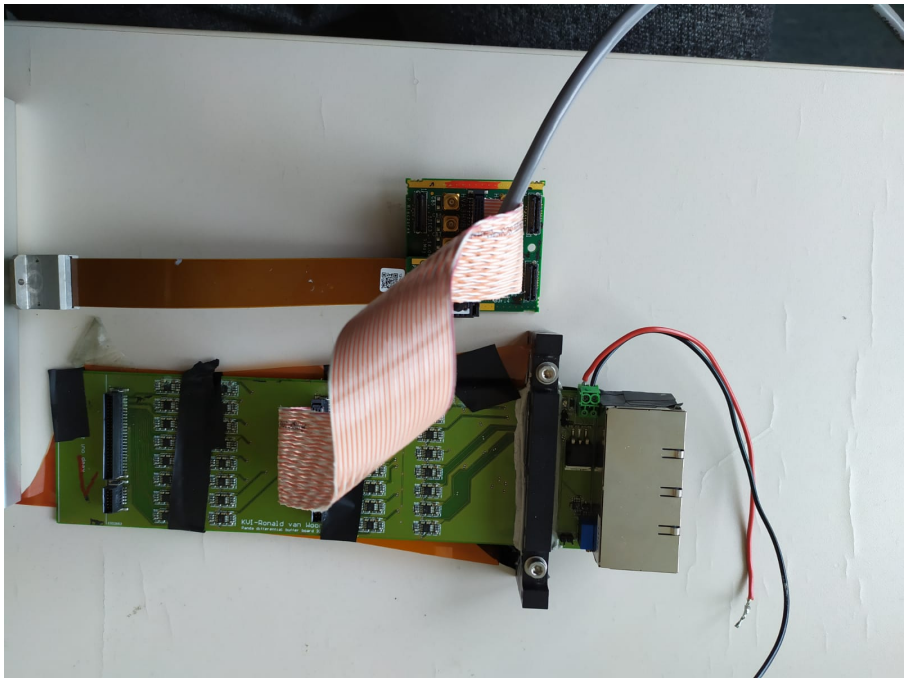

Figure 15: Picture of the complete front-end. On the leftmost side, an APFEL-ASIC inside its aluminium housing, can be seen. The attached Flex-PCB leads to an Apfelmatrix which is in turn, via the central connector, linked to the bufferboard.

3.3. Cooling and Temperature Control

To operate the crystals with high light yield and the APDs at a low noise level, the temperature must be kept relatively low. The optimal operating temperature for $\overline{\text{P}}$ANDA was determined to $-25\,^{\circ}\text{C}$ and so the experimental setup had to be cooled to this temperature, too, for comparability.
A large aluminium box was designed to house the whole experiment and ensure a temperature-stable environment. In figure 16, a drawing of the box is displayed, although the image was made by Lukas Nies for his master's thesis and the actual setup is therefore slightly different.

The inside of the aluminium box is clad with thermal insulation material and there is another aluminium frame set inside that is removable for easier access and set-up of experiments. Attached to the sides and the bottom of this aluminium frame

3.3 Cooling and Temperature Control

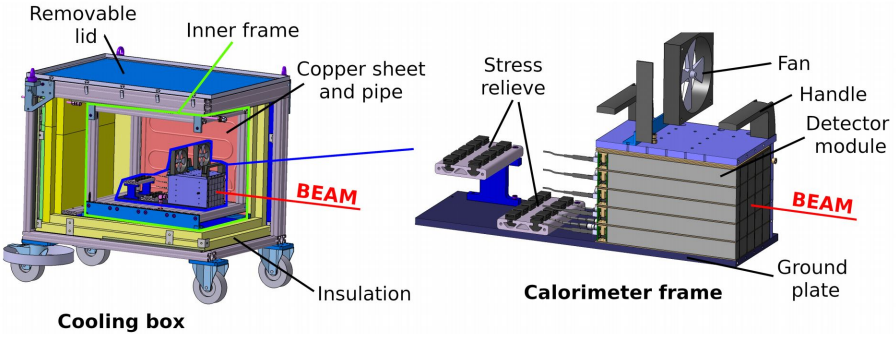

Figure 16: Left side: Aluminum housing for temperature stabilization and effective cooling. The cladding inside the box is made of a thermal insulator and placed inside is another aluminium frame, that is removable for easier set-up of experiments. Also displayed is one of the large copper plates with pipe-meanders, sitting on the right side looking from the beam. A similar sheet is placed on the opposite side and one on the bottom under the aluminium frame.
Right side: Drawing of the detector matrix. Consider that the shown image does not display the actual matrix used. In the utilised setup, the top-most layer of crystals had been removed, as well as the stress relieve for steric reasons. Additionally, only the nine central crystals shown her have been actually read-out. Image taken from [8].



Figure 17: Interior of the cooling box. On the right side, three nozzles can be seen. The central one is the inlet for dried air, while the other two can be used as inlet/outlet for cooling liquid.

are large copper plates with meanders made of copper pipes. These pipes were flushed with cooling liquid from the outside and the large thermal conductivity of copper ensures an efficient and stable, cooled environment. Through a small nozzle, the box can additionally be flooded with dried air. The external dried air is guided through some meanders at the bottom copper plate to pre-cool the air that floods the box. The box should always be flooded with dry air before cooling, as condensing humidity can damage electrical devices inside the box.



Figure 18: Utilised cryostat from Julabo. The top cover was additionally insulated, because of freezing humidity at the cover and on the liquid outlets, that inhibited the cooling capabilities.

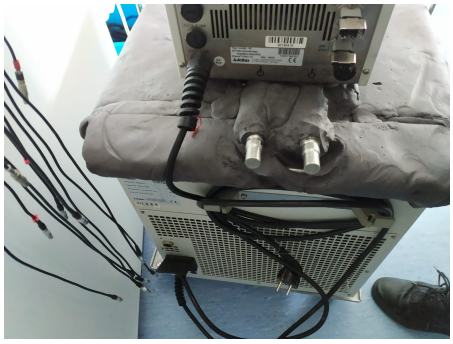

Figure 19: Rear view of the cryostat. The outlets are insulated to prevent freezing humidity.

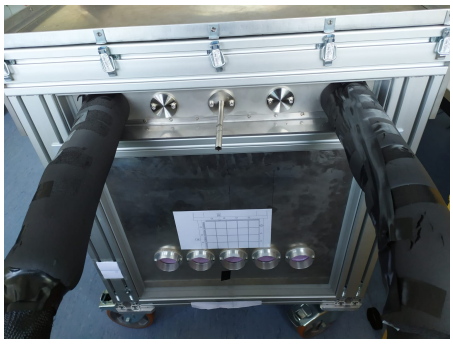

Figure 20: Rear view of the cooling box. The cooling liquid inlets are reinforced with steel rods and wrapped inside insulation material to prevent freezing humidity.

A picture of the interior of the cooling box can be seen in figure 17. The liquid used in the experiment was a 60 % ethanol-water-mixture pumped through the meanders inside the box by a FP51-SL ultra-low refrigerated-heating circulator from Julabo which will be in the following referred to as ”cryostat”. The cryostat is capable of cooling pure ethanol down to −50 °C and has a cooling capacity of 1 kW down

Table 5: Temperature-control data at the start of the beamtime. shown are IDs of the sensors, their position and the temperature in this area.

Sensor #	Position
1	PWO-matrix, bottom
2	top of the aluminium frame
3	PWO-matrix, top
4	bottom of the aluminium frame
5	Raspberry Pi
6	At copper meanders
7	Backplane no. 2
8	Central APFEL

to a temperature of $-20\,^{\circ}\mathrm{C}$. In the experiments, the ethanol solution was cooled to $-30\,^{\circ}\mathrm{C}$ to achieve a stable temperature of $-25\,^{\circ}\mathrm{C}$ inside the box. In figures 18 and 20 the utilised cryostat is displayed, as well as a rear view of the cooling box. Additional thermal insulation can be seen, as problems occurred with freezing humidity.
To monitor the actual temperature inside the aluminium box, several temperature sensors were attached to the inside of the cooling box. The temperature sensors are made of chromel and alumel, commonly known as type k thermocouple. The positions of the temperature sensors inside the box are listed in table 5.

3.4. Light pulser

For reference measurements, a light pulser system was installed. A light pulser with variable intensity, frequency and light colour was set up beside the cooling box and a light fibre bundle was attached to it. The light fibres were attached to the crystals one for each and another fibre was put to a reference detector inside the cooling box.

An image of the used light pulser can be seen in figure 21. It has been designed by the Bochum $\overline{\mathrm{P}}$ANDA group. Its light-pulses generate signals after being processed by the APFELs that are similar to those from PWO-II scintillation. The utilised light fibres are attached to the crystals via small holes at the front and by applying optical grease at the interfaces of crystal/light fibre and light fibre/pulser a good



Figure 21: Interior of the light pulser. The pulser was designed by the Bochum $\overline{\text{P}}$ANDA group. The light mixer crystal provides a good light homogeneity.



Figure 22: Picture of the front of the detector matrix with light fibres attached to the crystals. The fibres are inserted in small holes and fixated with a plasticine.

optical coupling is established.

The reference detector inside the cooling box consists of a Plexiglas®-block with a light fibre attached to the front and a large square APD attached to the rear. The APD is equipped with a Basel-type preamplifier and is supplied with 395 V. The supply voltage of this APD and the amplification factor of the preamplifier will not be changed, giving a constant basis to calibrate later measurements to each other.

3.5. MAMI

The "Mainzer Mikrotron" is an accelerator facility at the Johannes Gutenberg University in Mainz. It is capable of accelerating electrons to up to 1.5 GeV with an energy spread of 110 keV. Additionally, a high energetic photon-beam can be generated in the tagger hall A2. The electrons are guided against a copper radiator, creating photons as bremsstrahlung in beam direction. Lead cylinders with several differently-sized holes enable an improved collimation of the tagged photons.

3.5 MAMI

A 1.8 T dipole magnet behind the radiator deflect the electrons after the photon-production and makes the determination of the kinetic energy of the electrons possible, as it directly affects the bending radius of the electrons flight curve. A larger electron momentum will result in a smaller bending radius and by observing the impact position on a focal plane of 353 plastic scintillators, the bending radius and therefore the residual momentum of the electrons can be determined. This in turn provides a tool to designate the energy of the generated photon, due to it being the difference of impeding electron energy and the energy after photon-generation. The energy resolution of this process and therefore of the tagged photons is 2 MeV for up to 820 MeV of incoming electron energy and 4 MeV for higher energies.
A schematic of the MAMI-accelerator with the explained photon tagger is shown in figure 23.

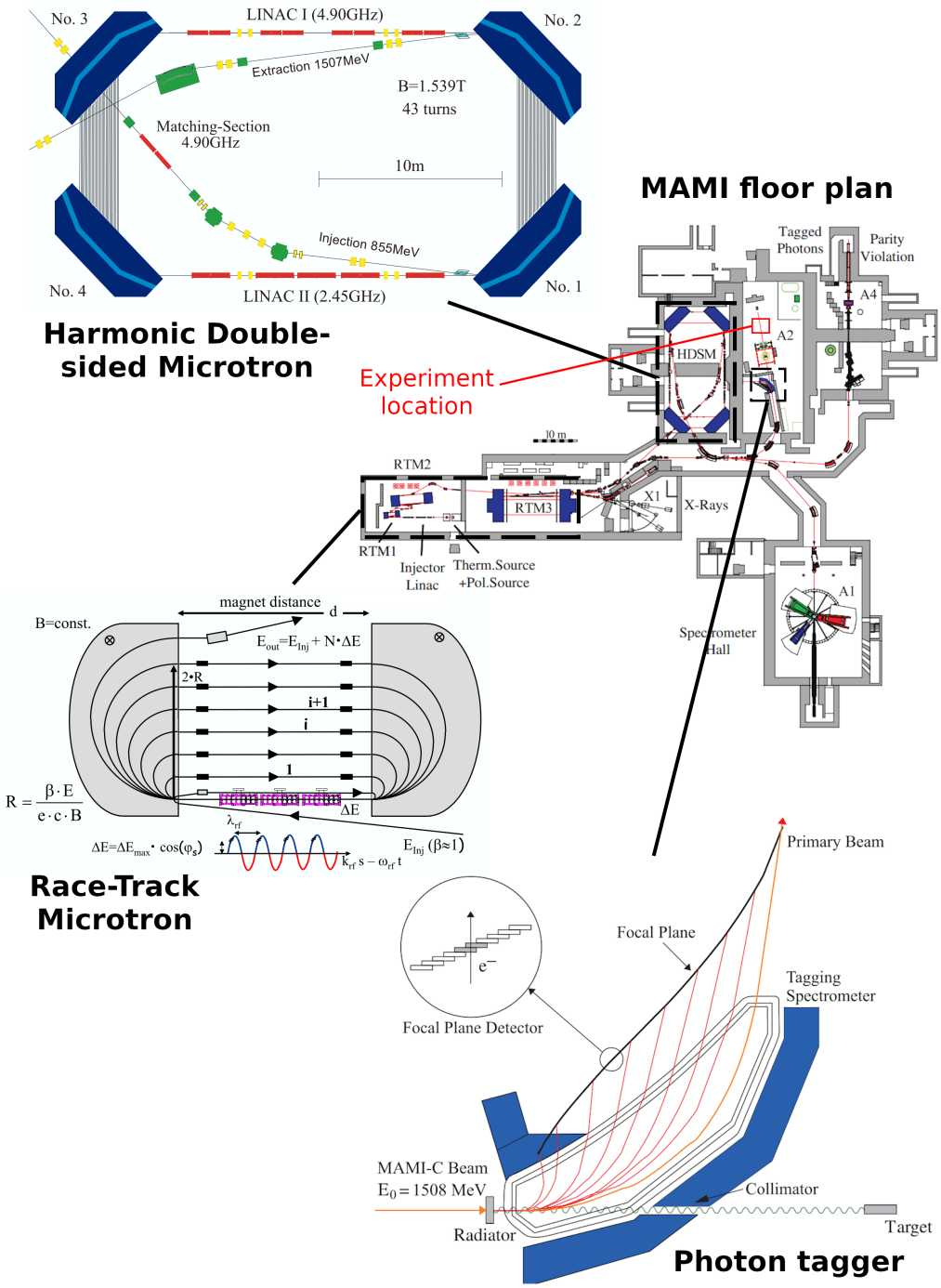

Figure 23: Layout of the MAMI accelerator facility. Shown are the two microtron-systems responsible for the acceleration of the electrons, at the bottom, a schematic of the photon tagger with different flight curves for different kinetic energies of the electrons are shown. On the floor plan on the right side, the layout of the facility can be seen. The experiments for this thesis have been conducted in hall A2. Courtesy by [8].

3.6. APD-gain setups

The 32 inputs of the used $\overline{\text{P}}$ANDA-SADC were fed with different signals, depending on the settings under test. For the High-APD-gain setup, the first 20 inputs were occupied by the High-APD-gain signal outputs of the nine APFEL of the matrix (two outputs each) plus the two Low-APD-gain outputs of the central detector. The remaining twelve SADC-inputs were fed with the eleven used tagger-channels plus a logical OR over all the used tagger-channels, to provide a common trigger.
For the Low-APD-gain setup (LG), all inputs that were connected with High-APD-gain detector outputs are swapped with their respective Low-APD-gain outputs and vice-versa.
The configuration is shown in table 6 and a scheme of the discussed setup is shown in figure 24.

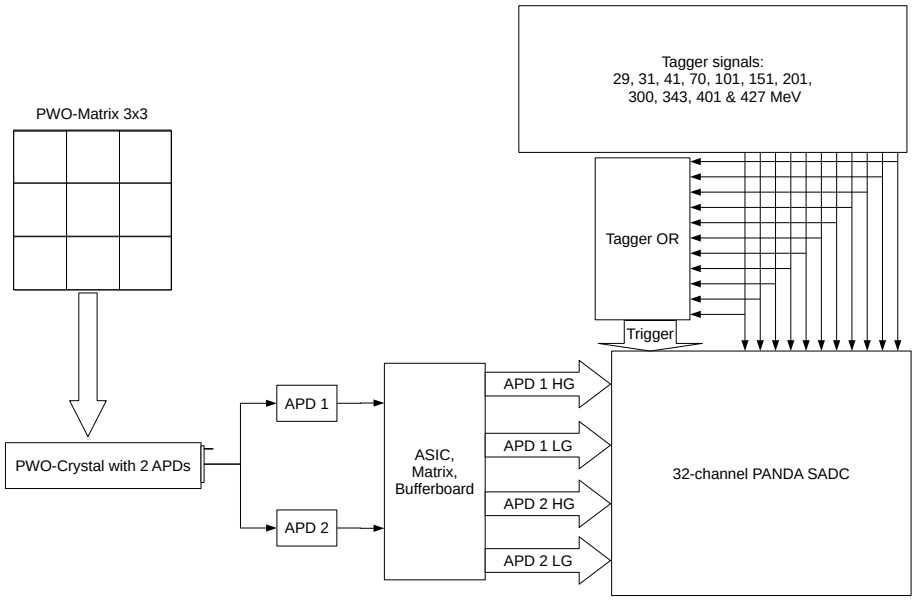

Figure 24: Scheme of the front end electronics with detectors and tagger channels. The eleven tagger channels are fed into the SADC and a logical OR, whose output is also fed into the SADC and provides a common trigger. Additionally, the SADC is provided with the High-gain or Low-gain outputs of the 18 APDs, plus the respective other outputs of the central detector.

Table 6: Allocation of SADC inputs to signal sources. The detectors are indicated with two numbers, the first standing for their position in the matrix (1-9), whilst the second represents the position of the APD on the crystal (1-2) respectively, as well as an indicator for the APFEL readout-branch (HG or LG). The listed tagger channels are shown together with the energy of the respective, incident photons.

SADC-input	LG setup	HG setup
0	Detector 2 2 LG	Detector 2 2 HG
1	Detector 1 1 LG	Detector 1 1 HG
2	Detector 4 2 LG	Detector 4 2 HG
3	Detector 3 1 LG	Detector 3 1 HG
4	Detector 2 1 LG	Detector 2 1 HG
5	Detector 1 2 LG	Detector 1 2 HG
6	Detector 4 1 LG	Detector 4 1 HG
7	Detector 3 2 LG	Detector 3 2 HG
8	Detector 5 2 HG	Detector 5 2 LG
9	Detector 5 1 LG	Detector 5 1 HG
10	Detector 7 2 LG	Detector 7 2 HG
11	Detector 6 1 LG	Detector 6 1 HG
12	Detector 5 2 LG	Detector 5 2 HG
13	Detector 5 1 HG	Detector 5 1 LG
14	Detector 7 1 LG	Detector 7 1 HG
15	Detector 6 2 LG	Detector 6 2 HG
16	Detector 9 2 LG	Detector 9 2 HG
17	Detector 8 1 LG	Detector 8 1 HG
18	Tagger 100.592 MeV	Tagger 100.592 MeV
19	Tagger 29.473 MeV	Tagger 29.473 MeV
20	Detector 9 1 LG	Detector 9 1 HG
21	Detector 8 2 LG	Detector 8 2 HG
22	Tagger 69.509 MeV	Tagger 69.509 MeV
23	Tagger 41.078 MeV	Tagger 41.078 MeV
24	Tagger 343.496 MeV	Tagger 343.496 MeV
25	Tagger 151.379 MeV	Tagger 151.379 MeV
26	Tagger OR	Tagger OR
27	Tagger 400.501 MeV	Tagger 400.501 MeV
28	Tagger 300.033 MeV	Tagger 300.033 MeV
29	Tagger 200.802 MeV	Tagger 200.802 MeV
30	Tagger 31.331 MeV	Tagger 31.331 MeV
31	Tagger 426.743 MeV	Tagger 426.743 MeV

4. Procedure

The beamtime for data-acquisition was conducted from the 22nd to the 25th of November, 2019. Several front-end settings and APD-gains were tested in combination with different thresholds. Furthermore light-pulser measurements and acquisition of cosmic data was done for later calibration. The temperature stability inside the cooling box was monitored at regular intervals.
Due to the limited amount of SADC-channels, dedicated runs for the low gain (LG run) and the high gain (HG run) branch of the APFEL have been performed with the following APD-gains: 150, 300, 400, 500. An overview is given in table 7

Before the first run and after the setup of the whole experiment, the whole box was flooded with dry air and after one hour the cooling procedure started. The cryostat was set to $-30\,^{\circ}\mathrm{C}$ liquid temperature. The monitored temperatures are shown in figure 25. The jump in temperatures at some electronic parts between 23.11. 12:00 and 24.11. 0:00 is caused by the activation of the front-end. After a short period of time the now switched devices are acclimated and the temperature drops again.
The trigger of the SADC was set on the Tagger OR channel and typically with a trigger threshold of 3000 for the beam measurements.

4.1. Accelerator runs

The first measurements were done with the High-APD-gain setup and an amplification of 16 on the APFELs. Four runs were executed with an APD-gain of 150, 300, 400 and 500, respectively. The DACs were optimised to obtain the maximum

Table 7: Overview of the conducted beam experiments. The data for the LG-runs have been taken in reversed order, starting with 2.4.

HG(×16)-run		**LG-run**		**HG(×32)-run**	
#	APD-gain	#	APD-gain	#	APD-gain
1.1	150	2.1	150	3.1	150
1.1	300	2.2	300	3.2	300
1.3	400	2.3	400	3.3	400
1.4	500	2.4	500	3.4	500

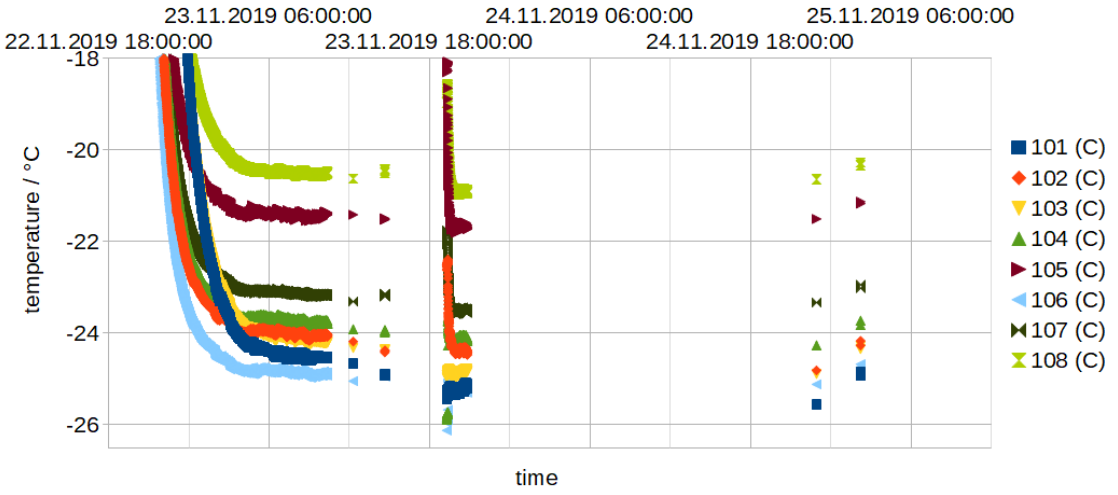

Figure 25: Monitored temperatures over the course of the beamtime. 101 denotes sensor #1, 102 denotes sensor no#2 and so on.

dynamic range for this setting, before the actual measurements happened. Optimization of the DACs was performed by observing every channel of the SADC in a live-view software and activating the light pulser. The DAC-values were changed, so that the light pulser peak in the corresponding APD would have a maximum peak height. A display of the used live-view software with shown light pulser peaks is shown in figure 26.

For an APD-gain of 150, an additional measurement was executed with the SADC-WaveformStretch option set to 1. This accounts for a doubling of the recording time per event with an averaging of 2 samples each. It should be noted, that the beam collimator was changed after the APD-gain 300 run, to get an improved flux at the matrix. The collimator was changed from one with a diameter of 1.5 mm to one with a 4 mm diameter.

Afterwards, measurements with the Low-APD-gain Setup were executed. As before, the DAC-values were optimised and the measurements were taken for APD-gains of 500, 400, 300 and 150, in this order. After about half an hour in the APD-gain 400 run, the beam intensity began to fluctuate. After around half an hour in the APD-gain 150 run, the beam shut down, due to some accelerator-cooling problems. Another five minutes later, the beam went back online, but with a significantly lower intensity. To compensate the missing data, another 30 min measurement was taken later on.

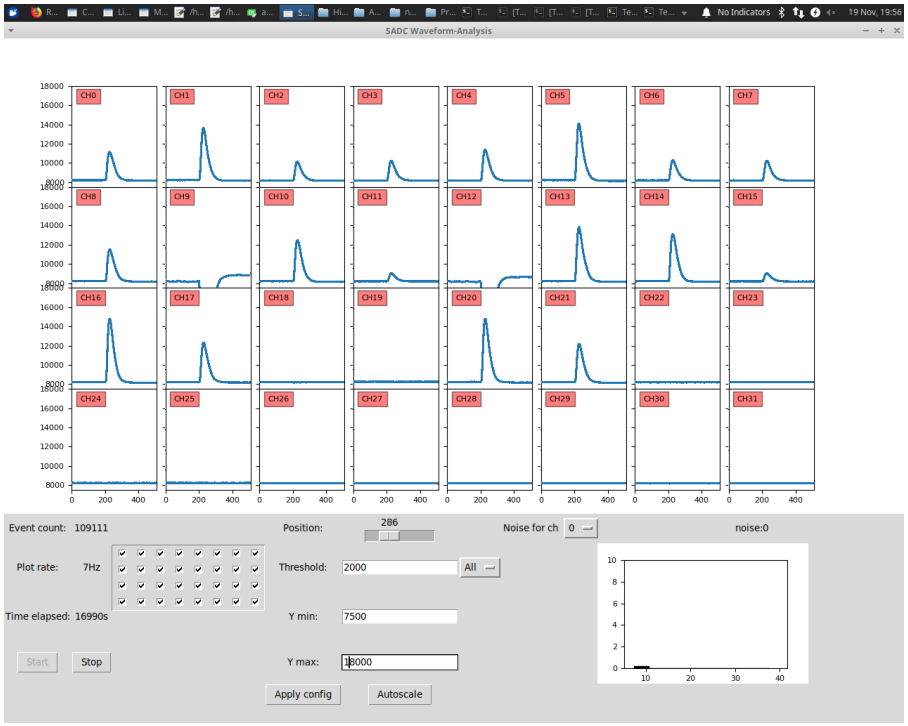

Figure 26: Display of the SADC-readout for DAC-optimisation via the light pulser and the live view software.

The accelerator runs were concluded with four measurement with the High-APD-gain setup at an APFEL high-gain-amplification of 32. Again, APD-gains of 150, 300, 400 and 500 were executed after optimising the DAC-values of the APFELs. For APD-gain 150, another test with the Stretch-option of the SADC set to 1, was made.

4.2. Lightpulser runs

The different settings for APD- and ASIC-gain are summarised again in table 8. Directly after the beam runs, the response of the detector matrix to the lightpulser-signal was measured. Therefore, the input channel 19 in table 6 was fed with the output of the reference detector of the lightpulser system and all other output channels marked with ”Tagger” were excluded from the readout.
Every APD-gain measured beforehand was set again and the setup measured for two minutes, while the light pulser emitted with a frequency of 1 kHz and

Table 8: Listing of the recorded data with its main front-end parameter

ASIC\APD	150	300	400	500
LG(×1)	Beam&LP	Beam&LP	Beam&LP	Beam&LP
HG(×16)	Beam&LP	Beam&LP	Beam&LP	Beam&LP
HG(×32)	Beam&LP	Beam&LP	Beam&LP	Beam&LP
HG(×16)				Cosmic

the intensity of the light pulser was varied. The trigger of the SADC was set on channel 19 (being the reference detector) with a threshold of 2000 SADC-channels.

4.3. Cosmic Radiation run

At the end of the beamtime, cosmic data was acquired for absolute calibration. The cosmic measurements were carried out with an APD-gain of 500 and with the High-APD-gain configuration with an amplification of 16 in the High-APD-gain branch of the APFELs. Only the inputs denoted with "Detector" in table 6 were read out and the SADC was set to trigger on all these channels. After three short test runs with different trigger thresholds, the actual measurement was carried out for 4 hours, the first two hours with a threshold of 500 and the latter two hours with a threshold of 1000 SADC-channels.

5. Analysis

5.1. Raw beam and cosmics data

All raw traces from one APD of the central detector run 1.4 are shown together in figure 27.

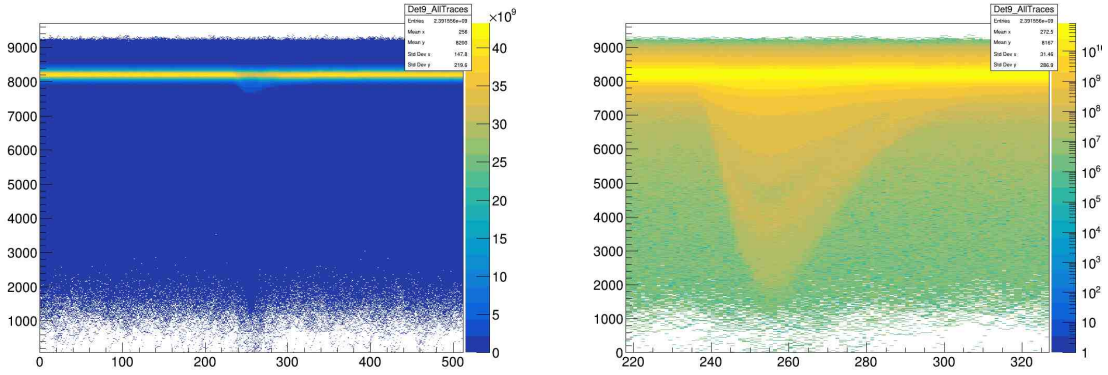

Figure 27: Histogram of all traces of the ASIC-gain 16 and APD-gain 500 run, without any filters or selection applied. The right picture shows the same data in logarithmic for the z-axis.

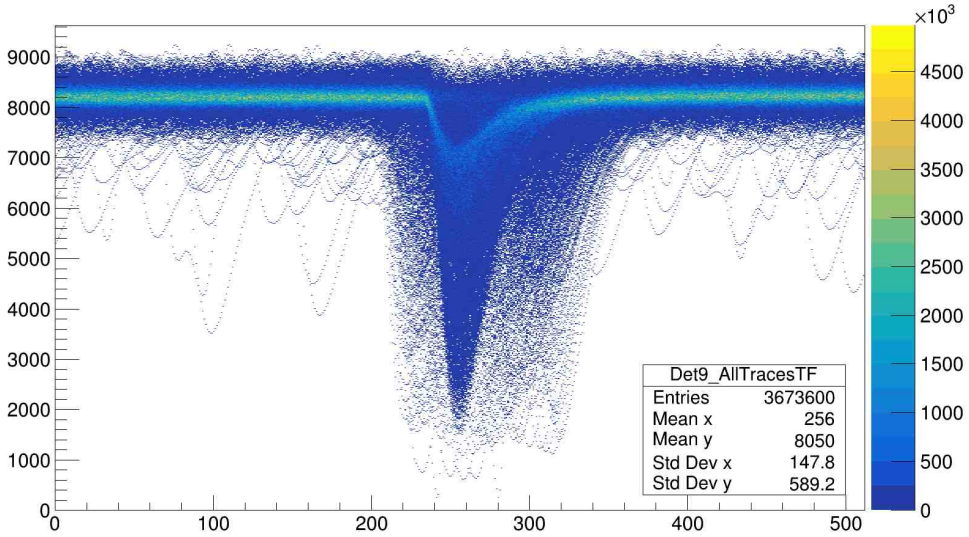

Figure 28: Histogram of all events of the ASIC-gain 16 and APD-gain 500 with a time-filter applied.

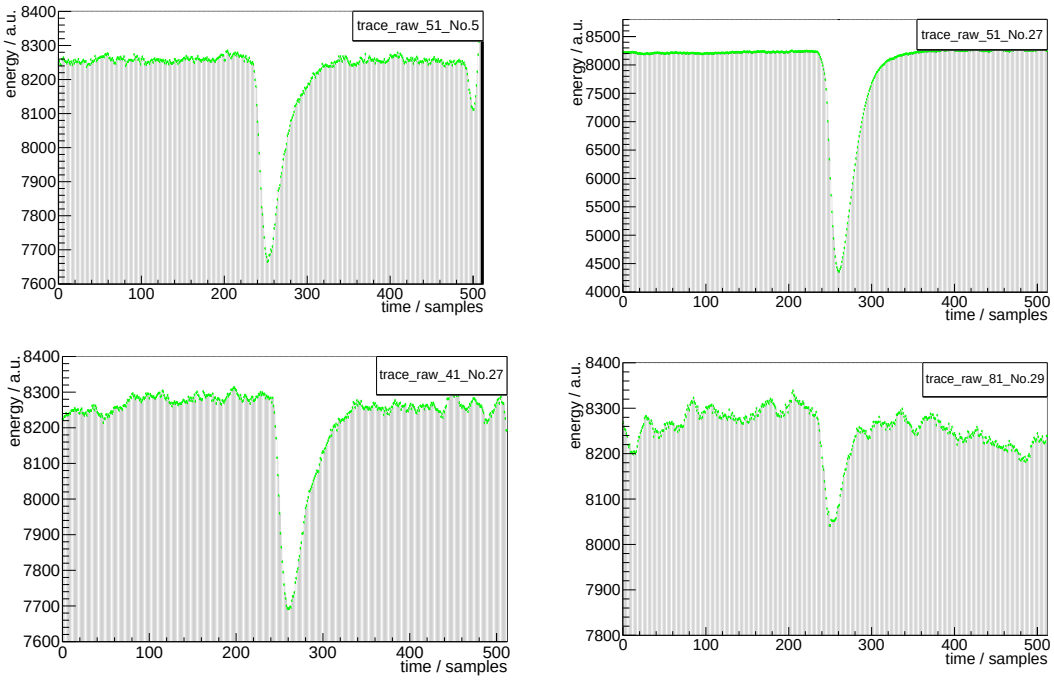

Figure 29: This picture shows four traces of different detectors from the ASIC-gain 16 and APD-gain 500 run. The parameter window shows the corresponding detector and APD. The first digit after "raw" shows the detector, the second digit the position, "1" being left and "2" being right as explained in chapter 3.1. Additionally, the event number is displayed at the end of the title. One time unit on the x-axis is one sample, as the SADC has a sampling rate of 80 MHz, the difference between two samples is 12.5 ns.

To get rid of the large amount of random coincidences in the data, a first event selection by means of the timing was applied. Events of this data set would only be taken into account, if the signal in the trace is under a certain threshold (below the baseline) in a time-window of 220 to 320, as this is the location of the expected signal. The resulting histogram is shown in figure 28.
Looking at several raw traces, it quickly became apparent that noise would be a big problem in the data analysis. Figure 29 shows several single traces.
In contrast, figure 30 shows traces of four different detectors, where large noise occurs. It should be noted, that on the one hand all shown traces were taken at the same time, as apparent from the last number (the "event number") in the title of the parameter window being 37 in all traces. On the other hand the peak height of the noise over the baseline is similar to some of the peak heights of the signals in figure 29. The traces are all measured at an ASIC-gain of 16 and APD-gain of 500.

5.1 Raw beam and cosmics data

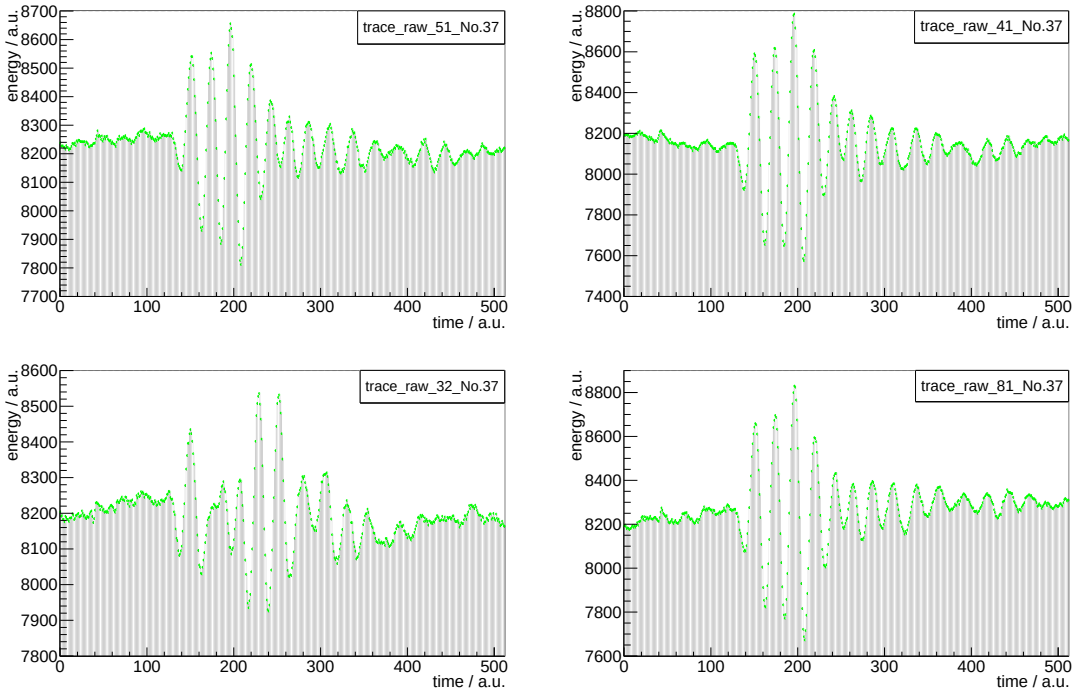

Figure 30: Several traces with occurring noise, belonging to the ASIC-gain 16 and APD-gain 500 run. Noticeably is the last number in the first line of the parameter window being "37" for all shown traces, meaning that the traces were taken at the same time.

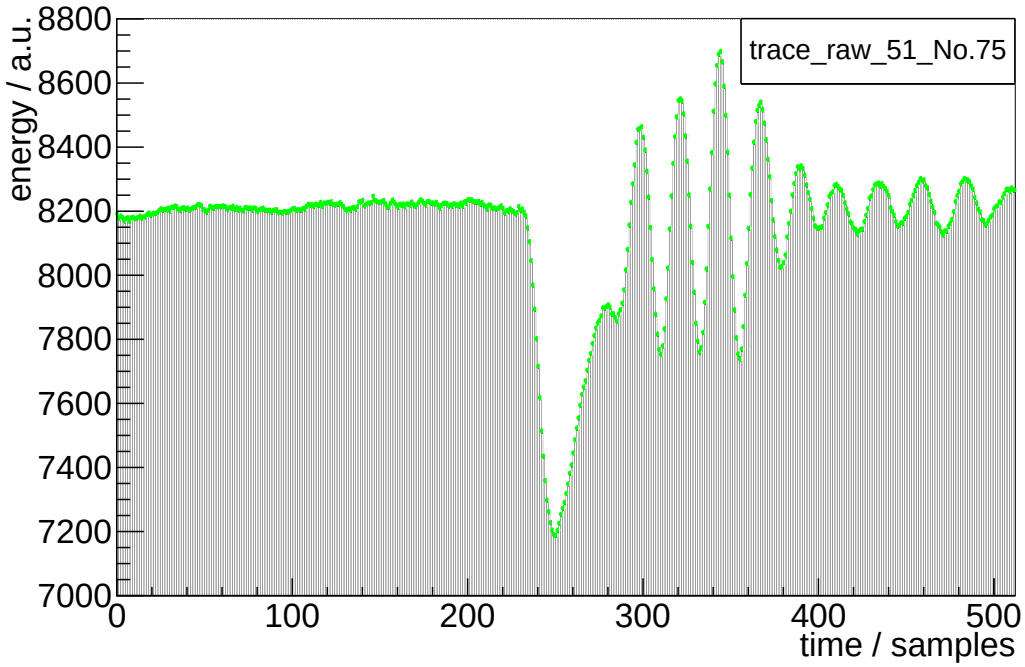

Figure 31: This trace shows a detected cosmic muon, and coincident noise in the same trace. The shown data was taken in the cosmic measurement runs.

Taking a look on the raw traces of cosmic signals, this problem became more severe. The reason for this is the cosmic rate being rather low, at around 2-3/sec whereas the rate of the coincident noise is significantly higher. Additionally, as can be seen in figure 31, the peak height of the noise below a baseline would be more than half of the negative cosmic signal height.
The further analysis was mainly done with the feature-extraction, that was described in chapter 2.5. The software was written in ROOT, which is a C++-framework being developed for data processing at CERN, specially designed for the needs of high-energy physics experiments. The software saves eligible traces with several parameters and values related to the event in a tree-structure The saved results with explanations are listed in table 9.
A simple peak-sensing algorithm was applied as well, to make first assumptions and considerations possible. The algorithm searches in a time-window around the expected peak for a minimum (or a maximum depending on the signal shape) over a baseline. The time-window chosen for this is set between sample 220 and 320, matching the aforementioned first event-selection. The baseline is calculated by averaging all values outside of this window. The algorithm searches for the first extremum, saves the sample number in *Time_sFE*, subtracts the energy from the baseline (or vice-versa) and saves the result as *En_sFE*.
Additionally, a filter was set up with the left APD of the central detector, being channel 9 for the SADC. Here, the energy above the baseline ten samples before and ten samples after the found peak is calculated. The algorithm compares these two values with the energy of the actual peak and will only save the event, if the energy of the peak is higher, to prevent the misidentification of a rising or falling edge at the borders of the window as a signal. Lastly, the found energy has to be above a certain threshold, to be accepted. This was set to a value of 50, which is just enough to sort out all traces, which have no signal or noise at all. All coincident traces of an event will only be saved, if this condition is fulfilled.
The feature-extraction differs from the described algorithm when dealing with cosmic data. Here, the algorithm will search in the whole trace for a maximum and there is no threshold applied, as the cosmics were expected to have a very small signal height and not be centred in the time window. Furthermore, the baseline is constructed by averaging all samples of the whole trace.

Table 9: Results saved by the analysis software and explanation of their purpose. The variables from *APD-gain* to *FE_Threshold* are saved in *MeasInf*.

Variable	Description
MeasInf	Array, that contains several general informations about the measurement. Contents listed below.
APD-gain	Set APD-gain. Possible values are 150, 300, 400 and 500.
ASIC-gain	Set ASIC amplification. Possible values are 1, 16 and 32.
timeSec	Measurement time in seconds. Typically 3600, corresponding to one hour.
Thresh	Trigger-Threshold. Set to zero, when more than one trigger-channel is set.
TriggerCh	Indicates, on which channel the SADC triggered. Set to 32, when triggered on all active channels.
Stretch	Waveform-Stretch option as explained in chapter 2.5.
Shift	Waveform-Shift as explained in chapter 2.5.
FE_Threshold	Threshold set for the feature-extraction.
eventNo	Continous number of the evaluated event, used for timing considerations. If two events have the same event number, they occurred simultaneously.
APDDet	Which detector produced this trace. Values going from one to nine.
APDPos	Which position the APD had on the detector. 1 for "left" and 2 for "right".
chNo	Number of the associated SADC input-channel, going from 0 to 31. Refer to table 6.
En_sFE	Energy of the peak above/below the baseline, calculated by a simple peak-sensing algorithm. Values are in SADC-channels.
Time_sFE	Time of the peak, calculated by a simple peak-sensing algorithm, ranging from 0 to 511 in principle.
En_FE	Energy of the peak, calculated by the feature-extraction algorithm.
Time1_FE	First timing information of the peak, calculated by the feature-extraction algorithm.
Time2_FE	Second timing information of the peak, calculated by the feature-extraction algorithm.

5.2. Calibration

For the calibration, the position of the most probable value (MPV) of cosmic muons in the energy spectrum of the APDs has to be found out. To achieve this, all found energies were gathered in histograms, APD-wise. Histograms were created for the energy-values calculated by the before-mentioned peak-sensing algorithm and for the energies determined by the feature-extraction of Oliver Noll. Examples of these histograms can be seen in figure 32.
Additional to the energies, the timing results are also interesting. Distributions of the timing is shown in figure 33. In both histograms, as well as in the histograms of the other APDs, equidistant peaks can be found.
To cope with the noise signals, that apparently distort the cosmic data, a moving average filter (MAF, MA-filter) was designed. A moving average filter in general takes several values around a former data point into account and calculates new data points out of this. Thus, a new histogram is build out of the former one with e.g. the following formula:

$$y(n) = \frac{1}{L} \cdot \sum_{k=0}^{L-1} x(n-k), \tag{9}$$

whereas $y(n)$ are the data points of the new histogram, L is the filter parameter ($L-1$ values around the former data point plus itself are averaged) and $x(n)$ are the data points of the former histogram. In this form, the MA-filter accounts for the last $L-1$ values before a data point.
In figures 34 and 35, the effects of a moving average filter on a noisy trace with no signal and on a trace where noise and a cosmic are overlapping, respectively, are shown. The noise in figure 34, is dampened from a peak-to-peak value of 1200 ADC-channels (an arbitrary unit) to 900, 250 and 175 for a filter-parameter of 5, 10 and 20, respectively.
When looking at a trace, where a cosmic peak and noise are present in parallel, the effects become even more noticable. The shown peak in figure 35 is mitigated from 1200 to 1075 ADC-channels under the baseline when a moving average parameter of 20 is used, while the noise is attenuated from a peak-to-peak value of 525 to 75 ADC-channels.

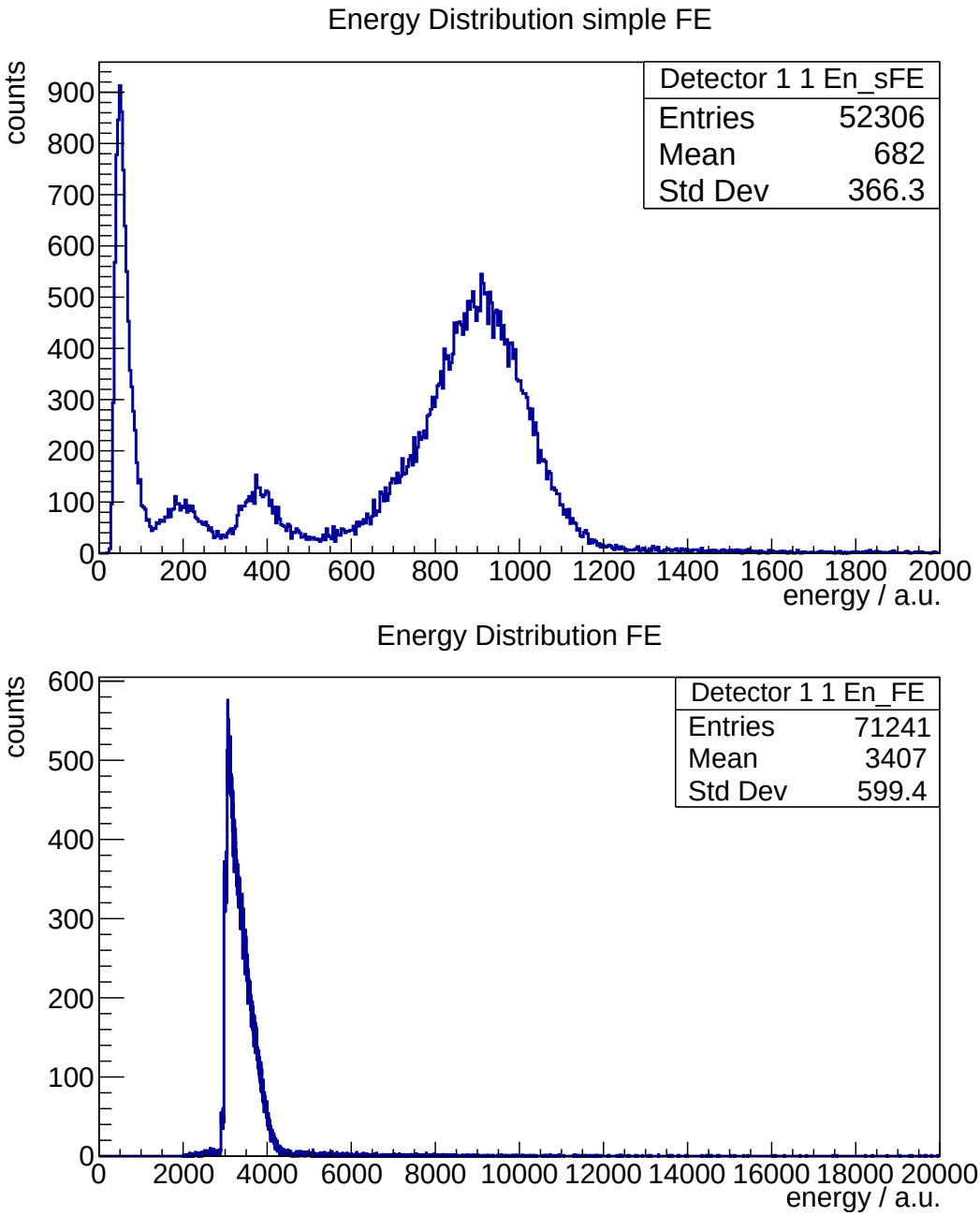

Figure 32: Energy distributions of the cosmic data for the simple peak-sensing algorithm and the feature-extraction by Oliver Noll without event filtering. Both histograms are for APD 1 on detector 1.

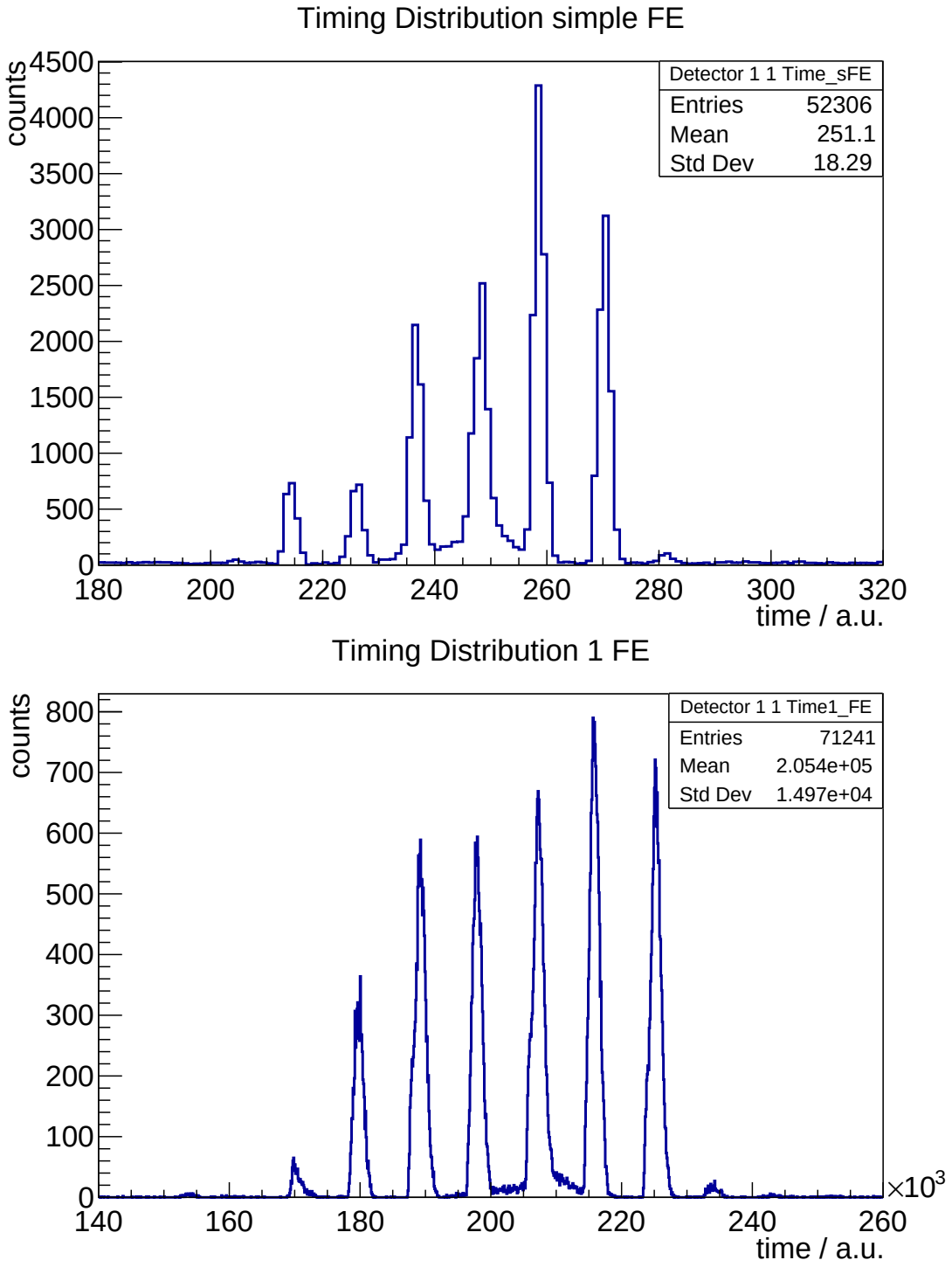

Figure 33: Timing distributions of the cosmic data for the simple peak-sensing algorithm and the feature-extraction by Oliver Noll without filtering or sorting the data. Both histograms are for APD 1 on detector 1.

5.2 Calibration

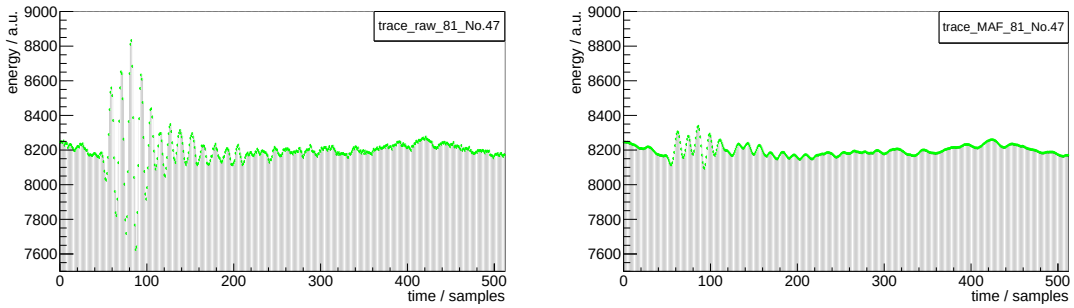

(a) No MAF

(c) MAF with $L = 10$

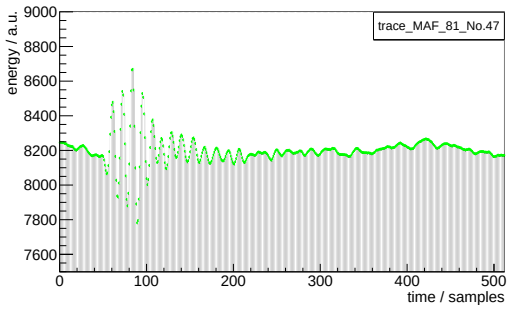

(b) MAF with $L = 5$

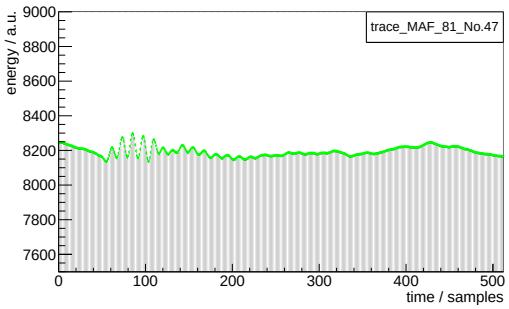

(d) MAF with $L = 20$

Figure 34: Reduction of noise through the moving average filter. The given parameter L is the amount of data points taken into account. The traces were taken with ASIC-gain 16 and APD-gain 300.

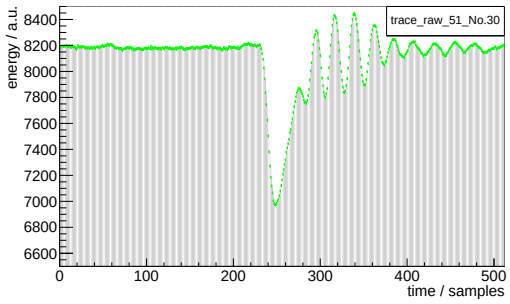

(a) No MAF

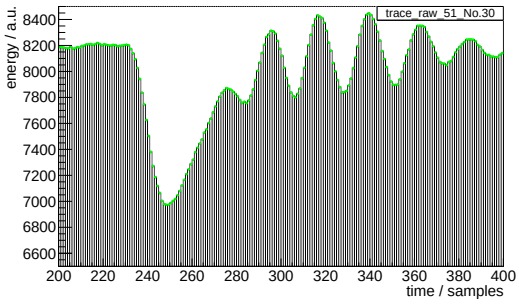

(c) No MAF, zoomed in

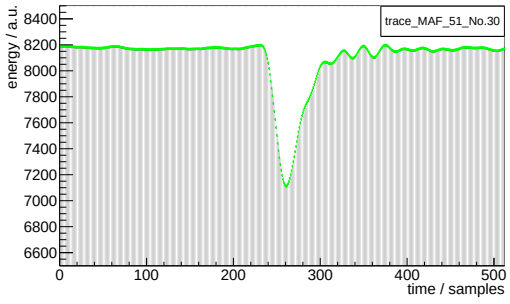

(b) MAF with $L = 20$

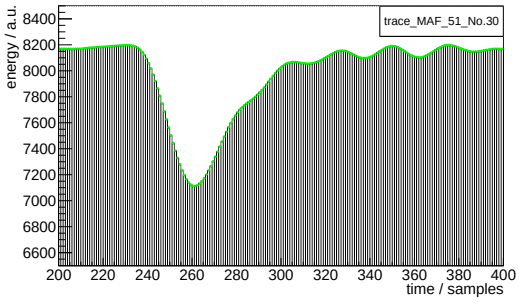

(d) MAF with $L = 20$, zoomed in

Figure 35: Reduction of noise through the moving average filter. The given parameter L is the amount of data points taken into account. The shown traces were recorded in the cosmic measurement runs.

After processing all traces with the moving average filter, the data was again plotted in histograms. An example is shown in figure 36. The pictures show the energy distribution of APD 1 on detector 1 and can therefore be compared to figure 32. When looking at the two distribution, it can be seen, that the majority of the data points is now shifted to low energies. The lower picture in figure 36 shows the same histogram with a logarithmic y-axis.
With respect to these results, an event selection was developed. As the moving average filter falsifies the cosmic peaks, the produced traces are not used directly for the calibration. Instead, the events are sorted with the results of the MAF. If the moving average filtered results are over a threshold of 400, the events are considered as true events and all other events are removed. The remaining events are again plotted in histograms. Taking a look at figure 37, a great improvement can be seen. Another look on the timing of the selected events shows an improvement as well.
From this point, only the residual data and the results of the $\overline{\text{P}}$ANDA feature extraction will be considered. The next step in the calibration is the determination of the actual most probable value of the data. Therefore, a landau fit was applied to the selected data. The fit range was first set from 2000 to 20000. Afterwards, the fit was calculated again, with a fit range from 0.75 to three times the previously designated MPV and thereafter one more time with the same fit range.
The qualities of the fits are then evaluated by their χ^2/ndf-values. These should be below 1.5 and where the quality of the fits doesn't meet this requirement, additional fit runs were executed with further restricted fit ranges. When the first χ^2/ndf does not suffice, the fit range is reduced to 0.8 to two times the MPV and when the χ^2/ndf of this fit is also above 1.5, the last fit has a range of 0.8 to 1.5 times the MPV.
The results of these fits are shown in table 10.
The uncalibrated data points can now be calibrated by a calibration factor generated by the determined most probable values and the mean energy that is deposited by a cosmic muon in a crystal with the utilised geometry. According to chapter 5.4.2.1. of [9], the MPV of deposited energy in a type 6 crystal is $MPV_6 = 27.97 \pm 0.03\,\text{MeV}$. A type 6 crystal has a length of 200 mm just as the rectangular crystals used for these measurements, but the front-face is not square and different from the backside of the crystal.

Table 10: Most probable values of the cosmic measurements and their errors, determined by a Landau fit.

Detector	APD	MPV / a.u.	ΔMPV / a.u.
1	1	3270	72
1	2	3920	42
2	1	3680	78
2	2	3500	25
3	1	4076	61
3	2	4220	45
4	1	3427	18.8
4	2	4140	40
5	1	3060	25
5	2	3440	68
6	1	4360	27
6	2	4590	43
7	1	3263	16
7	2	6160	33
8	1	4080	55
8	2	4060	113
9	1	4350	61
9	2	4350	61

According to [10], a type 6 crystal has a front-face with 2 equal sides, being $BF = 21.28\,\text{mm}$, an A-side with $AF = 21.29\,\text{mm}$ and a C-side with $CF = 21.78\,\text{mm}$. The rear-face on the other hand has also 2 equal sides and 2 different ones, with $BR = 27.22\,\text{mm}$, $AR = 26.72\,\text{mm}$ and $CR = 27.27\,\text{mm}$.
As the actual orientation of the crystal in [9] is not known and the vast majority of the detected muons coming from above the crystal, the side length of the used backward endcap-like crystal was compared with the average side length of the B-sites of a type 6 crystal:

$$MPV_{\text{BE}} = \frac{MPV_6 \cdot l_{\text{BE}}}{\frac{BF+BR}{2}}, \tag{10}$$

where $l_{\text{BE}} = 24.4\,\text{mm}$ is the side length of a backward endcap-type crystal face and MPV_{BE} is the most probable value of deposited energy in a backward endcap crystal and equals 28.14 MeV.

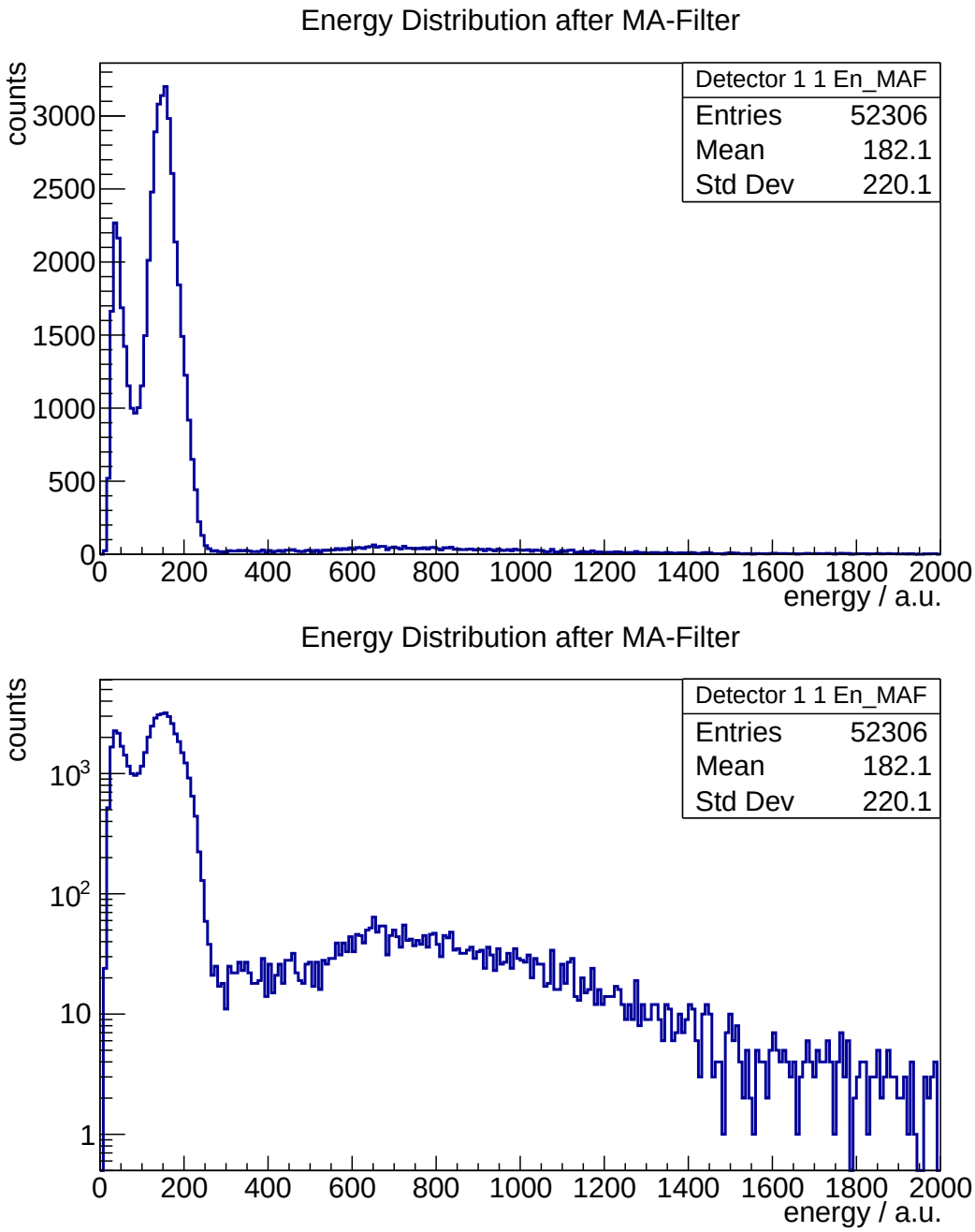

Figure 36: Energy distributions of the cosmic data after being processed by the moving average filter. The lower histogram is the same as the upper one, except that it has a logarithmic y-axis.

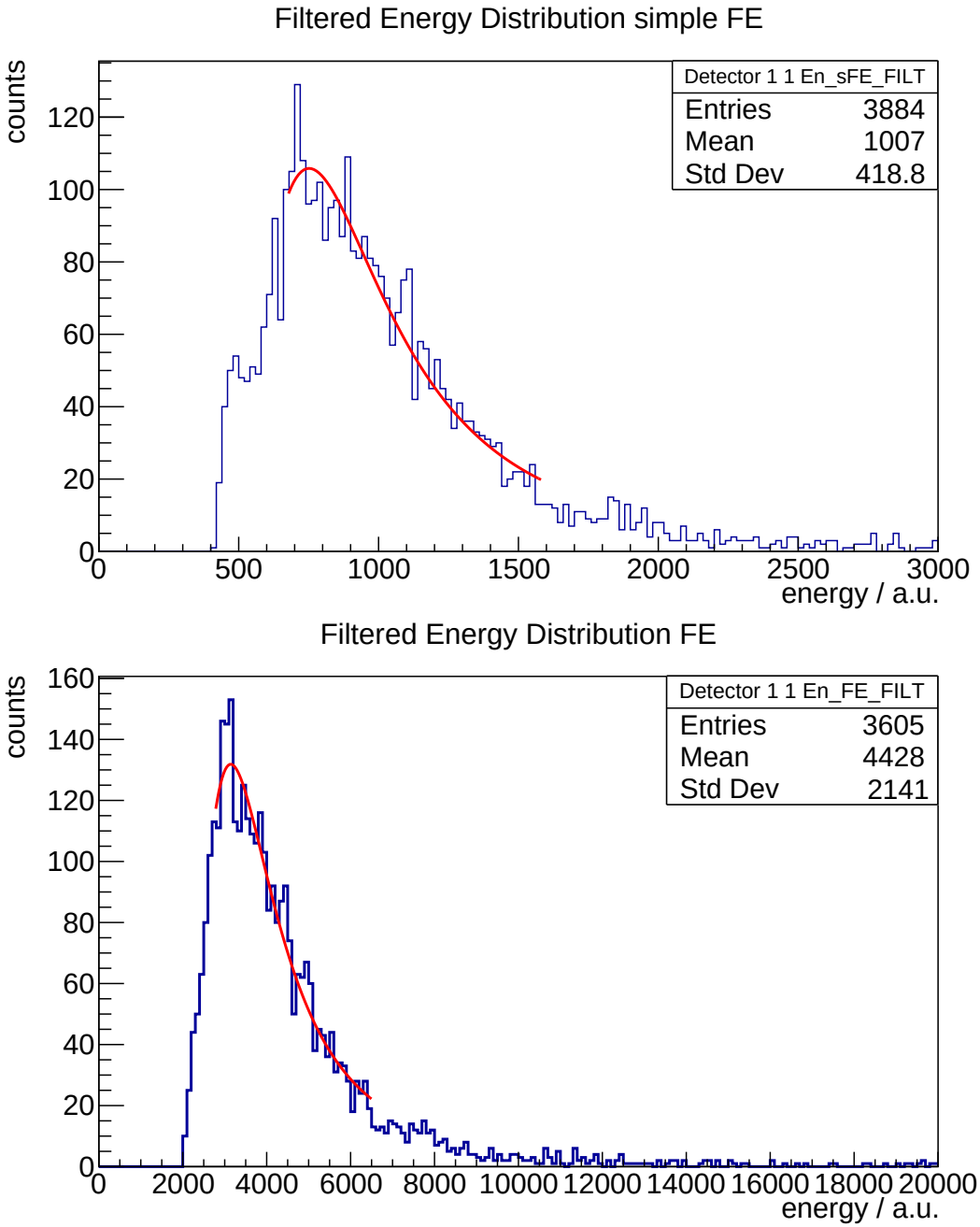

Figure 37: Energy distributions of the cosmic data for the simple peak-sensing algorithm and the feature-extraction by Oliver Noll after the event selection. Both histograms are for APD 1 on detector 1.

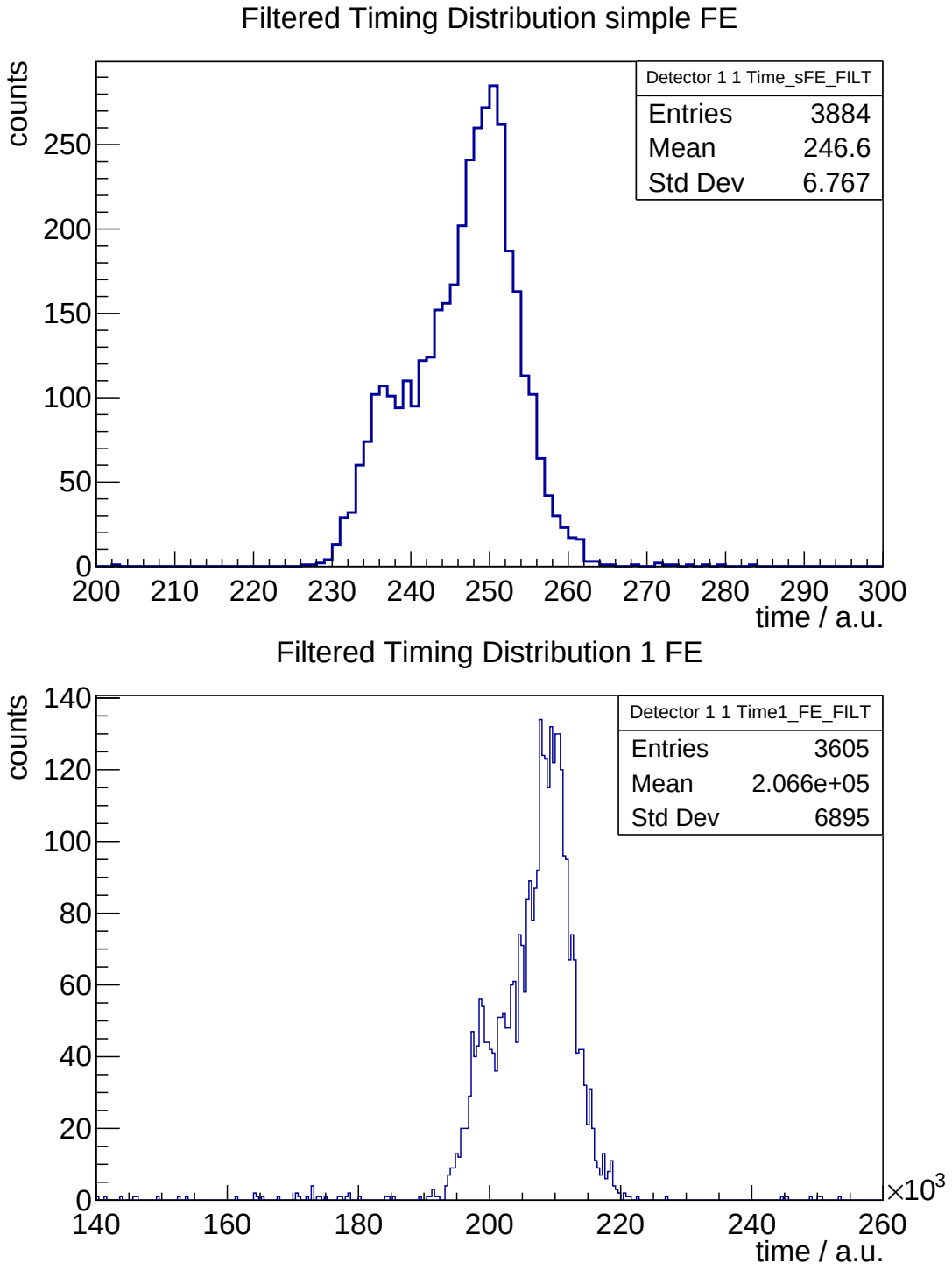

Figure 38: Time distributions of the cosmic data for the simple peak-sensing algorithm and the feature-extraction by Oliver Noll after the event selection. Both histograms are for APD 1 on detector 1.

The calibration factors for measurements with an ASIC-gain of times 16 and an APD-gain of 500 result as follows:

$$M(ch) = \frac{28.14\,\mathrm{MeV}}{MPV(ch)}, \tag{11}$$

where $M(ch)$ is the calibration factor for the channel ch and $MPV(ch)$ is the most probable value of this channel.

5.3. Calibration with light pulser

As the cosmic data was only taken for an ASIC-gain of times 16 and an APD-gain of 500, the other gain settings have to be calibrated relative to the calibrated ASIC-gain 16 APD-gain 500 data, via the light pulser measurements. Therefore, the data from the light pulser measurements were plotted channel-wise in 2D-histograms. For every channel, the energy determined by the feature-extraction is plotted against the energy of the reference detector, event-wise. This reference energy is produced by applying the moving average filter described in the previous chapter on the data from the reference detector, building a baseline from the first 200 samples of a trace and searching the lowest value under this baseline between 200 and 300 samples. A typical trace of the reference detector after application of the moving average filter is shown in figure 39.
One of the aforementioned 2D-histogram is shown in figure 40. Plotting the energy of the feature-extraction versus the reference energy event-wise, results in clouds of points with a linear behaviour.
As a linear fit shows the relation between the detector signal with the given amplification and the reference detector whose gain is not changed whatsoever, a relation between one given amplification and another one can be established, by comparing the slopes of the two energy vs. reference energy plots. Then, the calibration factor for an amplification not equal to ASIC-gain 16 and APD-gain 500 can be expressed as follows:

$$M_{ASIC,APD}(ch) = \frac{28.14\,\mathrm{MeV}}{MPV(ch)} \cdot \frac{m_{16,500}(ch)}{m_{\mathrm{ASIC,APD}}(ch)}, \tag{12}$$

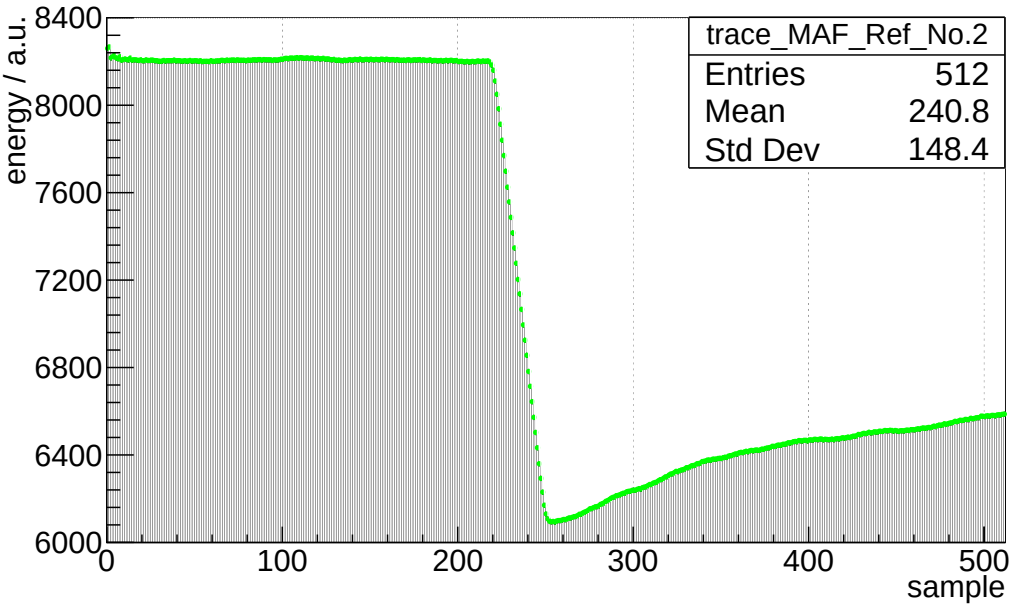

Figure 39: Typical trace of the reference detector after being processed by the moving average filter. The energy of this event is determined by averaging all samples between 0 and 200 to get a baseline and then calculating the distance to the lowest sample between 200 and 300. The trace was taken in the light pulser measurement run with ASIC-gain 16 and APD-gain 500.

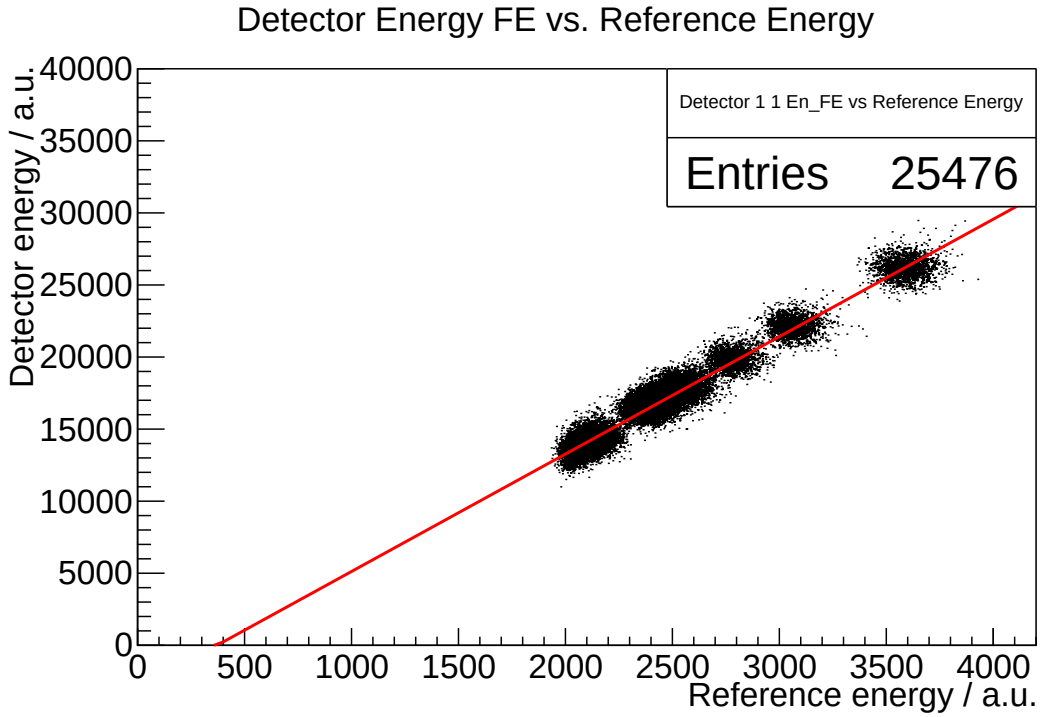

Figure 40: 2D-Histogram of the detector energy vs. the reference energy for APD 1 on detector 1 and the ASIC-gain 16 and APD-gain 500 run. The resulting point cloud is approximated with a linear fit.

whereas $M_{\mathrm{ASIC,APD}}(ch)$ is the calibration factor for channel ch and a given ASIC-gain of $ASIC$, as well as an APD-gain of APD, $m_{\mathrm{ASIC,APD}}(ch)$ is the slope of the linear fit between the energy of the detector with ASIC-gain $ASIC$ and APD-gain APD and $m_{16,500}(ch)$ is the same slope for an ASIC-gain of 16 and an APD-gain of 500, i.e. with the same settings that were used for the cosmic measurements. The determined slopes are listed in table 11.

Table 11: Determined slopes of the relations between detector energies and reference energies. These are all results for an ASIC-gain of 16.

Detector	APD	150	300	400	500
1	1	2.382	4.643	6.300	8.147
1	2	2.462	4.829	5.903	8.259
2	1	1.813	3.362	4.496	5.867
2	2	1.743	3.288	3.954	5.403
3	1	0.896	1.924	2.241	3.202
3	2	0.887	1.900	2.219	3.146
4	1	1.097	2.286	2.606	3.400
4	2	1.142	2.343	2.784	3.940
5	1	3.522	7.216	9.722	12.87
5	2	3.595	7.228	9.620	12.88
6	1	1.212	2.435	3.061	4.118
6	2	1.400	2.640	3.132	4.178
7	1	1.708	3.484	4.588	6.296
7	2	1.935	4.167	5.921	8.647
8	1	2.295	4.500	5.766	7.860
8	2	2.259	4.451	5.734	7.870
9	1	3.664	6.970	9.952	10.81
9	2	3.883	8.452	11.89	14.66

5.4. Timecuts

After the calibration of the data, the actual beam data was analysed. For a better event selection, a smaller timecut was chosen for the central detector. Events are only accepted if the time signal of the central detector is inside a sharp timing range. The basis for this consideration gives the image in figure 41.

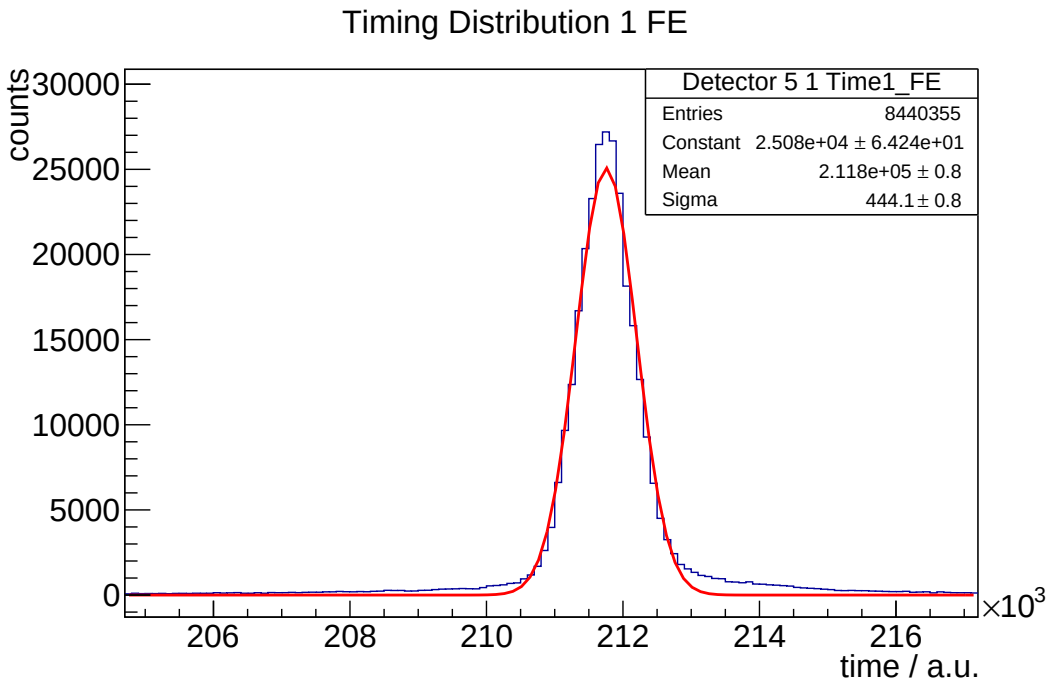

Figure 41: Timing distribution of the central detector for an ASIC-gain of 16 and APD-gain of 500, before applying timecuts. The data is fitted with a Gaussian function.

As can be seen in the figure, the timing of the central detector displays a mostly Gaussian behaviour. The mean being at 211800 with a standard deviation of 440. The chosen timing-range is 211000 to 212500 a.u. being roughly 2σ around the mean. The effect of this central time-filter can be seen in figure 42, where the coincidence of one of the central detector APDs with the 101 MeV Tagger is shown, once without the filter and once with the before mentioned central time-filter.
Tagger coincidence means, that the corresponding tagger did fire at the same time as the detector measured a signal and therefore the energy of the photon inducing the measured signal is known. In addition to the time filter on the central detector, the individual detectors were also filtered according to their timing, relative to the

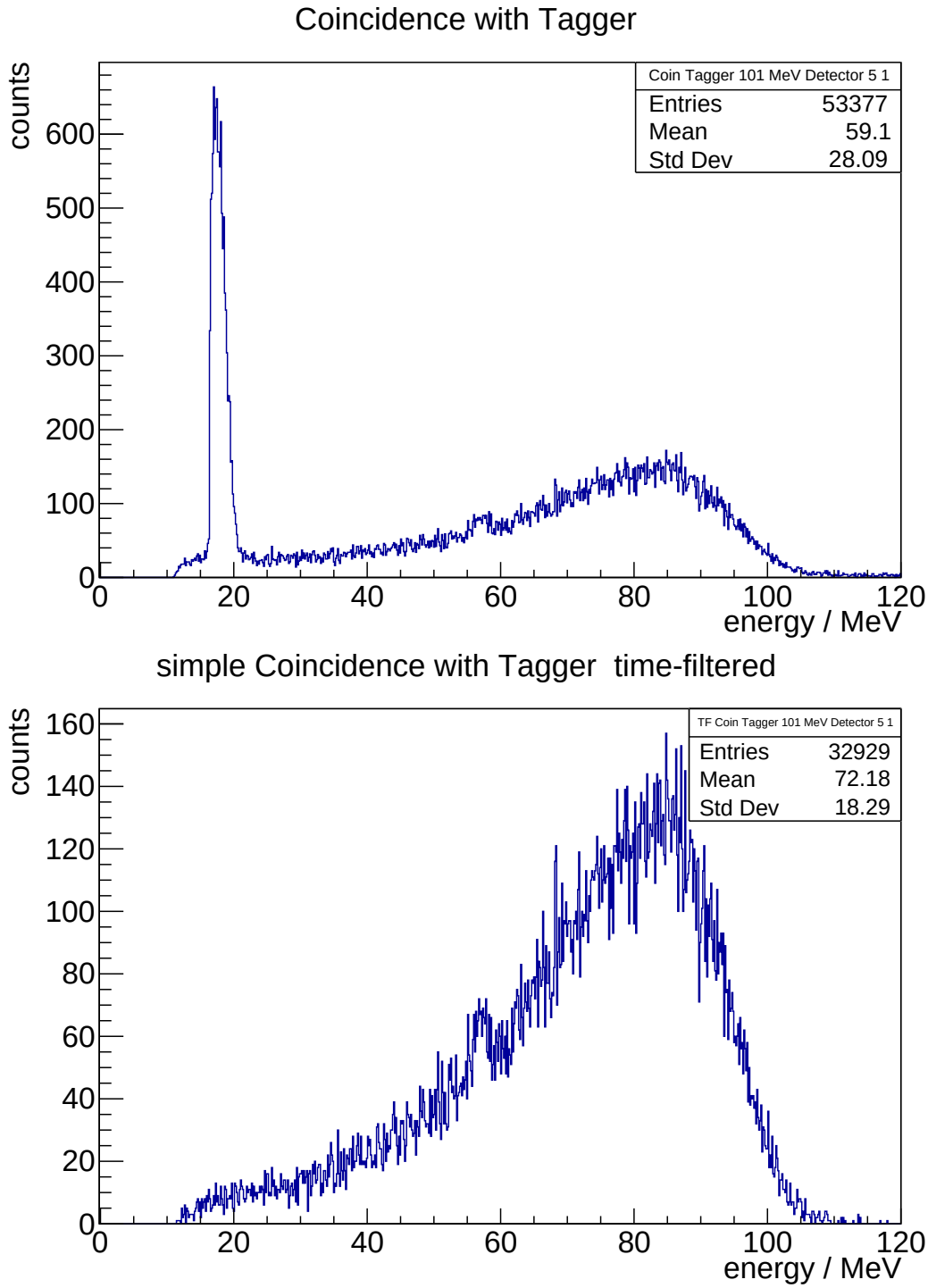

Figure 42: Comparison of the Tagger coincidence for the central detector with and without a central time-filter. The shown data belongs to the ASIC-gain 16 and APD-gain 500 beam run.

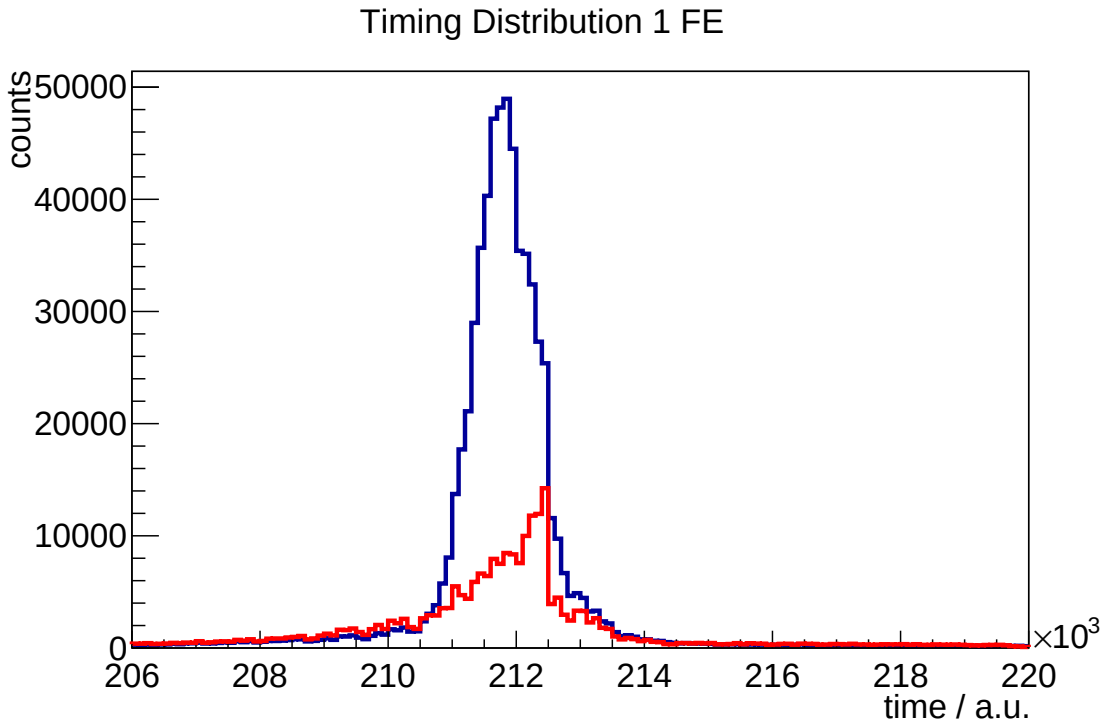

Figure 43: Comparison of central detector timing with the timing distribution of a non-central detector. The blue line represents an APD of the central detector, whereas the red line represents the APD 1 on detector 1. The shown data belongs to the ASIC-gain 16 and APD-gain 500 beam run.

central detector. In figure 43, a comparison of the timing distributions of a central APD and a non-central APD is shown.

The effect of different time-filters on the individual APDs was investigated. The utilised time-filters are working in relation to a central APD, meaning that a signal of an APD would only be allowed, if the timing of the signal was inside a given time-window around the signal of the central detector with the same event number. The data was filtered with a window of 2000 a.u. to both sides around the central signal or with a window of 5000 a.u. to lower values and 2000 a.u. to higher values. A comparison of the effects of this individual time-filter is shown in figures 44, 45 and 46.

According to the shown results, an individual time-filter window of 5000 a.u. to the left and 2000 a.u. to the right was chosen. Starting from this point, the energies as well as the timing of the two APDs belonging to a detector, were each averaged to get one energy and one time value for each detector per event.

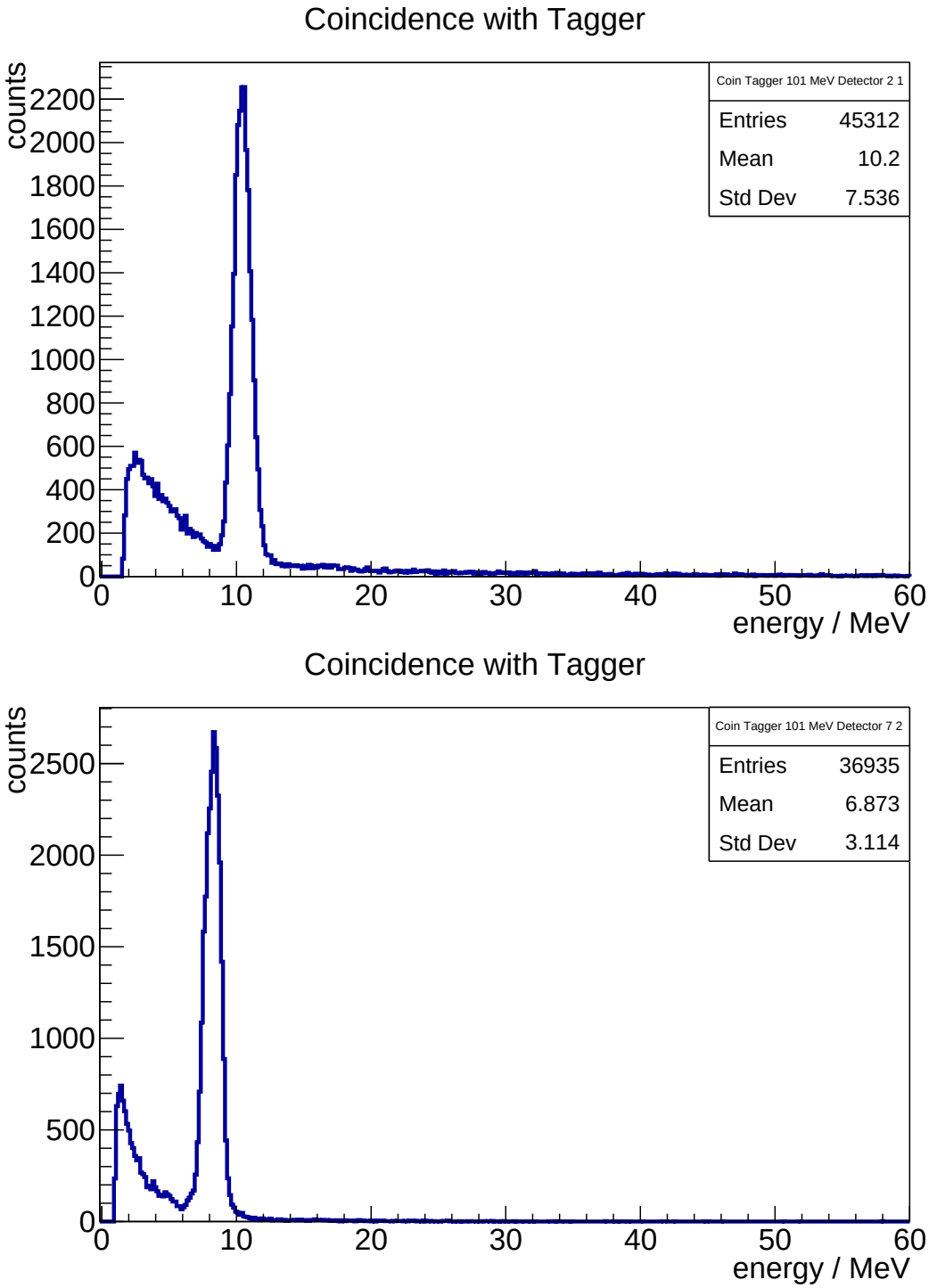

Figure 44: Energy distribution of two non-central APDs without the individual time-filter. The shown data belongs to the ASIC-gain 16 and APD-gain 500 beam run.

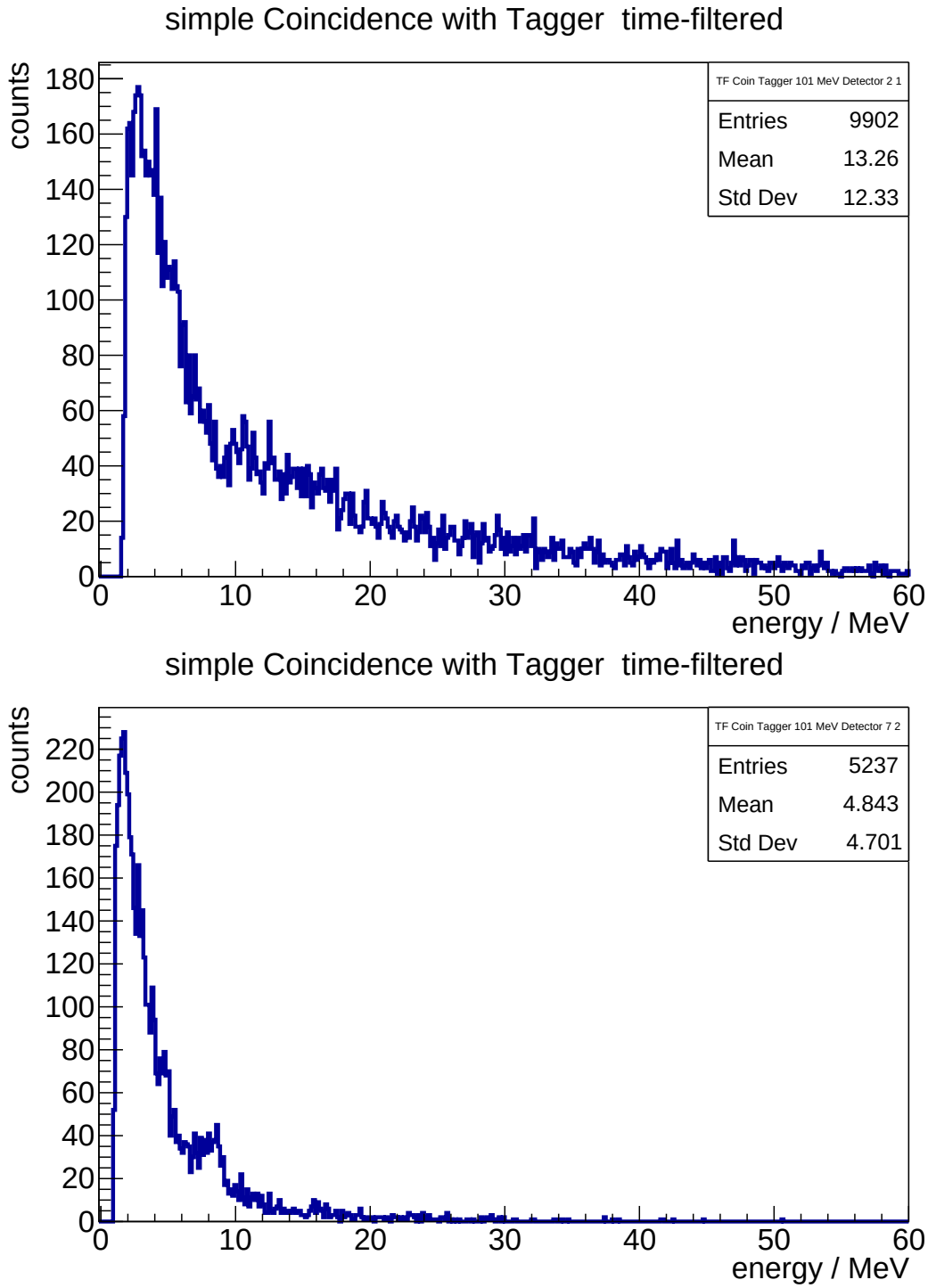

Figure 45: Energy distribution of two non-central APDs with an individual time-filter of 2000 a.u. to both sides. The shown data belongs to the ASIC-gain 16 and APD-gain 500 beam run.

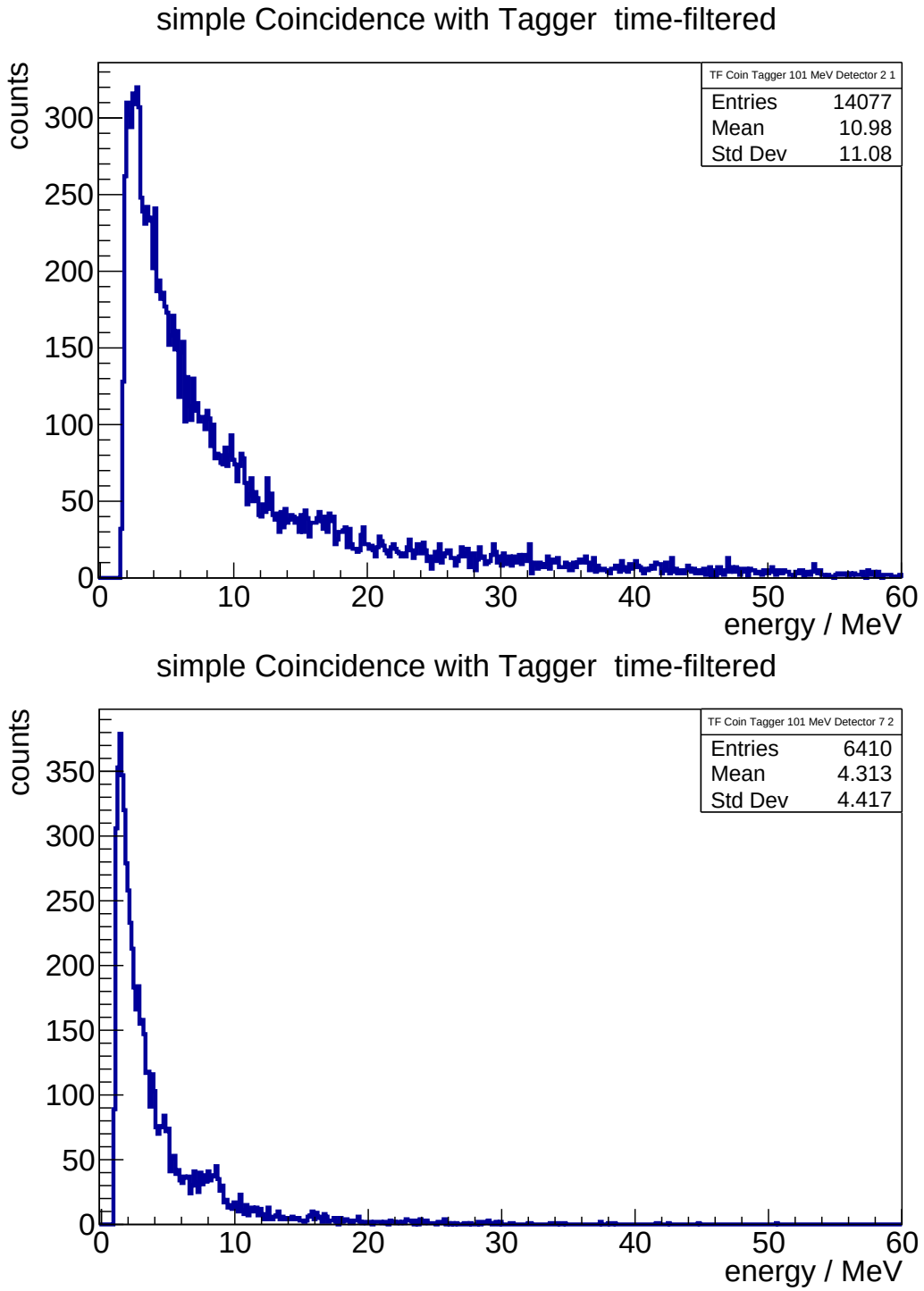

Figure 46: Energy distribution of two non-central APDs with an individual time-filter of 5000 a.u. to the left and 2000 a.u. to the right. The shown data belongs to the ASIC-gain 16 and APD-gain 500 beam run.

5.5. Beam position

The position of the beam was verified by comparing the energy distribution of the detectors with each other. Although quite a bit of effort was made to ensure that the beam hits the matrix right in its centre, the true position can only be verified via the data. In figure 47, the overall energy distributions of all detectors are shown for ASIC-gain 16 and APD-gain 500. The histograms are plotted with a logarithmic y-axis and the detectors are arranged in the same way, that they were in the matrix. If the beam was not perfectly central, we would see more counts in a detector according to the beam misdirection.

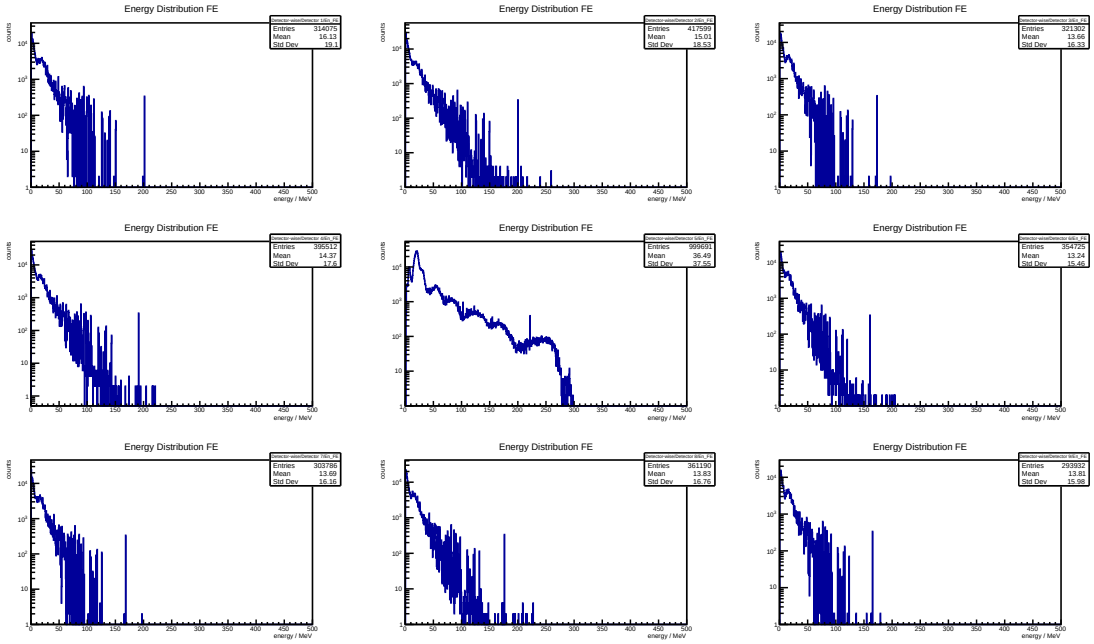

Figure 47: Overall energy distribution of all detectors for ASIC-gain 16 and APD-gain 500, with a logarithmic y-axis. The detectors are arranged like their actual position in the matrix.

5.6. Lineshapes

For the sake of noise filtering, an additional threshold was used for the summation of the deposited energy in the matrix, which was initially set to 0.5 MeV. The effect of different thresholds will be discussed later on.
In figure 48, the lineshapes for the 41 MeV tagger is shown. The total sum is shown in green, while the energy distribution of the central detector is shown in blue and the yellow line shows the total sum of non-central detectors, the outer ring, so to say. Naturally, the addition of the central and outer ring events should match the sum. The most crucial information that should be drawn from these total sums, is the mean energy value of the distribution μ, as well as the width of the distribution σ. With these two parameters, the energy resolution, being the width divided by the mean value $\frac{\sigma}{\mu}$, can be derived.
The total sum is fitted by a so-called "Novosibirsk" function, whose form is shown in the following:

$$f(x) = A \cdot \exp(-g(x)) \tag{13}$$

$$g(x) = \begin{cases} 0.5 \cdot \left(\frac{x-B}{C}\right)^2, & \text{if } |D| < 10^{-7} \\ 0.5 \cdot \left(\frac{\log\left(h(x)\right)}{D}\right)^2 + D^2, & \text{if } |D| \geq 10^{-7} \ \wedge \ h(x) > 10^{-7} \\ 15, & \text{else} \end{cases} \tag{14}$$

$$h(x) = 1 + D \cdot \frac{(x-B)}{C \cdot \frac{sinh(D \cdot \log(4))}{D \cdot \log(4)}}, \tag{15}$$

whereas A is the amplitude and the first fitting parameter, B is the second fitting parameter, the "peak" value comparable with the mean of a gaussian function, C is the third fitting parameter "width" equivalent to a Gaussian width and D is the last fitting parameter "tail" taking into account the low-energy asymmetry of the Novosibirsk function [11]. After several test fits, the parameter D was set to -0.2, as this seems to be the optimal value for the majorities of the results. In figures 48, 49 and 50, the lineshapes for the 41 MeV, 101 MeV and 201 MeV taggers are shown, respectively.

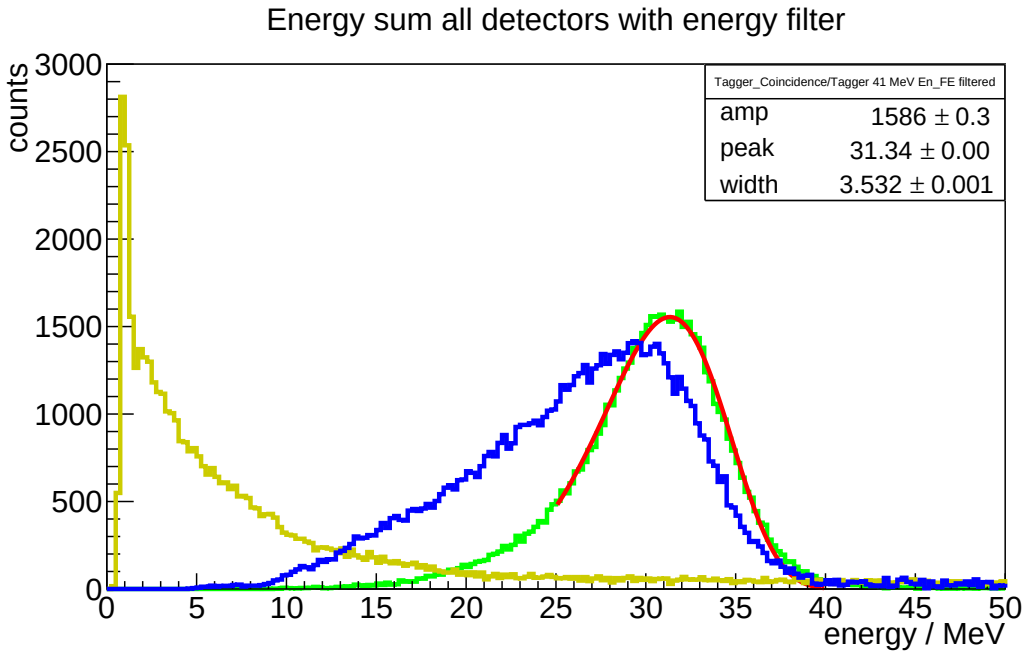

Figure 48: Lineshapes of the 41 MeV photon energy events. The yellow line represents the sum of the outer ring, the blue one the central detector and the green one is the total deposited energy. The Novosibirsk fit of the total sum is also shown, together with the fit parameters A (amp), B (peak) and C (width) in this order. The shown data belongs to the ASIC-gain 16 and APD-gain 500 beam run.

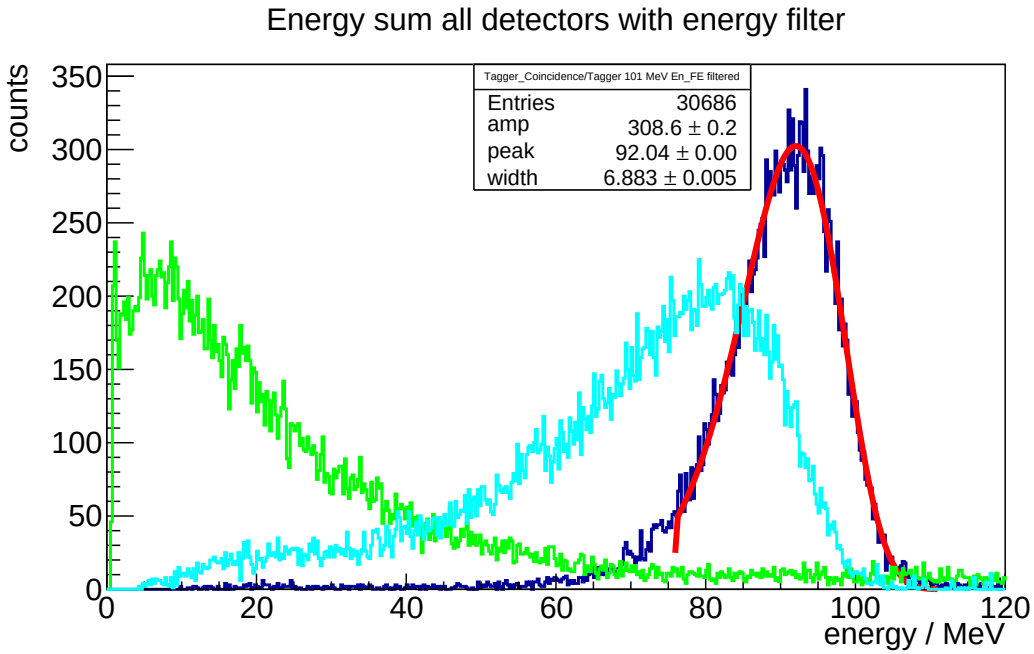

Figure 49: Lineshapes of the 101 MeV photon energy events. The green line represents the sum of the outer ring, the pale blue one the central detector and the dark blue one is the total deposited energy. The Novosibirsk fit of the total sum is also shown, together with the fit parameters A (amp), B (peak) and C (width) in this order. The shown data belongs to the ASIC-gain 16 and APD-gain 500 beam run.

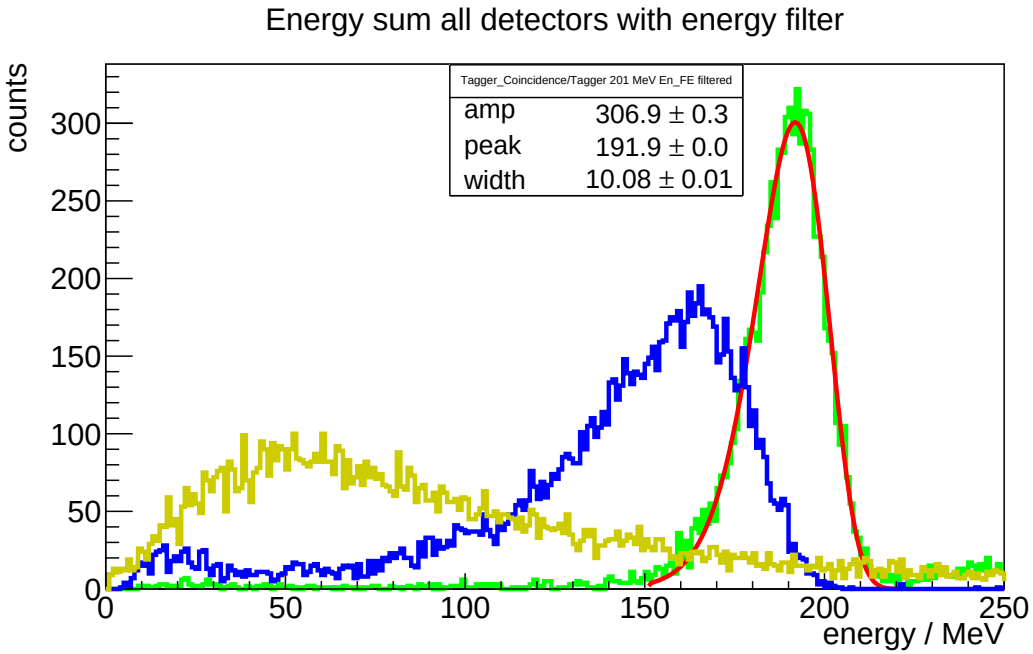

Figure 50: Lineshapes of the 201 MeV photon energy events. The yellow line represents the sum of the outer ring, the blue one the central detector and the green one is the total deposited energy. The Novosibirsk fit of the total sum is also shown, together with the fit parameters A (amp), B (peak) and C (width) in this order. The shown data belongs to the ASIC-gain 16 and APD-gain 500 beam run.

In figure 51, the energy sum for each tagger except for the two highest ones are shown in one diagram. The lineshape for 401 MeV and 427 MeV are not shown, due to the very low, collected statistics for these energies. As the shape of the highest shown lineshapes, the ones for 300 and 343 MeV, are difficult to distinguish from the underground noise, the same image is again shown with a logarithmic y-axis in figure 52.

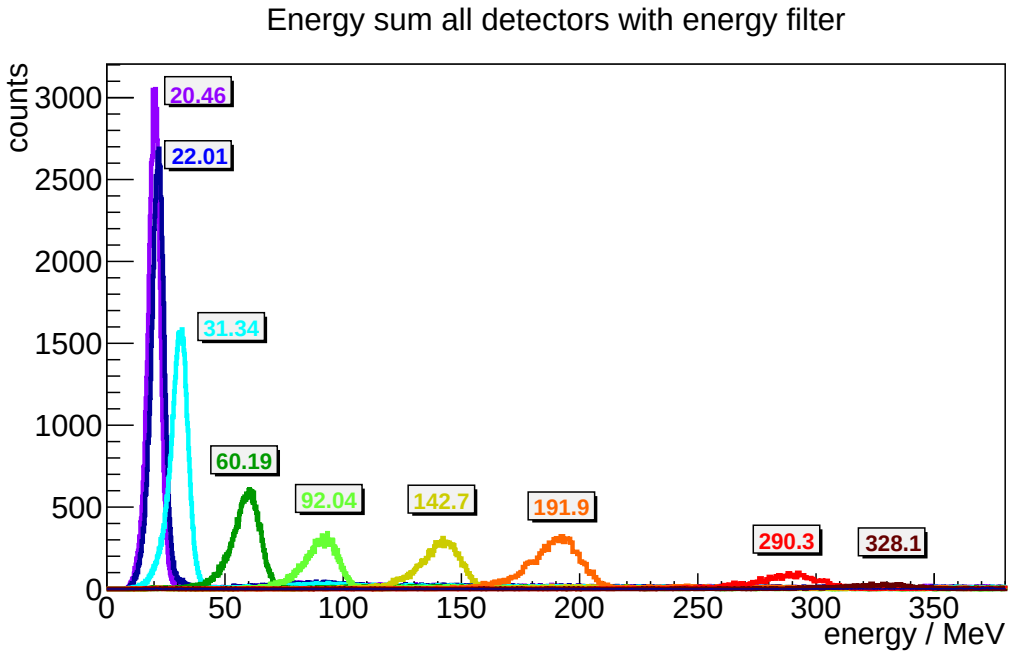

Figure 51: Histogram of the different analysed lineshapes shown together. The numbers beside the peaks are their mean value (parameter B of the fit). The peaks belong to the following taggers: purple: 29 MeV, dark blue: 31 MeV, pale blue: 41 MeV, dark green: 70 MeV, pale green: 101 MeV, yellow: 151 MeV, orange: 201 MeV, red: 300 MeV, dark red: 343 MeV. The shown data belongs to the ASIC-gain 16 and APD-gain 500 beam run.

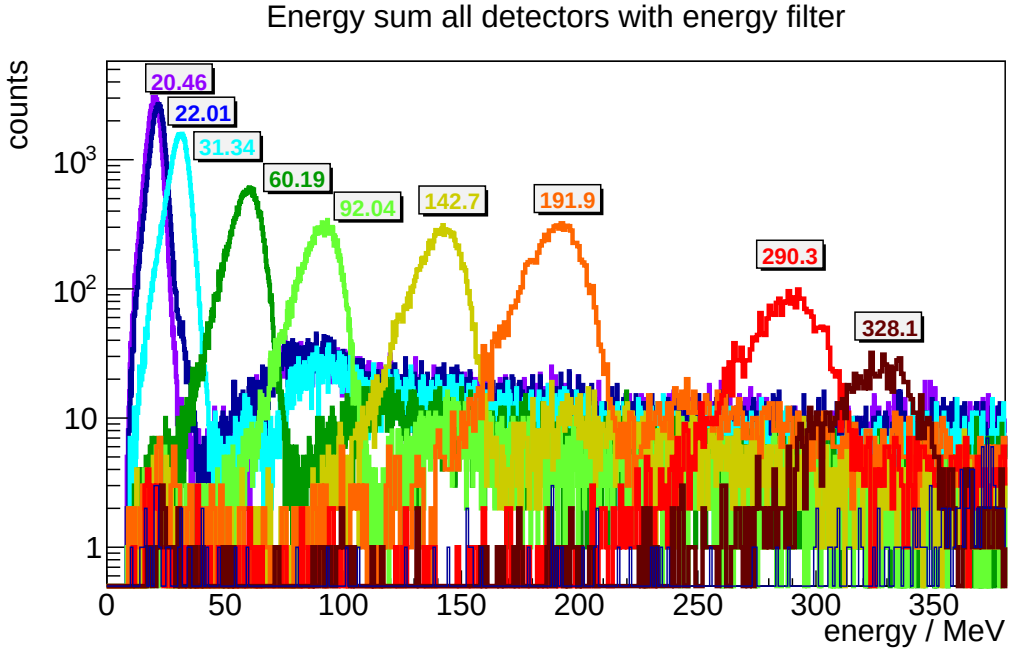

Figure 52: Histogram of the different lineshapes shown together, with a logarithmic y-axis. The colours are coded the same way as in the above picture. The shown data belongs to the ASIC-gain 16 and APD-gain 500 beam run.

5.7. Energy resolution

As mentioned before, the energy resolution σ/E is one of the most crucial parameters to be optimised. The energy resolution for a given lineshape is calculated by dividing parameter C, the width, by B, the peak. By plotting the energy resolution of a lineshape against the deposited energy, a response function can be derived.
The response function can be fitted with a function like the following:

$$\frac{\sigma}{E} = \sqrt{\left(\frac{p_0}{\sqrt{E}}\right)^2 + \left(\frac{p_1}{E}\right)^2 + p_2^2}, \tag{16}$$

where p_0 is a statistical noise term, p_1 is a electronic noise term and p_2 is a constant fitting parameter.
This shows the dependence of the energy resolution from the incoming particle energy and must be lowered to a minimum to get optimal results in later applications. In the previous chapters, a hit-detection threshold for the $\overline{\text{P}}$ANDA feature extraction and an individual energy threshold (for the total sum) were discussed. The first one was set to 50 ADC-channels to this point in the analysis, which translates into a calibrated energy of 0.31 MeV to 0.47 MeV, depending on the calibration and is applied to every APD, when the feature-extraction is processing the data. As the central detector has significantly higher peaks than the outer detectors, it was set to double the normal threshold, translating to an energy of roughly 0.9 MeV.
The individual energy threshold (from now on called single crystal threshold) in turn was now analysed regarding its effect on the energy resolution. In figure 53, a comparison of different thresholds is shown for the ASIC-gain 16 and APD-gain 500 data set.
For several energies, a threshold scan was performed, meaning that the energy resolution for one tagger energy was plotted against the applied single crystal threshold. This is shown in figure 54.
The response function for a threshold of 0.5 MeV can be seen in figure 55. It should be noted, that the highest two energies are omitted, because of their significantly lower statistics, that cause large errors in the energy resolution, as indicated in figure 53.

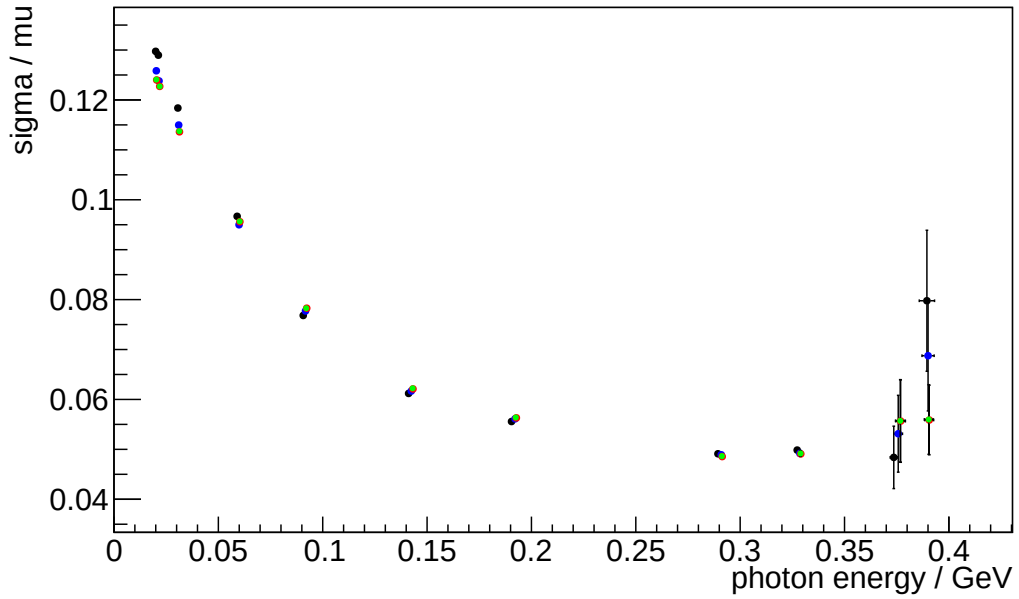

Figure 53: Comparison of different single crystal thresholds for the response function of ASIC-gain 16 and APD-gain 500. The black, blue, red and green dots show the response function for a single crystal threshold of 3 MeV, 2 MeV, 1 MeV and 0.5 MeV, respectively.

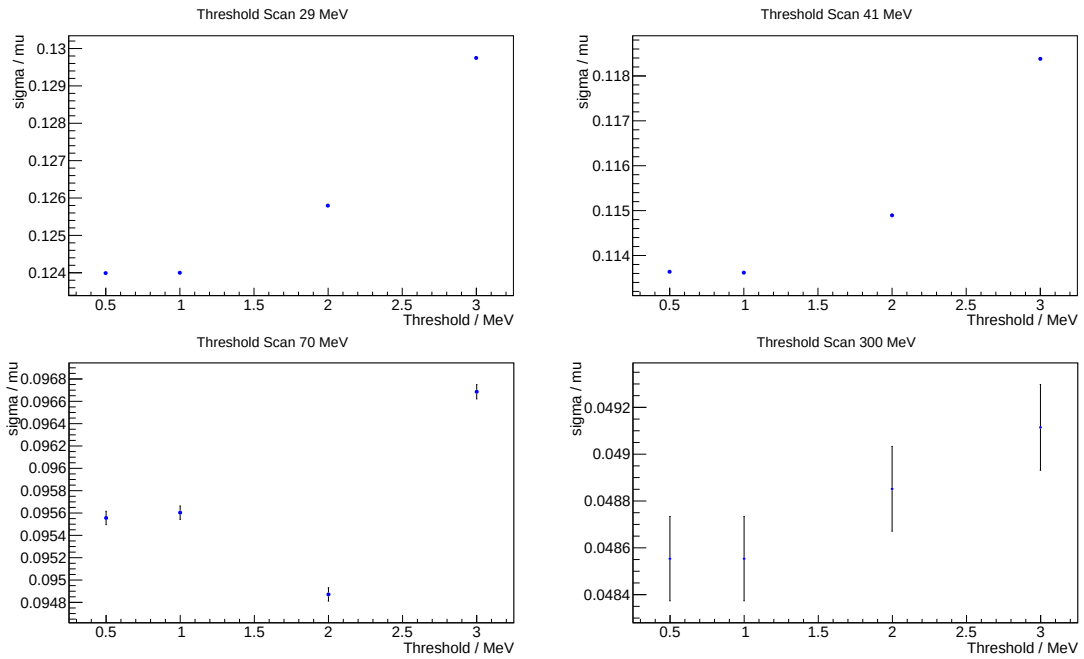

Figure 54: Threshold scans for different tagger energies.

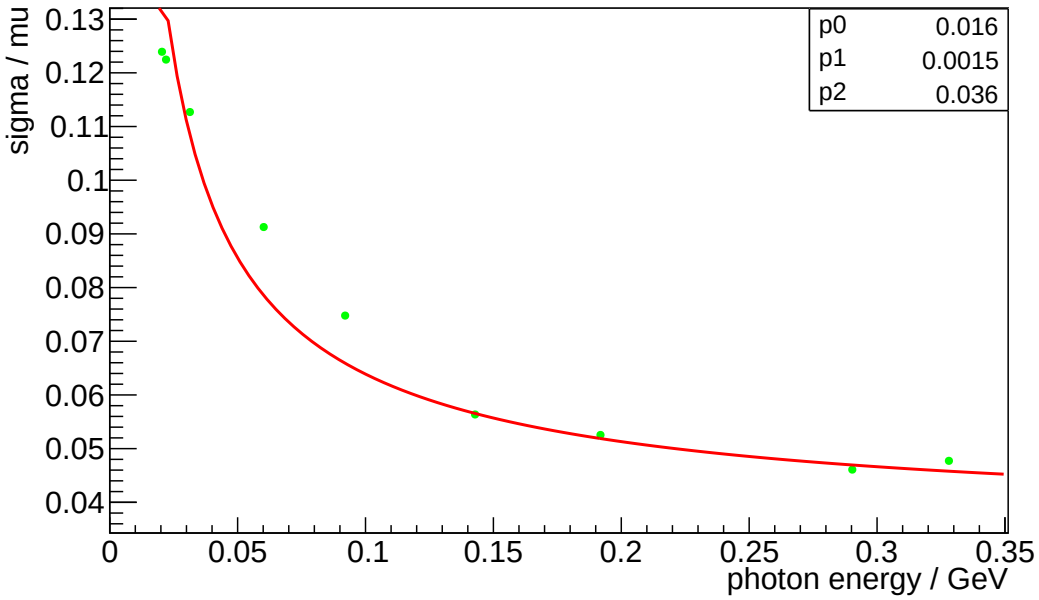

Figure 55: Fit of the ASIC-gain, 16 APD-gain 500 response function. The fit parameters are shown in the upper right corner.

The ASIC-gain 16 and APD-gain 150 response function was also compared for different thresholds and the comparison is shown in figure 56.
In figure 57, a fit of the 1 MeV single crystal threshold is shown, with the corresponding fit parameters.

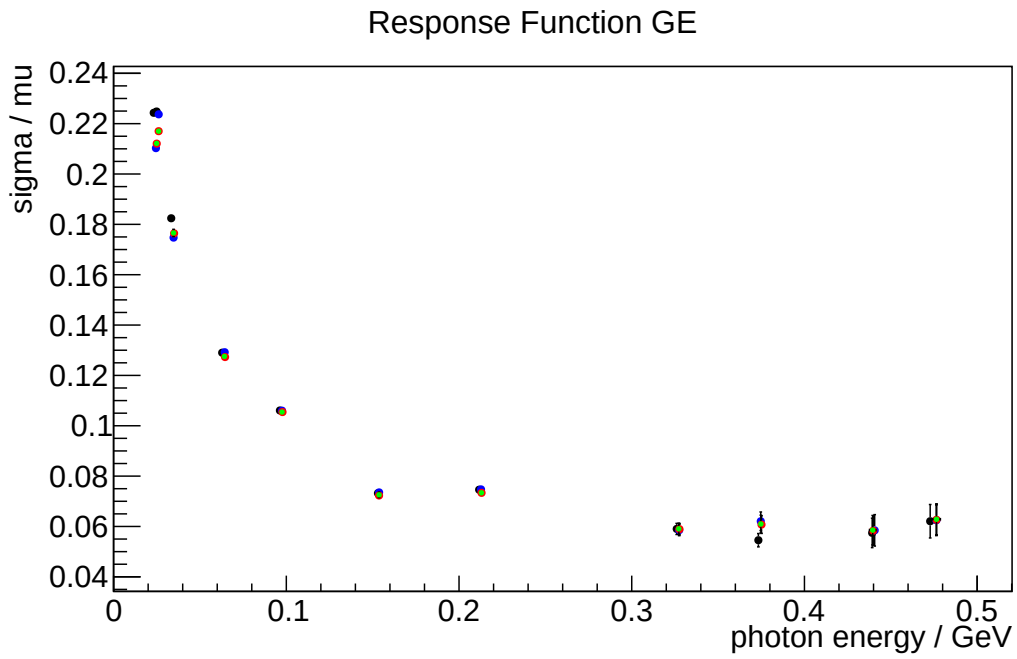

Figure 56: Comparison of different single crystal thresholds for the response function of ASIC-gain 16 and APD-gain 150. The black, blue, red and green dots show the response function for a single crystal threshold of 3 MeV, 2 MeV, 1 MeV and 0.5 MeV, respectively.

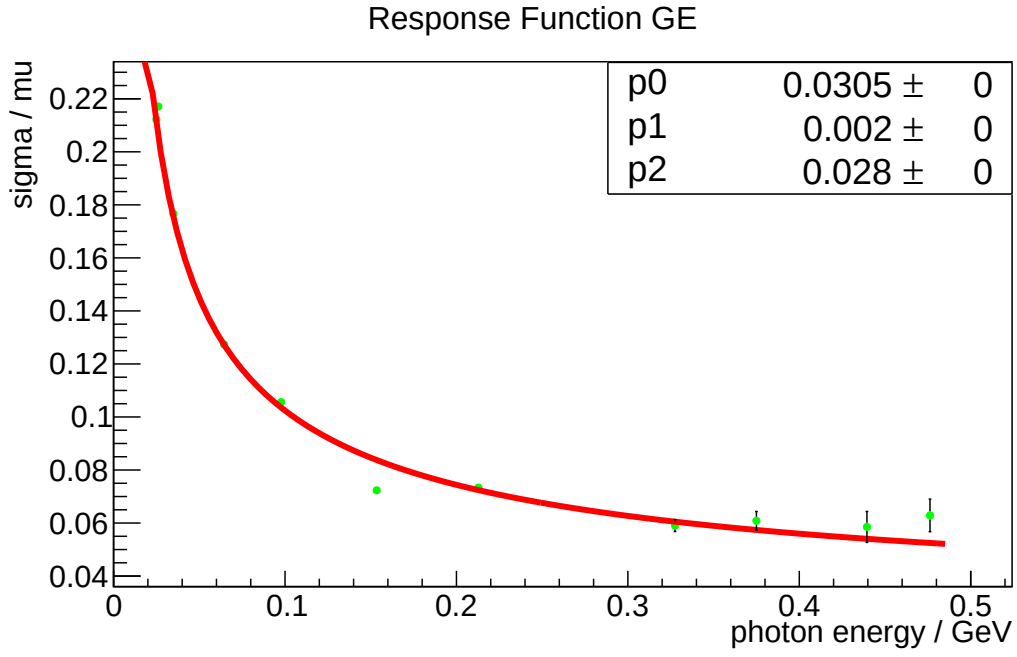

Figure 57: Fit of the ASIC-gain, 16 APD-gain 150 response function. The fit parameters are shown in the upper right corner.

6. Discussion

The first histograms of run 1.4 displayed in figure 27 are showing the characteristic shape of the expected signal. Discrete energy levels can be seen due to the coincidence with selected channels of the tagger. This fact is even more recognisable, when the data is shown with a logarithmic z-scale.
The timing of the signals can also be derived from the histograms. The peak is at roughly 257 samples and the whole signal is between 240 and 300 samples. To prevent any actual traces being lost, but filter the vast majority of the random coincidences, the time window for the first event-selection was set at 220 to 320 samples. The improvement gained by this event-selection can be seen, when comparing the histograms with figure 28.
Looking at the raw traces for the 1.4 beam measurement, signal heights of 4000 ADC-channels below the baseline and more can be found for the central detector. The lower right picture in turn is taken from a non-central detector and has a signal height of roughly 200 ADC-channels over the baseline. The lower right picture in figure 30 shows a trace of the same detector, where characteristic noise is apparent. The signal height of this noise is roughly 600 ADC-channels below the baseline. The characteristic structure appears coincident in all detectors. Therefore, one could assume, that this is caused by electromagnetic interference from an external source. Although the actual source of the pick-up noise could not be found out, the frequency with which the pick-up noise appears is relatively low compared to the event rate, which means that the effect of the noise could be reduced, when the beam intensity is raised.
When the frequency of the measured signal is in the same order as the noise or even lower, as it is the case for the cosmic measurements, additional actions have to be taken. In figure 31, a trace with a cosmic muon belonging to the cosmic measurement run is shown, where the pick-up noise was observed, too. The cosmic muon peak has a height of 1200 ADC-channels below the baseline, while the pick-up noise has a maximum amplitude of 525 ADC-channels below the baseline. This translates to a signal-to-noise ratio of 43.75 % within the raw data. Due to the pick-up noise occurring with a higher frequency than the cosmic rate, events containing those have to be filtered out by selecting only those events, where cosmic muons were

detected. The necessity for such a selection method becomes more apparent, when looking at the energy distributions in figure 32. Firstly, the distributions do not have the typical Landau-shape, expected for cosmic muons and on the other hand, the number of events is roughly one order of magnitude higher than expected.
At sea level the particle flux of muons is roughly $144\,/\mathrm{m}^2{\cdot}\mathrm{s}$ [12]. For a rectangular crystal with the given surface of 200 mm times 24.4 mm and therefore a surface area of $0.005\,\mathrm{m}^2$, we expect 0.72 cosmic muons per second. As the overall measurement time was four hours (14400 seconds), we therefore expect roughly 10000 events.
Taking a look at the time distribution in figure 33, we see equidistant peaks, with a distance of 11 to 12 samples in the upper picture analysed by the peak-sensing algorithm, which is double the period of the pick-up noise. This is again a strong indicator, that the pick-up noise is overlaying the cosmic muon peaks.
The effect of the moving average filter, that was designed to cope with the noise is shown in figure 34 and 35. Of particular interest is here the change in signal-to-noise ratio obtained by using the filter, when applied to the trace, where a cosmic muon is present coincident with the pick-up noise. After applying the filter, the height of the muon peak is 1075 ADC-channels below the baseline, while the pick-up noise was diminished to roughly 40 ADC-channels amplitude. This translates to a signal-to-noise ratio of 3.7 %, which is a huge improvement to the previous 43.75 %.
As the moving average filter dampens the signal and changes its form, the modified traces should not be used for extraction of energy or time of signals, but as event selection. The scope of this thesis is to invest the impact of an increased APD-gain, while using the $\overline{\mathrm{P}}$ANDA feature extraction.
After applying the event-selection via the moving average filter, the energy and time distributions match the expectations. The number of events is roughly in the expected range and the energy distributions are similar to a Landau-distribution.
Unfortunately, APD 1 on detector 9 did not record any cosmic muons at all during the cosmic measurement run. As the MPVs of two APDs belonging to the same detector are rather similar, the MPV for the other APD on detector 9 was assumed for both APDs.
Concerning the results for the slopes of the linearity measurements (result in table 11), one would assume, that the ratio between two slopes of the same detector for different gains matches the gain ratios, i.e. the slopes for the gain 300 measurements should be twice as steep as the slopes for the respective gain 150 measurements.

But the constant term of the linear fit was not fixed to zero, as this would have resulted in large errors for the fits. A constant of zero was expected, as there should be no signal on a detector in the matrix, when there is no signal on the reference detector. The reason for this deviation could be explained by the DAC-values of the APFEL. If the offset of each single-ended signal part of the differential signal is not perfectly aligned to the dynamic range of the following buffer, a part of the signal could be cutted. is since a strict optimisation of these could not be guaranteed.
Coming back to the data of run 1.4, the impact of the time filter for the individual detectors in relation to the timing of the central detector signals was compared in figures 44, 45 and 46. A large noise-induced peak can be seen in the unfiltered histogram between 8 and 12 MeV, depending on the APD. This peak vanishes nearly completely, when a time cut of 2000 a.u. on both sides is applied.
In figure 43, a larger tail on the left side of the non-central time distribution can be recognised. Because of this asymmetry, the time cut on the left side was shifted to 5000 a.u., resulting in significantly more statistics, without a significant rise of the noise peak. Hence, the latter was chosen as time filter for further analysis.
Despite special considerations being made, it was possible that the beam did not hit the detector matrix exactly in its centre. To verify that this is not the case, the total energy distributions of the detectors for one beam run (1.4, with ASIC-gain 16 and APD-gain 500) were arranged in the same fashion as the corresponding detectors were positioned in the matrix. Figure 47 shows this arrangement and the histograms adjacent to the central detector show no significant differences. Due to this fact, one can assume that the beam did hit the matrix directly in its centre.
Further analysis of the data resulted in the construction of the lineshapes, showing the total deposited energy. These are generated by adding up all measured energies event-wise. Shown are the lineshapes of the events caused by the taggers with 41 MeV, 101 MeV and 201 MeV in figures 48, 49 and 50, respectively.
Additional to the total energy deposition, the energy deposition in the central detector as well as in the outer ring (all detectors, except the central one) are shown. The higher the energy, the broader will the electromagnetic shower caused by the incoming photon will be, causing higher relative signals in the outer detectors.

The lineshape of the relatively low tagger energy of 41 MeV is displayed here with its outer ring as well, to show that even at this low energy the outer ring does contribute significantly to the total deposited energy. Typically, between 70 and 90 % of the total deposited energy can be found in the central detector.
When looking at the histogram of all analysed lineshapes together in figure 51, it is recognisable, that the reconstructed energies are shifted by 10 MeV to the respective, expected energy, no matter if its a high or a low energy. This effect can not be explained with the calibration, because the differences between actual mean value and expected energy should depend on the energy. As this is not the case, a shift of the chosen tagger channels could be assumed
Another detail, that can be seen, is that the number of counts in the peaks decreases with increasing energy. Although this is expected, because of the lower probability for higher energetic photons to be generated in the target, there is no drop from 151 MeV to 201 MeV. This incident is due to the binning of the histograms being halved from 201 MeV onwards, so that the histograms are more comparable.
Subsequently, a comparison of different single crystal thresholds regarding their effect on the energy resolution was performed. In figure 53, it can be seen that a significantly better energy resolution can be achieved in the low energy regime below 70 MeV when using a single crystal threshold of 0.5 MeV instead of 2 or 3 MeV. This is additionally supported by the threshold scans shown in figure 54, where the threshold of 0.5 MeV results in the best energy resolutions for low energies and for high energies above 200 MeV as well.
Typically, the energy resolution has an optimum value at 30 % of the peak-to-peak noise and gets worse, when the threshold differs from that. An example for that behaviour is shown in figure 58. The optimum threshold for the PROTO60 $\overline{\text{P}}$ANDA prototype was determined. The fact, that the single crystal threshold in the actual measurements here can be put down to 0.5 MeV and maybe even further, indicates an improved signal-to-noise ratio.
In comparison, the optimum threshold using an APD-gain of 150 and the APFELs was found at 2.7 MeV [2]. The cause of the large discrepancy of the optimum threshold for PROTO60 and PROTO120, is due to the utilised preamplifiers. The PROTO60 used a Basel-type preamplifier, whilst the PROTO120, as well as this thesis, used the APFELs as preamplifier. The results of the investigations of [2] did also show, that the APFEL are one of the main sources for noise.

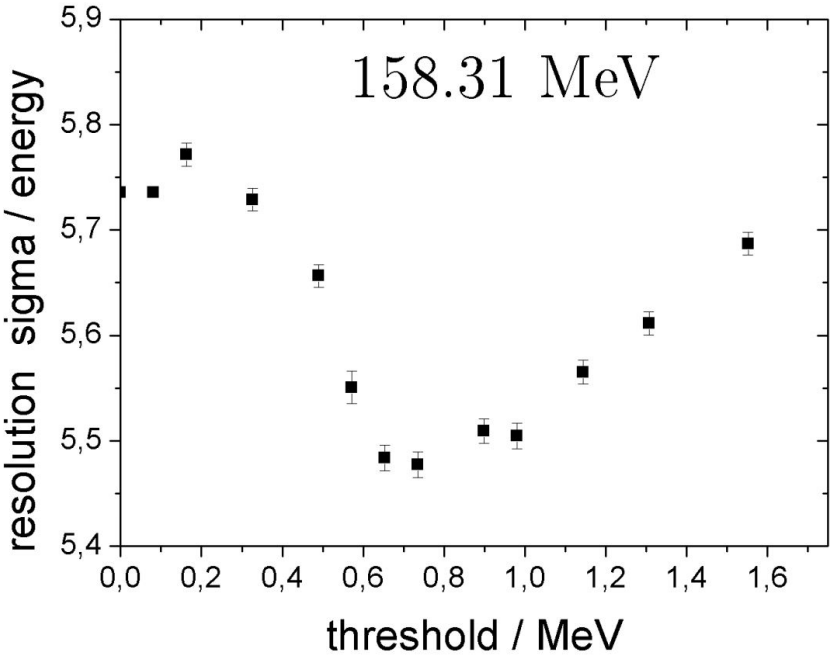

Figure 58: Threshold scan for low energy photons in the PROTO60. The optimal single crystal threshold is between 0.6 and 1.1 MeV. Courtesy by [9].

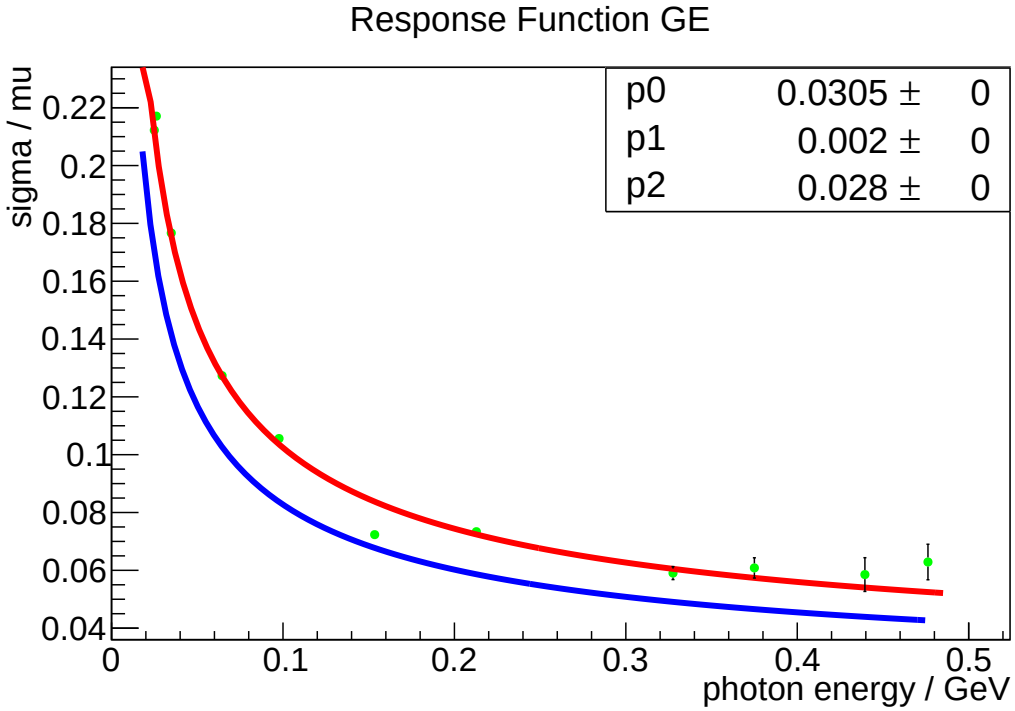

Figure 59: Comparison of the 1.1 beam data with the PROTO120 results. The green dots show the energy resolutions for a single crystal threshold of 1 MeV, the red line is the fit for the dataset and the blue line is the resulting optimal response function of the PROTO120.

Another point that underlines the importance of a low single crystal threshold is the reconstruction efficiency. In figure 60, the impact of the single crystal threshold on the reconstruction loss of π^0-mesons is shown.
Using a threshold of 2.7 MeV, the lowest possible photonenergy can be used for the reconstruction of pions with a momentum of up to 1.5 GeV/c. With the threshold of 0.5 MeV, the lowest possible photonenergy can be taken into account over the full shown momentum range and well beyond that.

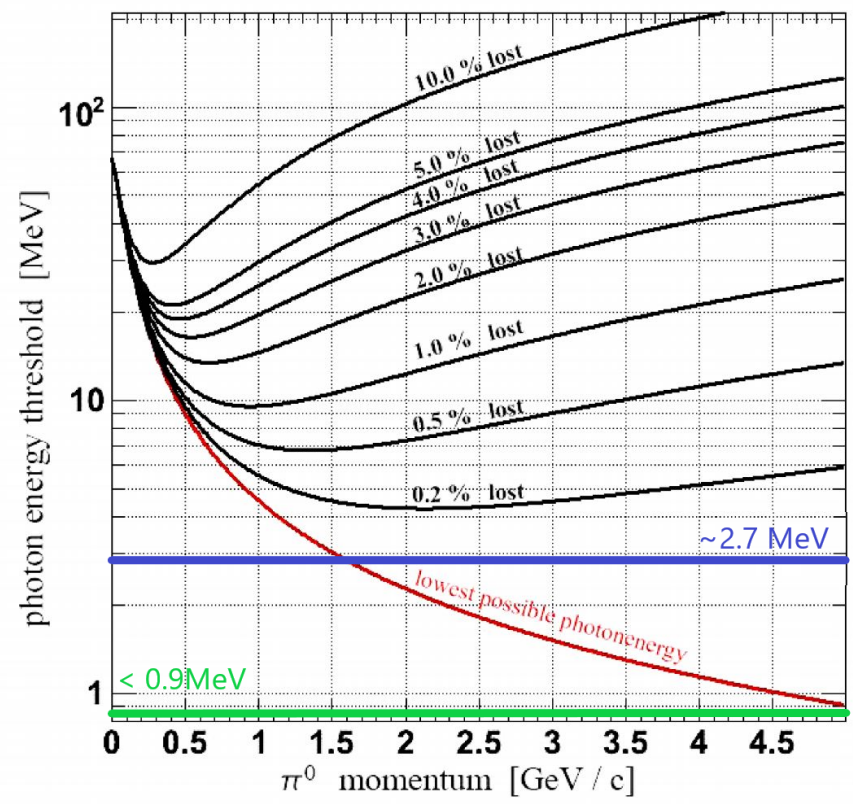

Figure 60: Dependence of the π^0 reconstruction loss on the single crystal threshold and the π^0-momentum. Picture taken from [11] and modified.

As shown before, the fit function assumed for the response function has three terms:

$$\frac{\sigma}{E} = \sqrt{\left(\frac{p_0}{\sqrt{E}}\right)^2 + \left(\frac{p_1}{E}\right)^2 + p_2^2}.$$

The first one being p_0, which is a statistical term caused by the photon-counting process and the second one p_1, being the electronic term caused by the electronic noise, while the third term p_2 is a constant term. The values found for the PROTO120 subarray are $p_0 = 2.46\,\%$, $p_1 = 0.16\,\%$ and $p_2 = 2.32\,\%$ [10]. The parameters are higher for the response function of run 1.1, as expected.
In figure 61, the response function of run 1.1 was compared to run 1.4, meaning an APD-gain of 150 to an APD-gain of 500. It can be seen, that the resolution has greatly improved with the use of a higher gain and this not only in the low-energy regime below roughly 100 MeV, but also in the higher energy regimes from 300 MeV upwards, although a real comparison is difficult there, because of the low statistics. For the lowest energies of about 30 MeV, the resolution was improved from 21.5 % to 12.4 %.
Of a high interest is also the comparison of the 1.4 run with the PROTO120 data, which is shown in figure 62. On the one hand, the form and height of the response functions can be compared, like it is shown in figure 62. It can be seen in this image, that the energy resolutions for the 1.4 run, are constantly below the PROTO120 values. For an energy of 30 MeV, the PROTO120 would have an energy resolution of 15.6 %, whereas the 1.4 energy resolution is 12.4 %, which is an improvement of 3.2 %. When comparing high energies like the 290 MeV, the PROTO120 would have an energy resolution of 5.1 %, while run 1.4 has 4.85 %, which is also an improvement, although not as much as in the low-energy regime.
The comparison of fit parameters and, therefore, the statistic and electronic part of the energy resolution is also interesting. In table 12, the fit parameters of runs 1.1 and 1.4 are shown together with the PROTO120 results.
Especially the electronic term p_1 of run 1.4 is expected to be especially low, compared to the PROTO120 result. That is because the higher APD-gain accounts for larger input signals into the APFEL, and with a higher input signal, the signal-to-noise ratio on the front-end output should be significantly better.

Table 12: Comparison of the fit parameters of the response function for the PROTO120, run 1.1 and run 1.4.

Parameter	PROTO120 / %	run 1.1 / %	run 1.4 / %
p_0	2.46	3.05	1.6
p_1	0.16	0.2	0.15
p_2	2.32	2.8	3.6

The statistical parameter was expected to be similar or even worse in the beamtime runs, because of the light yield of the utilised rectangular crystals being lower than the light yield of the type 2 crystals used in the PROTO120. The type two crystals of the PROTO120 have a light yield of approx. 25 $\frac{\text{phe}^-}{\text{MeV}}$, while the rectangular backward endcap crystals have a light yield of 17 $\frac{\text{phe}^-}{\text{MeV}}$, according to [13]. As the light yield does describe the number of photons created per energy unit, it does contribute to the statistical parameter by its root. Expected was therefore a statistical term of:

$$p_{0,\text{BT}} = p_{0,\text{P120}} \cdot \frac{\sqrt{25\frac{\text{phe}^-}{\text{MeV}}}}{\sqrt{17\frac{\text{phe}^-}{\text{MeV}}}} = 2.98\,\%, \tag{17}$$

which is in agreement with the run 1.1 statistical term. Surprisingly, this is not the case for the 1.4 run data. The parameter accounting for the photon statistic is in turn rather low compared to the PROTO120 data, which could be a hint, that the higher APD-gain does also improve the photo-detection by lowering the signal-to-noise ratio of the APD itself.
These deviations off the expectations could also mean, that further improvement of the fit-parameters have to be done, to fit the data better and perhaps lower the electronic term by a larger bit. When taking a closer look on the course of the lower energy data in run 1.4 (100 MeV downwards), the energy resolution seem to have an almost linear behaviour, where the applied fit could perhaps be improved.
Another important specification of the detector matrix is its dynamic range. The barrel part of the EMC in $\overline{\text{P}}$ANDA will extend from 22 ° up to 140 ° in respect to the interaction part. This means that with a maximum of 15 GeV/c beam momentum incoming into the experiment, the barrel will have to detect energies up to 7.3 GeV.

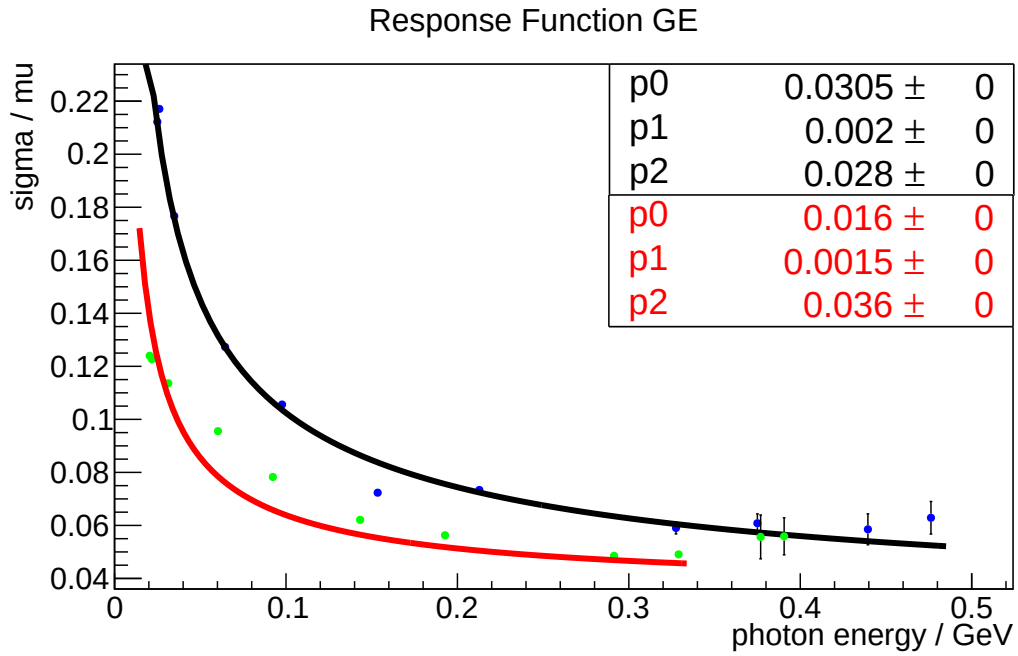

Figure 61: Response functions for APD-gain 150 and APD-gain 500, both with ASIC-gain of 16. The green dots represent the APD-gain 500 dataset together with the corresponding fit shown in red, while the blue dots represent the APD-gain 150 dataset, with the black line as fit.

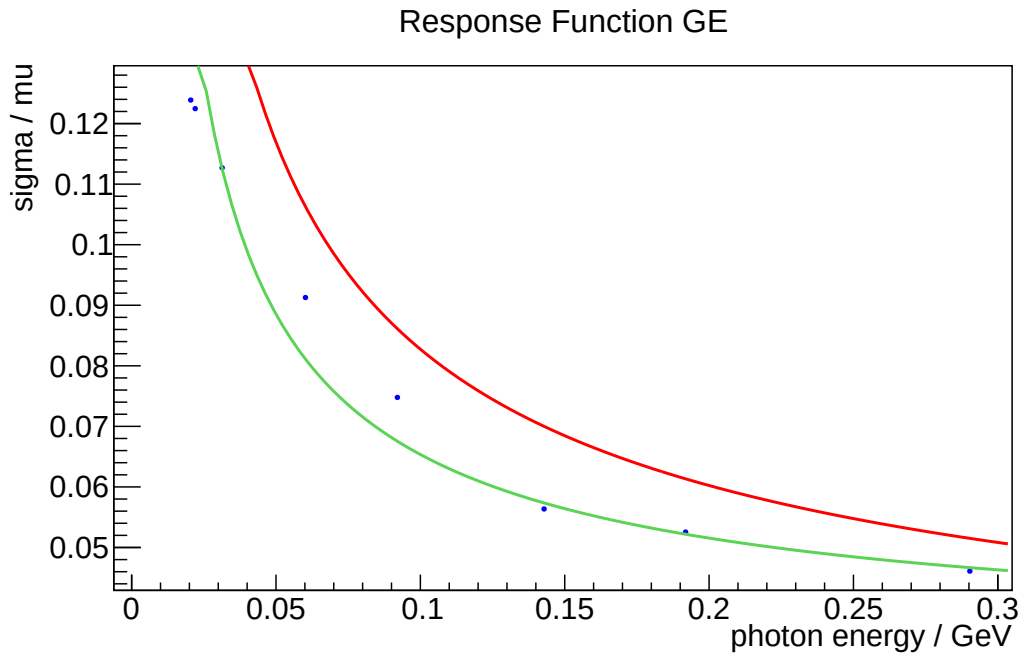

Figure 62: Comparison of the 1.4 beam data with the PROTO120 results. The blue dots show the energy resolutions for a single crystal threshold of 0.5 MeV, the green line is the fit for the dataset and the red line is the resulting optimal response function of the PROTO120.

When discussing the possible improvements on the energy resolution by using a higher gain of 500, one should also consider, what the highest detectable energy is. To determine this, another look into the cosmic data for the calibration is taken. In table 10, the most probable values of the cosmic measurements with an APD-gain of 500 and ASIC-gain of 16 was shown. The given values are results of the feature extraction of Oliver Noll and can hardly be taken directly for the dynamic range considerations. However, the most probable values of the simple peak-sensing algorithms were also determined and these are in units of ADC-channels. It is known, that the maximum amplitude of the linear response region is at about 7500 ADC-channels. The most probable values mentioned are between 750 and 1150 ADC-channels. Hence, the maximum dynamic range can be calculated to:

$$E_{\max} = \frac{7500\,\text{ADC-channel}}{1150\,\text{ADC-channel}} \cdot 28.14\,\text{MeV} \approx 184\,\text{MeV}, \tag{18}$$

and 280 MeV, respectively. It has to be considered that these values for the maximum dynamic range, are only valid for the ASIC-gain 16 branch and an APD-gain of 500. The dynamic range becomes significantly larger (roughly by a factor of 12), when using the low-gain branch of the ASICs.
In figure 63, simulations of the angular dependence of the photon energy distribution for two different incoming particle momenta in the later $\overline{\text{P}}$ANDA-experiment is shown.

When assuming the lower dynamic range from the previous calculations and a factor of 12, the dynamic range for the low-gain branch goes up to 2.2 GeV. Therefore, the increased APD-gain of 500 could be used up to 40 ° for the lower momentum and up to 50 ° for the higher momentum (which is also the maximum possible beam momentum), without losing any information.
When determining the optimal gain and therefore bias voltage of the APDs, one has to consider the breakthrough voltage of the APDs. The applied bias voltages are about 8 to 9 V below the breakthrough voltage and the used power supplies (which are the same, that are planned for $\overline{\text{P}}$ANDA) have a voltage stability better than ± 0.1 V.
In the future $\overline{\text{P}}$ANDA-experiment, a higher gain would provide several advantages. On the one hand, a higher gain could compensate for light yield losses through

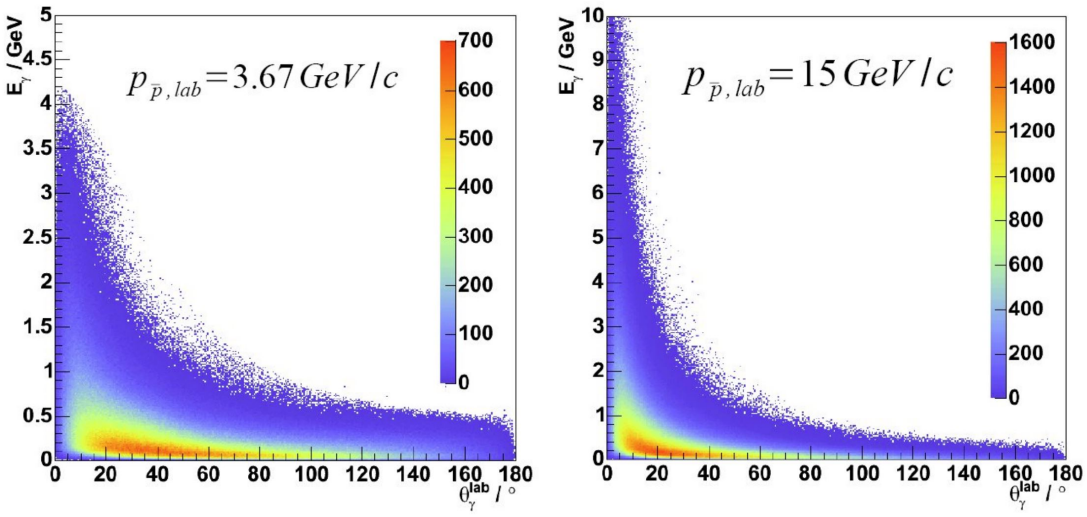

Figure 63: Simulations of the angular dependence of the photon energy distribution for two different particle momenta [4].

ageing-processes, like e.g. radiation damages.

On the other hand, large experiments like $\overline{\text{P}}$ANDA always bear the risk of pick-up noise despite thorough shielding. A higher gain provides a possibility to cope with this, as it reduces the electronic noise in relation to the signal heights.

7. Outlook

Several tasks concerning the Mainz19 beamtime have to be completed in the future. The most obvious of these is the fact that twelve different ASIC-gain-APD-gain-combinations have been measured, while it was only possible to investigate two of these combinations in the course of this thesis. It was shown, that the APD-gain 500 does improve the energy resolution greatly, but an APD-gain of 300 or 400 could also hold some useful information or have an even better resolution. The ASIC-gain 1 runs could also hold valuable information. If e.g. the energy resolution of the measured data does not worsen significantly compared to the ASIC-gain 16 runs even for the low energy regime, then the possibility to get rid of the high-gain branch completely could be considered, as this would generate additional free space desperately needed for the barrel.
The analysis already done could be further improved by taking a closer look at the fit parameters. Due to the automatic fit process not working properly, it had to be done manually, resulting in it being very lengthy and prone to errors. A more detailed view in the hit-detection threshold and the single crystal threshold could also bring valuable insights. The lowest possible single crystal threshold for a minimum energy resolution should drop until a certain point with increasing APD-gain, due to the signal-to-noise ratio at the APFEL-input being lower. As this effect was not observed until now, further analysis might make even lower energy resolutions possible. The noise and, more importantly, better ways to cope with it and prevent it in the future should also be observed further. If not handled and avoided correctly, it could be a major issue in the later $\overline{\mathrm{P}}$ANDA-experiment.
Another point that can be investigated, is the energy and time resolution achieved by using only one APD in comparison to two APDs. Again, if the results don't worsen much when using only one APD, one could consider equipping every crystal with just one instead of two APDs, creating more free space, especially in the support-beam, by reducing the required amount of signal cables.

Lastly, another beamtime could be conducted, gathering more data especially in the high-energy regimes. The response function of the 1.4 run showed a behaviour, that could account for lower energy resolutions, even in energies way above 400 MeV. As the statistics were too low, this could and can not be proven with the current available data. Therefore, one could measure higher energies and over a longer time / with higher intensities to verify these assumptions in a future beamtime.

References

[1] Anastasios Belias. PANDA detector design at FAIR. *9th International Conference on New Frontiers in Physics*, 2020.

[2] Christoph Rosenbaum. *Optimization of the Front-End electronics of the PANDA Barrel EMC*. Dissertation, Justus-Liebig-Universität Gießen, 2016.

[3] Kim Giebenhain. *Large Area Avalanche Photodiode Gain Optimization for the APFEL ASIC Preamplifiers of the PANDA Calorimeter*. Bachelor's thesis, Justus-Liebig-Universität Gießen, 2019.

[4] PANDA Collaboration. Technical design report for PANDA electromagnetic calorimeter (EMC). Technical report, 2008.

[5] PANDA Collaboration. PANDA annual report 2019. Technical report, 2019.

[6] Oliver Noll. Digital signal processing for the EMC. *PANDA Collaboration Meeting 19/3*, 2019.

[7] Benjamin Wohlfahrt. *Matching of Avalanche Photodiodes and Light Injection Into Scintillation Crystals*. Dissertation, Justus-Liebig-Universität Gießen, 2019.

[8] Lukas Nies. *A Novel Approach for the Photo-Readout of a Lead-Tungstate Calorimeter With Silicon Photomultipliers*. Master's thesis, Justus-Liebig-Universität Gießen, 2019.

[9] Markus Moritz. *Measurements and improvements of the response of the PANDA-EMC prototype PROTO 60 to high energetic particles and photons in accelerator experiments*. Dissertation, Justus-Liebig-Universität Gießen, 2013.

[10] PANDA Collaboration. Technical design report for PANDA electromagnetic calorimeter (EMC). Technical report, 2020.

[11] Stefan Diehl. *Optimization of the influence of longitudinal and lateral non-uniformity on the performance of an electromagnetic calorimeter*. Dissertation, Justus-Liebig-Universität Gießen, 2016.

[12] O C Alkofer. The absolute cosmic ray flux at sea level. *Journal of Physics G: Nuclear Physics*, 1975.

[13] Tobias Eissner. *The new PWO Crystal Generation and Concepts for the Performance Optimisation of the PANDA EMC*. Dissertation, Justus-Liebig-Universität Gießen, 2013.

A. Appendix

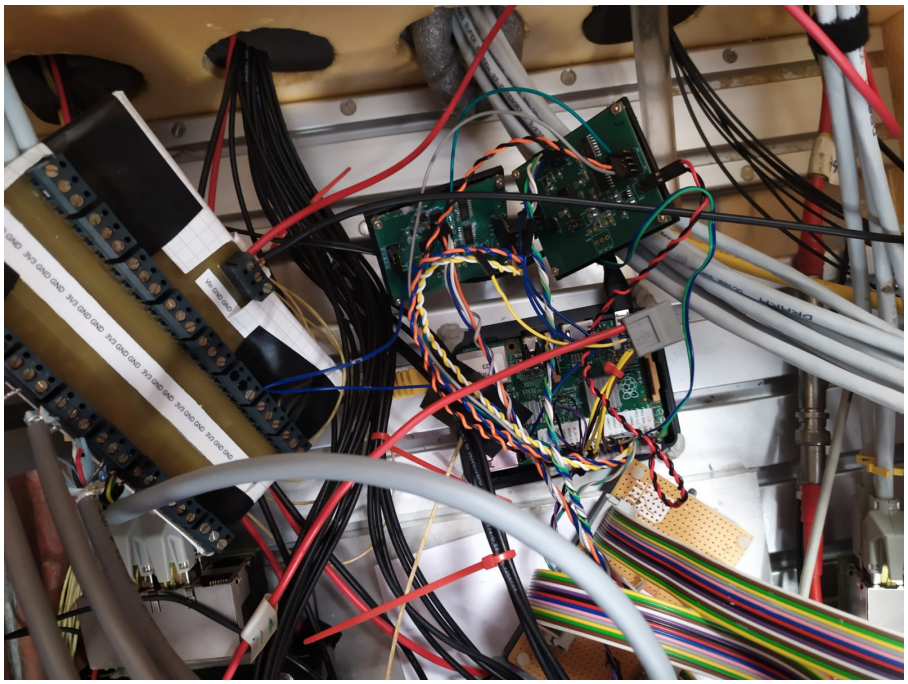

Figure 64: Voltage distribution board and electronics for controlling the APFEL-ASICs. On the left side, a voltage distribution board can be seen that acts as power supply for the APFEL-matrices. On the right side of the picture is a Raspberry Pi and two intermediate boards, to enable the communication with the APFEL-ASICs and, therefore, the modification of the DAC-values.

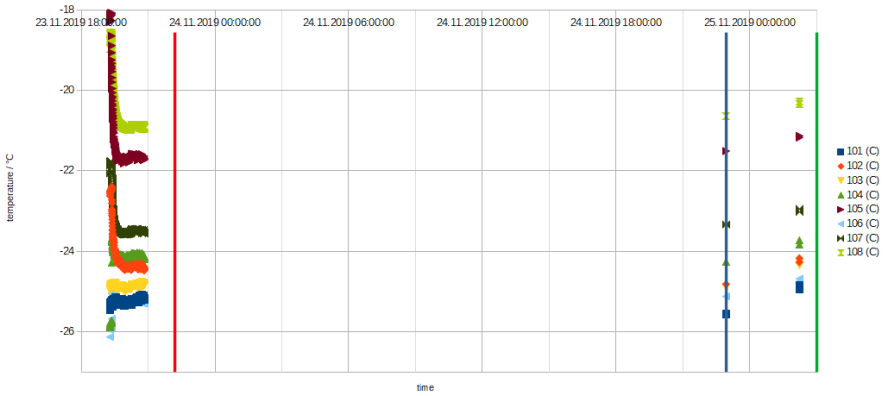

Figure 65: Monitored temperatures over the course of the experiments. The vertical lines mark: the start of the first beam runs (left, red), the start of run 3.1 (mid, blue) and the start of the cosmic runs (green, right).

Table 13: This table shows the set, optimal DAC-values of the APFEL-ASICs for the High-APD-gain x16 amplification. The values were optimised before the first HG16-run and were used for all HG16-measurements

Detector	DAC 1	DAC 2	DAC 3	DAC 4
2	758	760	673	380
5	750	743	673	375
3	762	762	673	380
6	757	762	673	370
8	763	763	673	370
9	757	753	673	360
4	762	767	673	380
1	759	764	673	400
7	762	755	673	350

Table 14: This table shows the set, optimal DAC-values of the APFEL-ASICs for the Low-APD-gain amplification. The values were optimised before the first LG-run and were used for all LG-measurements

Detector	DAC 1	DAC 2	DAC 3	DAC 4
2	758	760	685	380
5	750	743	690	375
3	762	762	710	380
6	757	762	700	370
8	763	763	705	370
9	757	753	700	360
4	762	767	710	380
1	759	764	710	400
7	762	755	720	350

Table 15: This table shows the set, optimal DAC-values of the APFEL-ASICs for the High-APD-gain x32 amplification. The values were optimised before the first HG16-run and were used for all HG32-measurements

Detector	DAC 1	DAC 2	DAC 3	DAC 4
2	777	779	680	390
5	774	768	680	440
3	782	787	680	450
6	774	780	680	400
8	787	787	680	470
9	787	776	680	470
4	790	794	680	500
1	780	782	680	475
7	793	780	680	475

List of Figures

1. The particle accelerator facility of FAIR . . . 3
2. HESR at FAIR . . . 4
3. schematic of the $\overline{\text{P}}$ANDA-experiment . . . 5
4. Image of a single detector . . . 10
5. Functional schematic of APD with reverse structure . . . 11
6. schematic layout of APFEL-ASIC . . . 12
7. picture of the $\overline{\text{P}}$ANDA-SADC with the main parts highlighted . . . 13
8. Pictorial representation of the FIR . . . 14
9. Description of the amplitude extraction algorithm of the FEx by Oliver Noll . . . 15
10. Description of the time extraction algorithm of the FEx by Oliver Noll 15
11. Numbering scheme of the detectors in the matrix and APD position 18
12. Miller-Fit on APD-gain vs. bias voltage data . . . 19
13. image of a backplane used in the readout electronics . . . 21
14. image of a bufferboard used in the readout electronics . . . 21
15. Picture of the complete readout-chain . . . 22
16. Drawing of the cooling box and the inset detector matrix . . . 23
17. Cooling box interior . . . 23
18. Julabo cryostat . . . 24
19. Rear view of the cryostat . . . 24
20. Rear view of the cooling box . . . 24
21. Light pulser used for the reference system . . . 26
22. Light fibres attached to the front of the crystals . . . 26
23. Layout of the MAMI accelerator facility . . . 28
24. Scheme of the front end electronics with detectors and tagger channels 29
25. Monitored temperatures over the course of the beamtime . . . 32
26. Display of the live view SADC-readout . . . 33
27. Histogram of all traces of the ASIC-gain 16 and APD-gain 500 run 35
28. Histogram of all events of the ASIC-gain 16 and APD-gain 500 with a time-filter applied . . . 35
29. Detected tagger events . . . 36

30. Noisy traces . . . 37
31. Cosmic muons with overlapping noise . . . 37
32. Energy distributions of the cosmic data before event selection . . . 41
33. Timing distributions of the cosmic data before event selection . . . 42
34. Effects of the moving average filter on a noisy trace . . . 43
35. Effects of the moving average filter on a noisy trace . . . 43
36. Energy distributions of the cosmic data after the moving average filter 46
37. Energy distributions of the cosmic data after event selection . . . 47
38. Time distributions of the cosmic data after event selection . . . 48
39. Reference trace after MA-filter . . . 50
40. 2D-Histogram of the detector energy vs. reference energy . . . 50
41. Timing distribution of the central detector . . . 52
42. Comparison of central detector coincidence with and without a central time-filter . . . 53
43. Comparison of central detector timing with the timing distribution of a non-central detector . . . 54
44. Energy distribution without individual time-filter . . . 55
45. Energy distribution with 2k time-filter to both sides . . . 56
46. Energy distribution without 5k left and 2k right individual time-filter 57
47. Comparison of multiple energy distributions for beam retracing . . . 58
48. Lineshapes of the 41 MeV photon energy events . . . 60
49. Lineshapes of the 101 MeV photon energy events . . . 60
50. Lineshapes of the 201 MeV photon energy events . . . 61
51. Histogram of the different lineshapes . . . 62
52. Histogram of the different lineshapes with logarithmic y-axis . . . 62
53. Comparison of different thresholds for the response function of ASIC-gain 16 and APD-gain 500 . . . 64
54. Threshold scans for different tagger energies . . . 64
55. Fit of the ASIC-gain 16, APD-gain 500 response function . . . 65
56. Comparison of different thresholds for the response function of ASIC-gain 16 and APD-gain 150 . . . 66
57. Fit of the ASIC-gain 16, APD-gain 150 response function . . . 66
58. Threshold scan for low energy in the PROTO60 . . . 71
59. Comparison of the 1.1 beam data with the PROTO120 results . . . 71

60. Dependence of reconstruction loss on single crystal threshold 72
61. Response functions for APD-gain 150 and APD-gain 500 75
62. Comparison of the 1.4 beam data with the PROTO120 results . . . 75
63. Simulation of the angular dependence of the photon energy distribution 77
64. Voltage distribution board and APFEL-control 81
65. Monitored temperatures over the course of the experiments 81

List of Tables

1. Requirements for the Barrel-EMC 6
2. IDs of the utilised APDs and crystals 18
3. Gain of the actual APDs on detector 7 20
4. Required bias voltages for the desired APD-gains 20
5. temperature data at the start of the beamtime 25
6. Allocation of SADC inputs 30
7. Overview of the conducted beam experiments 31
8. APD-gain settings at the beamtime 34
9. Results saved by the analysis software 39
10. Fit results of the cosmic data 45
11. Determined slopes of the relations between detector energies and reference energies 51
12. Comparison of response function fit parameters 74
13. High-APD-gain x16 DAC-settings at beamtime 82
14. Low-APD-gain DAC-settings at beamtime 82
15. High-APD-gain x32 DAC-settings at beamtime 83

Acknowledgements

Danksagungen

Zum Ende dieser Arbeit möchte ich die Gelegenheit nutzen, um mich bei all denen zu bedanken, die mich auf meiner bisherigen universitären Laufbahn begleitet und unterstützt haben.
Zuvorderst möchte ich mich bei Herrn Prof. Dr. Brinkmann für die Vergabe des Themas und die Ermöglichung meiner wissenschaftlichen Arbeit bedanken, sowie auch für die Beschäftigung in der Arbeitsgruppe und die Ermöglichung meiner Experimente auf der Strahlzeit in Mainz.
Ebenfalls danken möchte ich Herrn Dr. Markus Moritz und Herrn Dr. Hans-Georg Zaunick für die Betreuung meiner Arbeit und das stete Einbringen neuer Ideen und ihrer Expertise. Vielen Dank auch für die Geduld, die doch manchmal nötig gewesen ist. Darüber hinaus möchte ich auch Herrn Dr. Valera Dormenev, für das Teilen seiner Erfahrung im Umgang mit den verwendeten Szintillatoren, danken.
Ein weiterer, besonderer Dank gilt Herrn René Schubert für die technische Betreuung und Beratung einiger Aspekte der Experimente und auch für das Bewahren eines kühlen Kopfes, wann immer es nötig war. Ebenfalls an den technischen Details der Arbeit beteiligt und daher meinen Dank verdient haben die Herren Marcel Straube und Ulrich Thöring aus dem Elektroniklabor. Darüber hinaus bedanke ich mich auch bei Herrn Thomas Wasem und der Feinmechanischen Werkstatt für die Planung und Konstruktion der Kühlbox.
Mein Dank gilt weiterhin allen Mitgliedern der Arbeitsgruppe, die mich wie selbstverständlich unter sich aufgenommen haben und besonders denen, die direkt oder indirekt an der Strahlzeit oder deren Vorbereitung beteiligt waren und all jenen, die den Forschungsalltag durch Hilfsbereitschaft und Humor aufzuwerten wussten. Zusätzlich bedanke ich mich noch bei allen weiteren Helfern auf der Strahlzeit, hierbei insbesondere bei Herrn Dr. Peter Drexler für die Betreuung vor Ort.
Weiterhin bedanken möchte ich mich bei den Herren Oliver Noll, Dr. Johannes Müllers und Dr. Pawel Marciniewski für das Beisteuern ihrer Expertise.
Zusätzlich möchte ich noch meinen Lektoren danken und besonders denen, die noch kurz vor der Abgabe innerhalb kürzester Zeit erfolgreich auf Fehlersuche gegangen sind.

Acknowledgements

Zu guter Letzt möchte ich mich bei allen Freunden und Kommilitonen, die mich bei den Höhen und Tiefen meines Studiums unterstützt haben und auch bei meiner Lebensgefährtin, meiner Mutter und meinen Großeltern ohne deren fortwährende und unermüdliche Unterstützung nichts von alldem hier möglich gewesen wäre.